Université Lille I - Sciences et Technologies
Laboratoire de Mécanique de Lille (UMR CNRS 8107)
Ecole Doctorale SPI Lille Nord-de-France

Année 2012 - N° d'ordre : 40856

THESE

Pour obtenir le grade de
Docteur de l'Université Lille I - Sciences et Technologies
Discipline : Génie Civil

Présentée par
Yun HUANG

Modélisation micromécanique du comportement différé des roches argileuses – application au stockage des déchets radioactifs

Soutenue publiquement le 27 Septembre 2012 devant le jury composé de

M. A. GIRAUD, Professeur, INPL-ENSG	**Rapporteur**
M. D. HOXHA, Professeur, Université Orléans	**Rapporteur**
Mme. A. ABOU CHAKRA, Maître de conférences, INSA Toulouse	**Co-encadrant**
M. G. ARMAND, Ingénieur, ANDRA	**Examinateur**
M. PY. HICHER, Professeur, Ecole Centrale Nantes	**Examinateur**
Mme. Y. JIA, Maître de conférences, Université Lille I	**Co-encadrant**
M. N. LAHELLEC, Maître de conférences, LMA	**Examinateur**
M. JF. SHAO, Professeur, Université de Lille I,	**Directeur de thèse**

Contents

Remerciements

Ce mémoire représente mes travaux de recherche pendant quatre années dans notre beau bureau D100 à Polytech'Lille.

Mes remerciements s'adressent tout d'abord à mon directeur de thèse Jian-Fu Shao pour m'avoir accueilli au sein du Laboratoire de Mécanique de Lille et m'encadrer depuis mon master. Je suis impressionné par ses connaissances et sa rigueur scientifique. Quand je suis perdu, Monsieur SHAO peut trouver mes fautes assez rapidement et m'aide de calibrer avec sa patience et son amitié.

Je voudrais exprimer ma gratitude tout particulièrement envers Ariane Abou-Chakra pour m'avoir encadrée pendant quatre années. Bien qu'elle travaille et demeure à Toulouse, elle est toujours passionnée de m'aider. Je n'oublierai jamais que, dans les moments les plus difficiles, nous avons travaillé ensemble à Toulouse et à Marseille et discuté par des centaines d'e-mail pour trouver les solutions possibles.

Je lance un grand merci à Noël Lahellec. Il nous a accueilli chaleureusement au Laboratoire de Mécanique et d'Acoustique à Marseille pour nous aider à résoudre les problèmes concernant sur la méthode variationnelle incrémentale. Grâce à lui, mon travail a pu être continué.

Je remercie vivement Pierre-Yves Hicher pour m'avoir fait l'honneur de présider mon jury, Albert Giraud et Dashnor Hoxha pour avoir accepté d'être rapporteurs de cette thèse ainsi que Yun Jia et Gilles Armand, membres du jury.

Je remercie également Shouyi Xie et Jean Secq pour leurs patiences et leurs amitiés. Leurs ardeurs et leurs idées nouvelles dans les essais m'ont profondément touché.

Mes remerciements s'adressent également à mes meilleurs amies He Yang, Tao Zeng et Zheng He pour leur compagnie, pour leur sympathie et humeur. Je n'oublierai pas nos nombreuses discussions sur la micromécanique dans notre bureau.

Pour finir, Je remercie mes parents, ma femme et toute ma famille pour leur soutien constant à travers ces longues années.

Notation

Tensor notation

x	scalar	$\cdot$	simple contraction
$\underline{x}$	vector	:	double contraction
$\mathbf{x}$	second-order tensor	$\otimes$	tensor product
$\mathbb{X}$	fourth-order tensor	$\boldsymbol{\delta}$	second-order identity tensor
$\mathbb{I}$	fourth-order identity tensor	$\mathbb{J} = \frac{1}{3}\boldsymbol{\delta}\otimes\boldsymbol{\delta}$	

$\mathbb{K} = \mathbb{I} - \mathbb{J}$

Common notation in all chapters

Ω	the domain occupied by the REV
$\partial\Omega$	boundary on the REV
Ω^s	solid domain in the REV Ω
$\boldsymbol{\Sigma}$	macroscopic stress tensor
$\tilde{\boldsymbol{\Sigma}}$	mesoscopic stress tensor
$\boldsymbol{\sigma}$	microscopic stress tensor
$\mathbf{E}$	macroscopic strain tensor
$\tilde{\mathbf{E}}$	mesoscopic strain tensor
$\boldsymbol{\varepsilon}$	microscopic stress tensor
$\mathbb{A}$	strain concentration tensor
d	density of damage by microcracks
$\mathbb{C}$	elastic stiffness tensor
$\mathbb{C}^{\text{hom}}$	homogenized elastic stiffness tensor
$\mathbb{L}$	tangent operator
$\mathbb{L}^{\text{alg}}$	algorithmic tangent operator
k^{hom}	homogenized bulk modulus in isotropic conditions
μ^{hom}	homogenized shear modulus in isotropic conditions
ν	Poisson's ratio
E	elastic Young's modulus
φ	porosity

Introduction générale

Dans le cadre des études de faisabilité du stockage des déchets radioactifs de haute activité et à vie longue en formation géologique profonde, nous sommes amenés à effectuer des modélisations des phénomènes de couplage THM à court et à long terme engendrés par l'excavation et le stockage. Grâce à sa faible perméabilité qui impose un transport par diffusion et sa capacité de rétention, les argilites du Callovo-Oxfordien ont été choisies comme potentielles barrières géologiques pour le stockage. Au vu de la complexité des phénomènes mises en jeu, la thèse se limitera à l'étude de son comportement mécanique différé, volet essentiel à l'étude des couplages précités.

Pour la caractérisation du comportement différé des argilites, deux mécanismes de fluage sont souvent envisagés: la déformation viscoplastique de la matrice argileuse et la propagation subcritique de microfissures. Dans ce travail, les deux mécanismes de fluage sont étudiés respectivement. Comme les approches micromécaniques permettent de conduire à une meilleure description du comportement macroscopique en relation avec les aspects microstructuraux de la roche et d'éviter ainsi le recours à une identification des paramètres pour chaque zone géomécanique, dans ce travail, nous proposons de mettre en œuvre une modélisation multi-échelle construite à partir des comportements des constituants et des données microstructurales de l'argilite.

Le mémoire de thèse se décomposera en cinq chapitres de la manière suivante:

Le chapitre 1 présente la problématique dans son ensemble. Dans un premier temps, on y décrit le concept de stockage en formation profonde et la géologie du site où se situe le laboratoire de recherche souterrain construit par l'ANDRA. Une modélisation de l'argilite dans cette zone apparaît alors comme essentielle pour la sûreté des ouvrages de stockage à long terme. Souhaitant développer des modèles mécaniques ayant une base physique pertinente, nous précisons les éléments du choix d'une modélisation par transition d'échelle basée sur un passage "micro-macro". Une deuxième partie présente une description de la microstructure de l'argilite et une revue des traits fondamentaux du comportement mécanique macroscopique de l'argilite (viscoplasticité, endommagement par microfissuration de la matrice argileuse...). Cette étape de compréhension du matériau aux deux échelles est cruciale dans l'optique de la modélisation par changement d'échelles.

Le chapitre 2 présente d'abord l'homogénéisation du comportement des argilites en régime élastique. Le principe des méthodes de changement d'échelle est d'abord rappelé. Les schémas d'homogénéisation linéaires (schéma dilué, estimation de Mori-Tanaka [Mori et Tanaka, 1973] et modèle autocohérent [Hill, 1965b]) ainsi que des bornes de Voigt et de Reuss [Voigt, 1889; Reuss, 1929], bornes de Hashin-Shtrikman [Hashin et Shtrikman, 1962] reposant sur les principes variationnels seront brièvement rappelés. Enfin, une introduction à une méthode d'homogénéisation du comportement non linéaire de l'argilite, l'approche incrémentale de Hill [Hill, 1965a], clôturera ce chapitre.

Le chapitre 3 proposera une modélisation micromécanique du comportement différé des argilites du Callovo-Oxfordien, basée sur l'étude de la propagation subcritique de microfissures. Les argilites sont alors considérées comme des composites constituées de trois phases: une matrice argileuse élastique endommageable, deux types d'inclusions minérales ayant un comportement élastique linéaire : à savoir les grains de calcite et de quartz. Des schémas d'homogénéisation basés sur l'approche incrémentale de Hill sont appliqués aux argilites. Leur efficacité sera évaluée par comparaison avec les essais de fluage.

Le chapitre 4 présente une modélisation du comportement différé des argilites en faisant référence à la déformation viscoplastique de la matrice argileuse. Cette modélisation tient en compte des effets de la porosité dans la matrice argileuse à l'échelle en dessous de micrométrique. Comme les inclusions dominantes (calcite et quartz) dans l'argilite sont de l'ordre du micromètre, une modélisation obtenue par deux étapes de changement d'échelle est nécessaire: à l'échelle mésoscopique, les argilites sont composées d'une matrice argileuse poreuse dans laquelle sont noyés des inclusions minérales élastiques; et à l'échelle microscopique, la matrice argileuse est elle-même constituée d'une phase solide qui est un assemblage de particules argileuse et de pores. Ce travail consiste à étendre celui récemment effectué par Shen et al. (2012) sur la modélisation micro-macro du comportement instantané des argilites au comportement différé. De ce fait, les propriétés effectives de la matrice argileuse poreuse sont décrites par un modèle viscoplastique. Pour déterminer le comportement différé macroscopique de l'argilite, une approche incrémentale modifiée basée sur les travaux de [Hill, 1965a] sera proposée.

Enfin dans le chapitre 5, nous proposons une adaptation d'une approche variationnelle incrémentale initialement proposée par Lahellec et Suquet (2007) à la modélisation du

comportement différé des argilites. Ce travail est motivé par le fait que dans la plupart des modèles micromécaniques non linéaire, on fait l'hypothèse de distribution homogène des champs locaux dans chaque phase. Cette simplification forte conduire à une réponse macroscopique trop rigide du matériau. Il convient alors d'apporter des améliorations en tenant en compte de l'hétérogénéité des champs locaux. Par les diverses méthodes proposées dans la littérature, l'approche variationnelle incrémentale proposée par Lahellec et Suquet (2007) présente une démarche rigoureuse de prendre en compte l'hétérogénéité des champs locaux. Le problème d'homogénéisation du matériau hétérogène est transformé en un problème de minimisation dans un matériau thermoélastique linéaire équivalent. Dans le présent travail, nous proposons une adaptation de cette approche à la modélisation des argilites en tenant compte de ses spécificités, notamment la transition de contractance-dilatance volumique et les effets de la pression de confinement.

Le mémoire de thèse se termine par une présentation de conclusion générale et des perspectives.

Chapter 1 Context of the thesis

Résumé du chapitre :

Le chapitre 1 présente la problématique dans son ensemble. Dans un premier temps, on y décrit le concept de stockage en formation profonde et la géologie du site où se situe le laboratoire de recherche souterrain. Une modélisation de l'argilite dans cette zone apparaît alors comme essentielle pour la sûreté des ouvrages de stockage à long terme. Souhaitant développer des modèles mécaniques ayant une base physique pertinente, nous précisons les éléments du choix d'une modélisation par transition d'échelle basée sur un passage "micro-macro". Une deuxième partie présente une description de la microstructure de l'argilite et une revue des traits fondamentaux du comportement mécanique macroscopique de l'argilite (viscoplasticité, endommagement par microfissuration à la matrice argileuse...). Cette étape de compréhension du matériau aux deux échelles est cruciale dans l'optique de la modélisation par changement d'échelles.

1.1 Introduction on the underground radioactive waste storage

1.1.1 Management of the radioactive wastes

The radioactive wastes come form different domains. Particularly, it arises with as a byproduct of the generation of the nuclear science and technology industry. In France, Radioactive waste is divided into three different categories:

- the wastes A: low level waste ,which are now stored in above ground storage;
- the wastes B: intermediate level waste, which, contain the long-lived radionuclide;
- the wastes C: high level waste being vitrified, which are the centre of an activity and a high thermicity and contain the most of long-lived radionuclide.

The French government has decided to store the wastes of low- and intermediate level short-lived at these productions sites, mainly la Hague (Manche), Marcoule and Cadarache. On the other hand, the management of the high-level long-lived wastes and the medium-level long-lived wastes is currently under study coordinated by the ANDRA (Agence Nationale pour la gestion des Déchets Radioactifs).

ANDRA is created with the CEA (Commissariat à l'Energie Atomique) on 7th November 1979. in 1991, it was established by the December 1991 waste act as a public organization in charge of the long-term management of all radioactive wastes. Its three research axes are presented as follows:

- the research and development axe: propose safe long-term solution for radioactive waste without current disposal system, partitioning and transmutation: study for the solutions to reduce the mass and toxicity of the long-lived radionuclide,
- the 2nd axe, underground storage: to define the conditions in which could be realized and exploited a deep geological storage,
- the 3rd axe, packaging and storage for long term: includes the development of packaging in the form of waste packages and facilities for conservation and recovery under acceptable conditions.

The 1st and 3rd axes are conducted by CEA, while the underground storage, the 2nd axe was assigned to the ANDRA.

In the framework of the mission entrusted upon ANDRA by the Waste Act of 1991, the ANDRA have presented to the Ministers for Research and Industry in 2005 a report on the feasibility of deep geological disposal for high-level and long-lived radioactive waste. This report, called "Dossier 2005", summery the last 15 years investigations realized by ANDRA and promulgate the waste act of 2006. It formally declare deep geological disposal as the reference solution for high-level and long lived radioactive wastes. Furthermore, in this act, ANDRA is responsible for the design and establishment of a repository with target dates of 2015 for licensing and

2025 for operation. .

1.1.2 Repository concept

The objective is a geologic repository is to protect man and environment form the possible impact of radioactive wastes. It consists to design a “multi-barriers” system which is capable to confining the radioactivity for very long periods of time.

In very general terms, the geological storage can be represented as a group of elementary cavities excavated in the deep rock containing the waste packages, grouped together in modules (Fig. 1.1). These cavities are all connected by galleries, and the access from the outside is made possibly by wells passing through the geological formation. The waste packages will be placed between the natural rock and the geological barrier.

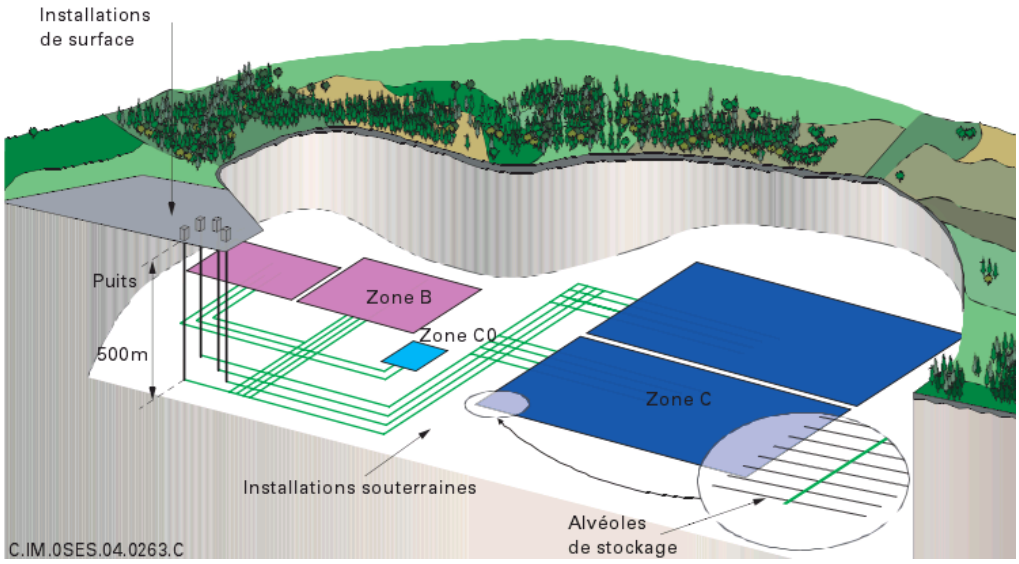

Fig 1.1 Diagram of repository architecture

1.1.3 The underground research laboratory

In the framework of feasibility study of underground storage for radioactive wastes, the geological formation is at the core of its construction. It must ensure the very long term confinement of radioactive substances to prevent their migration into the nature. In France, due to the favorable mechanicals and hydraulic properties of Callovo-Oxfordian argillite, it has been selected as a deep geological repository formation. Furthermore, it processes a very high potential for the retention of radionuclide migration.

In order to get a good understanding on the geological medium in the Meuse/Haute Marne sector, the ANDRA was authorized by decree of 3 Aug. 1999 to construct and install an underground laboratory to (Fig 1.2). On the site of the underground laboratory, the Callovo-Oxfordian argillite formation forms a uniform clay layer

between 422 and 552m in depth directly below the underground laboratory site. Due to layers dipping north-west, the depth increases progressively to attain more than 600m, fifteen kilometers or so towards north. In the same way, the layer thickness varies form about 130 to 160 m form south to north-west.

This clay formation was deposited 150 million years ago, while the Paris Basin was under the sea level, and is part of a sedimentary series which starts at the Middle Jurassic (Dogger) and ends by the upper Jurassic (Malm). This sedimentary period is approximately 44 million years.

The Callovo-Oxfordian formation is beyond the influence of the major regional faults (faults of the Marne in the west, coal pits of Gondrecourt-le-Château in the southeast) to ensure a tectonic relatively stable area (Fig 1.2). A geophysical campaign by "seismic reflection" in three dimensions, realized at the end of 1999 covering an area of 4.35km², has noted that the Callovo-Oxfordian argillite formation was steady and does not represent the observable heterogeneities.

To acquire the further information about the geological environment of the site Meuse/Haute-Marne and evaluate the long-term behavior of the argillite, a research laboratory is currently built at -490m depth. The installations consist of two vertical wells of 4 to 5 meters in diameter, an experimental gallery of 40m long located at -445m in the upper layer of argillite and a network of galleries of 485m long located at -490m in the middle layer (Fig 1.3). The experiments have begun in the experimental gallery at -445m and were used to analyze the rock structure and its reaction to the excavation of the rock. Since August 2005, the following research program is conducted within the main galleries at -490m. Its main object is to collect the geotechnical, hydraulic, thermal and geochemical data of clay formation. These studies focus on the characterization of the intensity and the extension of the damage created by the galleries excavation. About 130 boreholes were drilled from the galleries and 1400 experimental sensors were installed, enabling the measurements of strain under natural stress, of pore water pressure, of temperature, of permeability, of diffusion and of retention. Furthermore, since 1994, 27 boreholes several hundred meters deep have been excavated to carry out 2D and 3D seismic campaigns on the site, surveying to observe the outcropping formation both at local and regional scales, ascertaining the main features of the geological environment and taking samples. The objective of theses research work is to acquire a thorough understanding of the geological environment of the site Meuse/Haute-Marne to ensure the durability and stability of geological formation, especially the Callovo-Oxfordian argillite formation. It is also necessary to evaluate its long-term behavior, including the effect of the perturbations which is created by the implantation of underground repository.

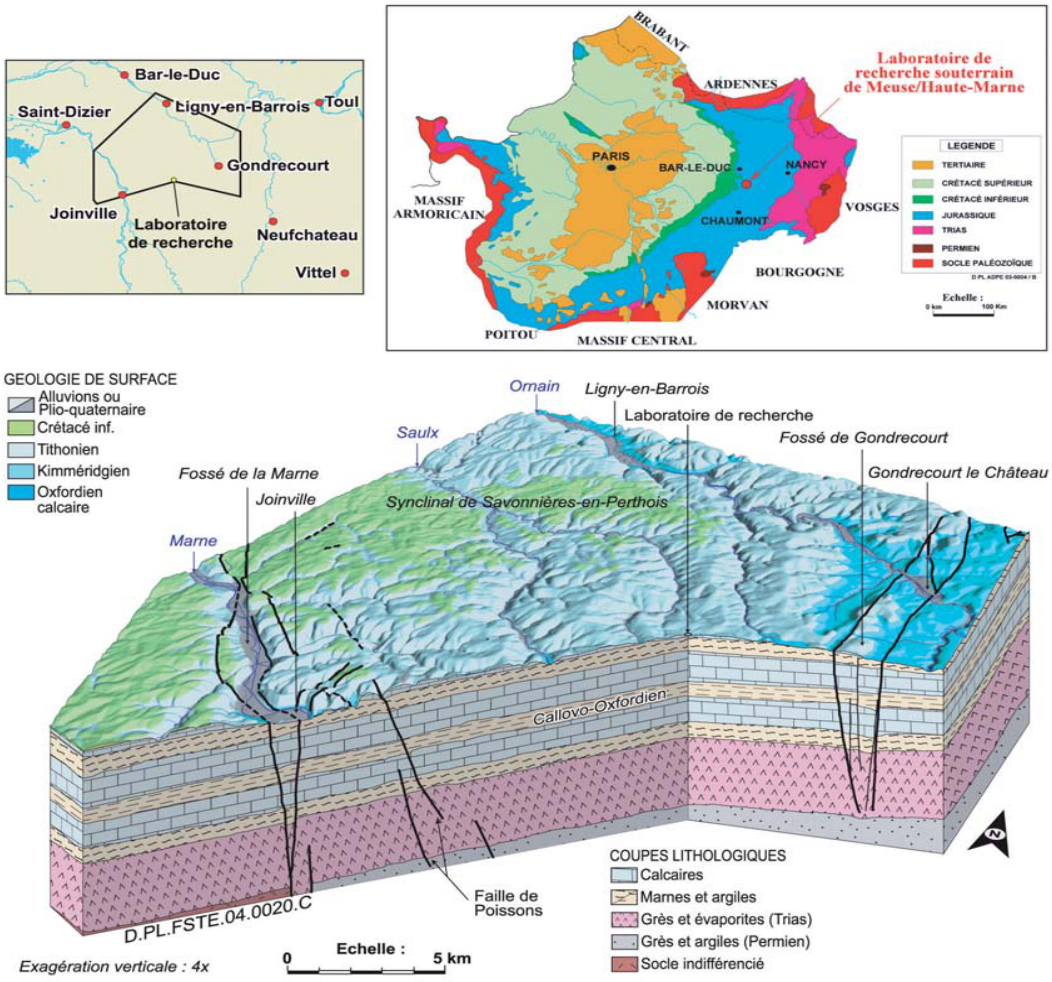

Fig 1.2 3D geological diagram of Meuse/Haute-Marne

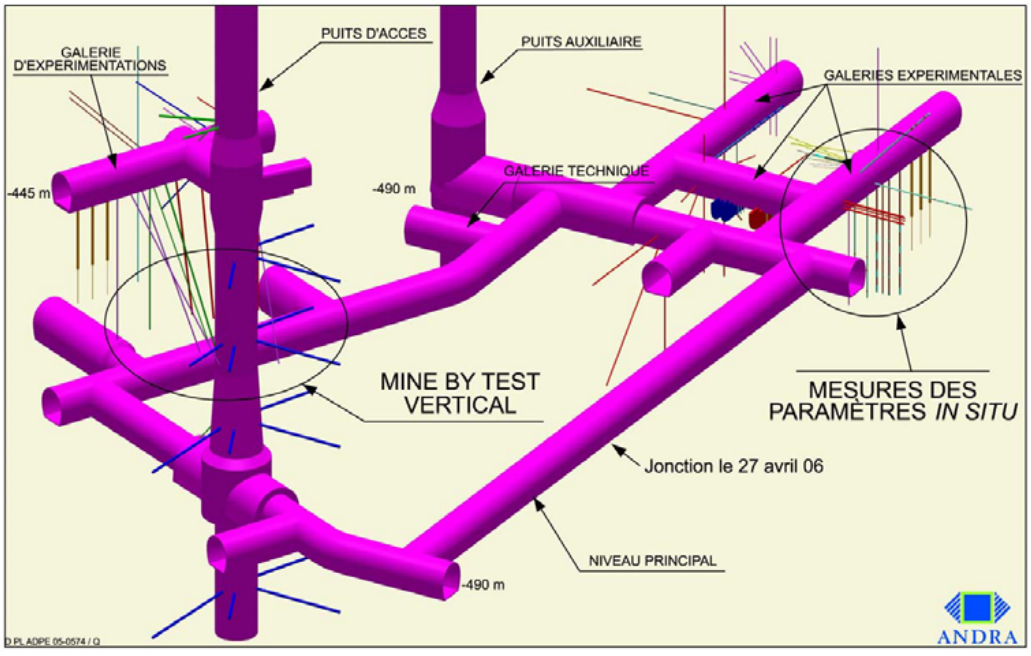

Fig 1.3 Location of the scientific works in the laboratory

1.2 Industrial context of the thesis

To get a deep understanding on the geomechanical issues related to the Callovo-Oxfordian geological formation, the different research themes of the ANDRA are scheduled as follows:

- the long-term stability of the storage zone and of the tunnel excavations;
- the excavation disturbed zone ;
- the impacts of the construction engineering on the storage site performance, the mechanical behavior of rock.

Our work is belong to one part of these research theses and consists of analyzing and predicting the thermo-hydro-chemo-mechanics behavior of the excavated zone in the short and long term. The mechanical behavior of the argillite formation in which radioactive materials will be stored plays a fundamental role for the performance of the storage site. This importance is underlined by the fact that these materials are notoriously difficult to characterize. Generally, the geological formations are significantly affected by the environment. Consequently, the difficulty of predicting their behavior, especially in the long term, will be more difficult. These disturbances environmental are given in the following:

- Mechanical: When the underground repository is created, a zone of disturbed rick at the interface, called the Excavation Damaged Zone (EDZ) appeared with the creation of some cracks. Furth more, the mechanical behavior of the underground repository and of the EDZ will subsequently evolve during operational phase and further following closure. Finally, over the long term, argillite creep plays an important role on the repository's mechanical evolution.

- Hydraulics: Initially, the creation of the repository induces an unloading of hydraulic head in the Callovo-Oxfordian argillite around the boreholes and the access galleries. During the following operation phase, the hydraulic head discharge propagates around the structures that are kept open or be ventilated. The argillites in the immediate vicinity of the structures will be desaturated. Finally, after the closure of the structure, the repository and the argillite in the near field subjected to desaturation during the operation phase will be resaturated and help the host rock to return to a new hydraulic equilibrium. This resaturation may be influenced by the hydrogen produced by the corrosion of repository metal corposants

- Thermal: After the installation of wastes package, its heat decay will a gradual increase in the temperature of the surrounding repository zones and geological environment. However, with the recessive decrease of heat decay of radioactive wastes, this temperature increase is transitory and disappear in several thousands years.

- Chemical: The chemical process include the interface reactions with the near field and clayey components, corrosion of metal components and chemical degradation of concrete. Moreover, these processes are affected by the thermal disturbance and the aforementioned hydraulic processes.

Aforementioned, in order to get a good understanding of the argillite behavior, it is necessary to take into account the coupled thermo-hydro-chemo-mechanic processes. Many macroscopic models have been proposed in recent years by different researchers (Chiarelli [2003], Hoxha [2005], Jia [2005], etc). These models have taken into account the numerous phenomena involved in the THCM coupling. However, they can not take into consideration of the complex physical phenomena which act at a microscopic scale, such as the mineral composition and microstructure of the argillite. In the objective to develop the mechanical models incorporating pertinent physical basis, some micro-macro transition models will be developed in this study. This thesis will be mainly focused on modeling the time-dependent mechanical behavior with the consideration of the micromechanisms of strain associated with the microstructure of the argillite. Afterwards, the microstructure of Callovo-Oxfordian argillites will be presented in the following section.

1.3 Microstructure and behavior of the Callovo-Oxfordian argillite

The previous research work performed by Andra on the microstructure and micromechanisms of the Callovo-Oxfordian argillite is synthesized in this section:

- the microstructure of the argillite and the micromechanisms of argillites. These phenomena govern the nonlinear macroscopic behavior of the rock and help us to develop a micro-macro model in the following chapter.
- The characterization of the macroscopic mechanical behavior in the short and long term.

1.3.1 Microstructure

Many experimental methods have been used by numerous partners of ANDRA to characterize and understand the microstructure of the Callovo-Oxfordian argillite ([Bornert, 2001], [Valès, 2001], [Sammartino, 2001], [Robinet, 2008]). Some

microscopic observations carried out on samples (scanning electron microscopy (SEM)) in Fig 1.4. Furthermore, optical microscope, microtomography (Fig 1.5)), radiography, tomography and digital camera help us to get a good knowledge on the microstructure of the argillite as well as the impact of microstructure on the macroscopic behavior of argillite. Nevertheless, the knowledge of the argillite in microstructural scale is essentially qualitative.

The Callovo-Oxfordian argillite is composed mainly of quartz, calcite and clay minerals (Fig. 1.4 (a) [Sammartino, 2001]) and a small percentage of subordinate minerals (dolomite, feldspar and pyrite) (Fig. 1.4 (d) [Valès, 2001]). One notices also the voids from sub-micron to nanometer scales which are preferentially associated with arrangement of the clay particles: inter-aggregates porosity. However, there is little or no inter-grain porosity. According to this mineralogical analysis, a two-scale modeling will be considered in chapter 4: at a mesoscopic scale, this clay rock is composed of a quasi continuous clay matrix which is embedded by mineral inclusions; at a smaller scale, the clay matrix is itself constituted of a solid phase which is an assembly of clay particles and pores between such particles. Nevertheless in chapter 5, with regard to introduce a new variational approach in modeling the argillite behavior, we will neglect the porosity of the material and consider only its mechanical properties.

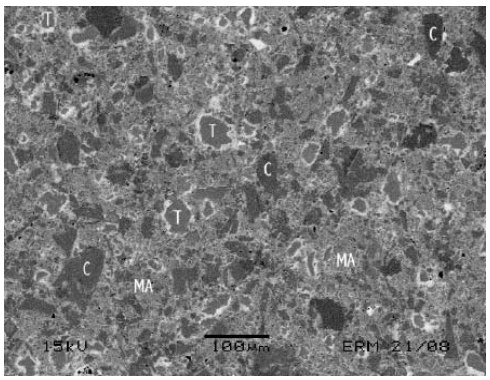

(a) SEM photo (backscatter mode) Sample N° HTM 01147
C=carbonates, T=tectosilicates and MA=clay matrix
[Sammartino, 2001]

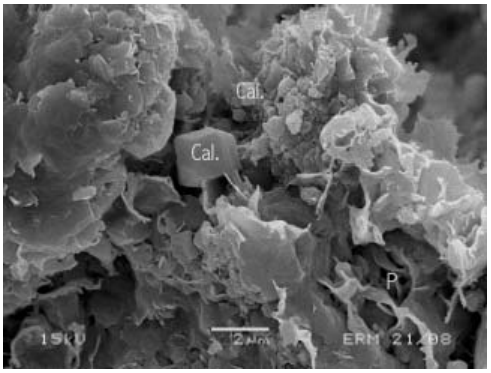

(b) SEM photo (secondary electron mode) Sample N° HTM 01147
Cal.=calcite, Q=quartz, P=pore
[Sammartino, 2001]

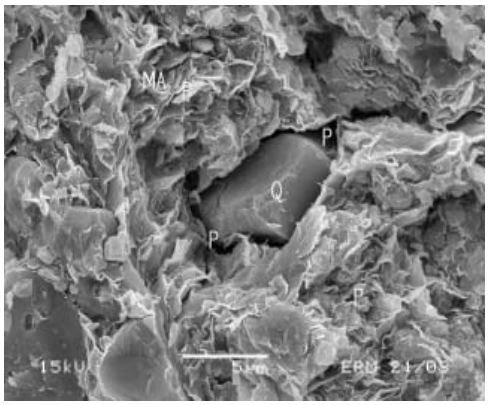

(b) SEM photo (secondary electron mode). Sample N° HTM 01147
Cal.=calcite, Q=quartz, P=pore
[Sammartino, 2001]

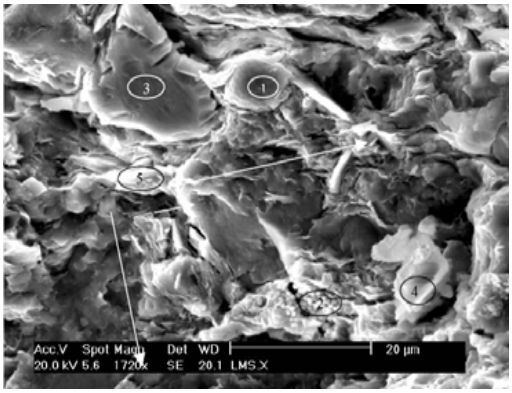

(d) SEM photo (the minerals are identified). Zone 1: Ca + Mg - grained dolomite; Zone 2: Fe + S - pyrite concretion; Zone 3 and 5: Si (dominant) + Al + Ca + K + Mg; Zone 4: Ca - grain of calcite [Valès, 2001]

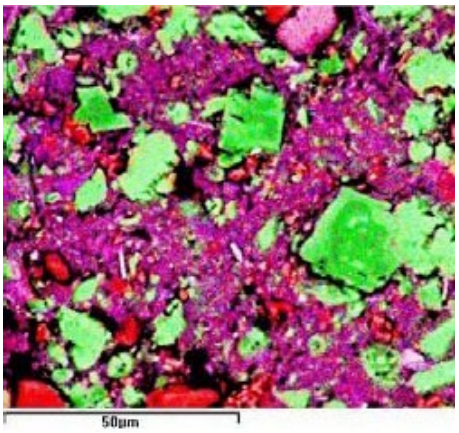

(c) RGB photo, sample N° HTM 01147
red= quartz, green=calcites, black=pore zone
[Sammartino, 2001]

Fig 1.4 Microstructure of the Callovo-Oxfordian argillite

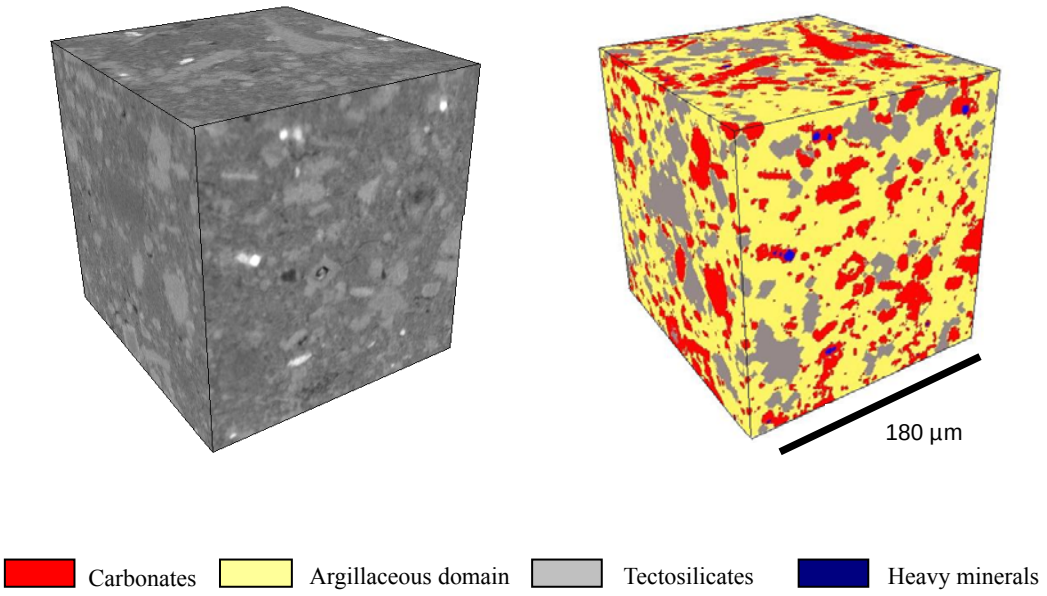

Fig 1.5 Mineralogical distribution of the Callovo-Oxfordian argillite EST26095 (-507 m) (3D Synchrotron microtomography) [Robinet, 2008]

Base on these experimental observations, the argillite formation may be considered as a heterogeneous medium in which the quartz and large calcite grains are dispersed in a fine matrix of clay minerals and calcite, which acts as cement the larger grains (Fig. 1.4 (a)). From the SEM observation, Gasc [Gasc, 1999] has observed the presence of clay particulars in the layer of sheets, including quartz and calcite crystal grains. She has noted that the carbonated phase does not constitute a cement but is organized in grains spread in a clay matrix. Using Optics and SEM method, Chiarelli (Chiarelli, 2000) have got a same observation: quartz and calcite grains are tied to the clay matrix. Mineral grains have principally a rounded shape and a dimension between 10 and 40µm. On the other hand, the clay minerals are grouped in cluster of some microns large that can coat very well the grain form.

The constituents of the argillite are distributed in the following proportions:

- 40-50% clay minerals in their vast majority of detrital origin (forms of debris from the continental erosion). The clay phase is mainly composed of non-swelling phyllosilicates: (mica + illite), kaolinite and chlorite, group strongly dominated by the set (mica + illite) with a proportion higher in mica than that in illite, and of swelling phyllosilicates: illite/smectite (I/S) interstratified minerals.
- 20-27% calcite (Fig. 1.4 (b) [Sammartino, 2001]), of rounded shape (detrital) or rhombohedral (diagenetic origin: neogenic calcite) and dimensions ranging from

about 10 to 40um. Note that the upper sequence and the lower sequence are more carbonated (27 to 37%) than the median sequence (22 to 30%).

- 23-25% quartz (Fig. 1.4 (c)), of more or less rounded shape and diameters between 20 and 40um.
- 5-10% various minerals (pyrite, mica, dolomite, halite, gypsum). The claystone also contains between 0.5 and 1% organic matter.

A notable variation in mineralogical composition is noticed with depth in the Callovo-Oxfordian formation (Fig. 1.6). consequently, the argillite formation is divided into five geomechanical zones from A to E (or geotechnical zones in Figure 1.6), characterized by different volume fractions of minerals as well as their mechanical properties. For example, in unit A, the volume fraction of carbonate content is the highest. Consequently, it process the higher mechanical properties (strength, Young's moduli) that these of B and C units.

In the horizontal direction, the formation of argillite processes the same mineralogical composition over a study area of 350 km². Moreover, based on the experimental observations realized in the boreholes around the underground laboratory, one notices that the distribution of mineral constituents is quasi-identical within a radius of 15 km around the studied boreholes (Fig. 1.7).

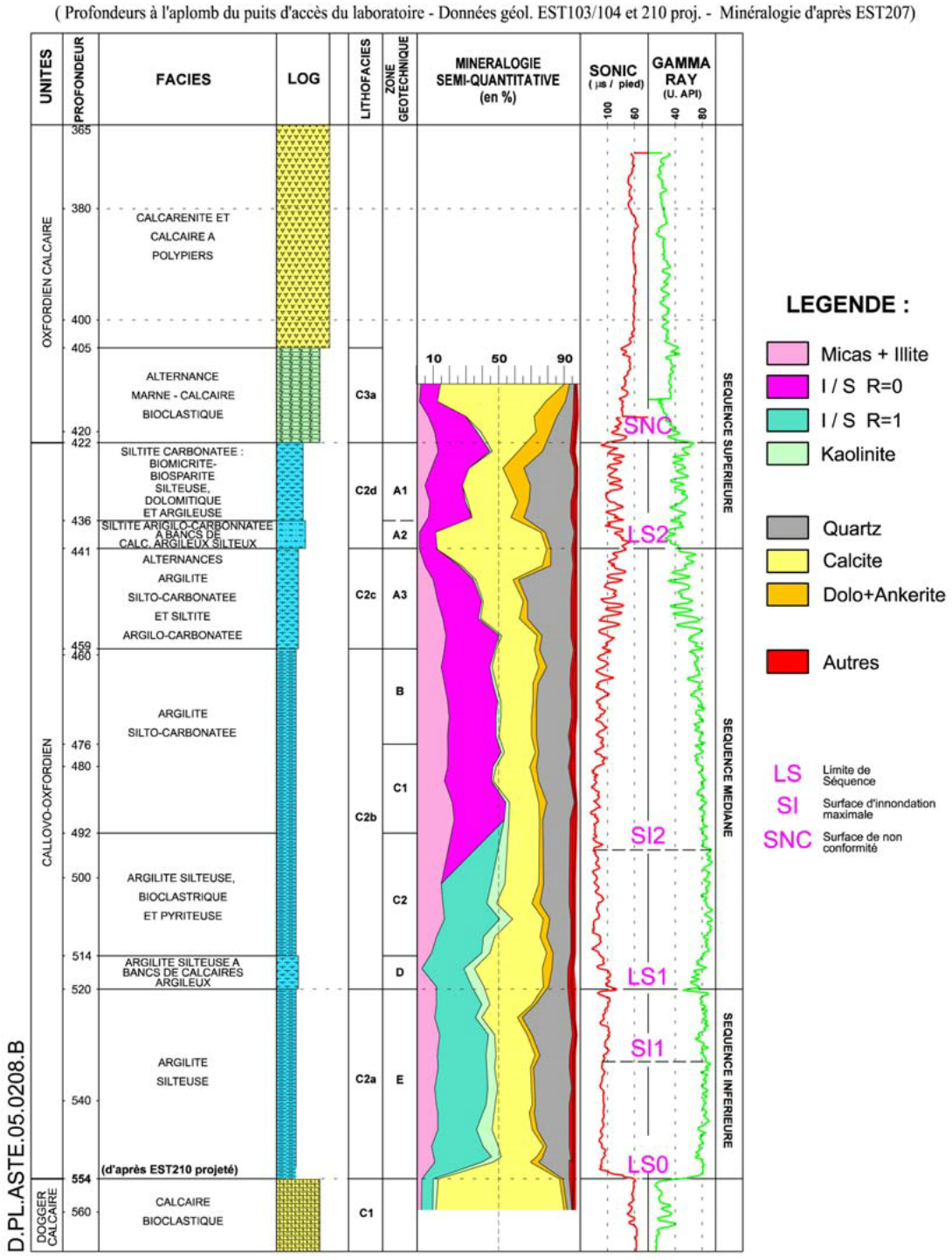

FIG. 1.6: Geological section of Callovo-Oxfordian on the site of the underground research laboratory. Geological data from EST 103/104, mineralogical data from EST 207.

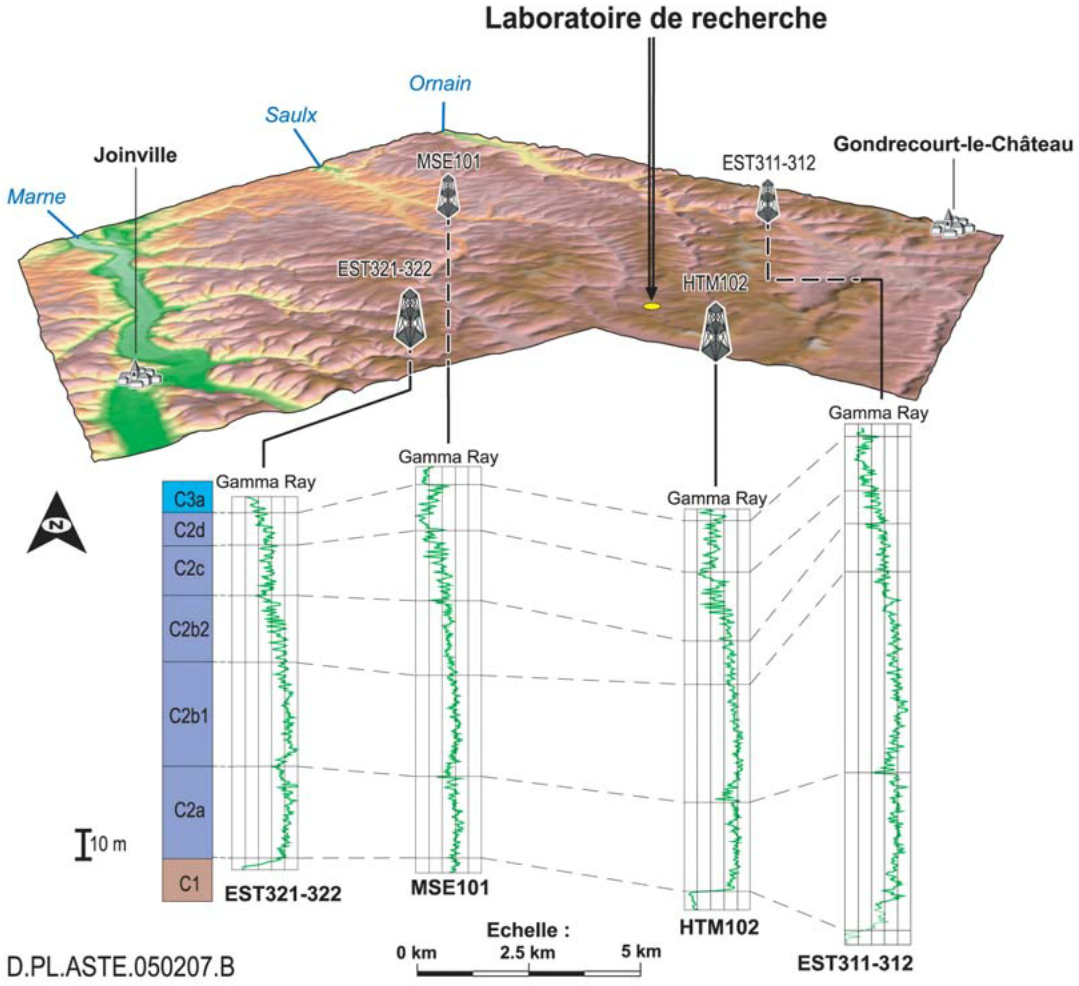

FIG. 1.7: Lateral homogeneity of Callovo-Oxfordian at the site studied

1.3.2 Micromechanisms

Based on the sum of microstructure of Callovo-Oxfordian argillite, its micromechanisms are presented in this section.

Based on microscopic analysis of the clay phase, the sliding movements of clay sheets against each other are observed. The picture (Fig. 1.8 (c)) shows the extruded clay minerals, confirming a sliding motion which would be the cause of the plasticity of the matrix. Moreover, time-dependent strain has also been observed in the argillite. The creep strain may be related to two basic phenomena: viscoplastic sliding of the clay matrix and sub-critical propagation of micro-cracks (Shao, 1999).

Additionally, it is noticed that the mechanical properties of argillite minerals are strongly contrasted (the Young modulus of quartz and calcite is in the order of 100GPa, while that of clay matrix is about 10GPa). In that manner, it can lead to high local deformation in the clay matrix with respected to those in the calcite and quartz grains (Fig. 1.8 (d)). This contrast induce shearing stress on the interface [Su, 2005a]

and may create micro-cracks by decohesion at the grains/matrix boundaries (Fig. 1.8 (a)) or trans-granular fractures (Fig. 1.8 (b), Vales, 2001). The cracking inside the grains are mainly visible in the calcite with a network of micro-cracks randomly oriented and almost uniformly distributed. In this study, to simplify the micromechanical modeling, we neglect the micro-cracking around the grain and the matrix. It is assumed that the micro-cracking exists and propagates only in the clay matrix.

1.3.3 Mechanical behavior

Numerous studies have been conducted by various laboratories on samples and in situ to characterize the mechanical behavior in the short and long-term. In this section, basic macroscopic behavior of argillite is summarized ([ANDRA, 2005b], [Chiarelli, 2000]), with a special emphasize on the interactions between the microstructure and mechanical behavior.

1.3.3.1 Mechanical behavior in short term

Chiarelli (Chiarelli, 2000) have performed hydrostatic and triaxial compression test in order to determine its mechanical properties (Young's modulus, uniaxial compressive

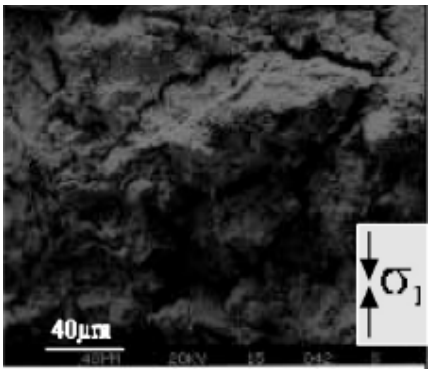

(a) Optical microscope photo.

The surface of rupture of a specimen after a uniaxial compression test. Note that the propagation of the cracks caused by the debonding of the grain.

[Chiarelli, 2000]

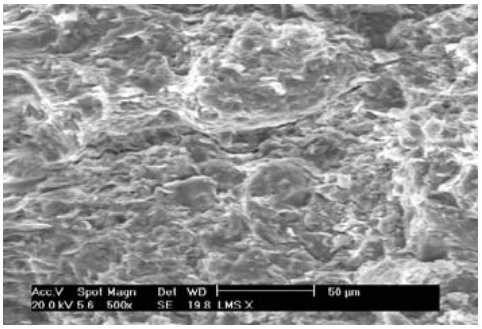

(b) SEM photo of the clay matrix

A crack passes through the specimen by appearing around the visible grains.

[Valès, 2001]

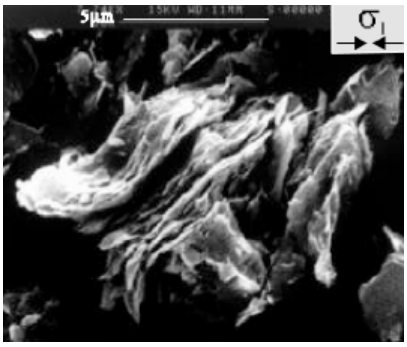

(c) Optical microscope photo
A cluster of minerals extruded by .a sliding movement
[Chiarelli, 2000]

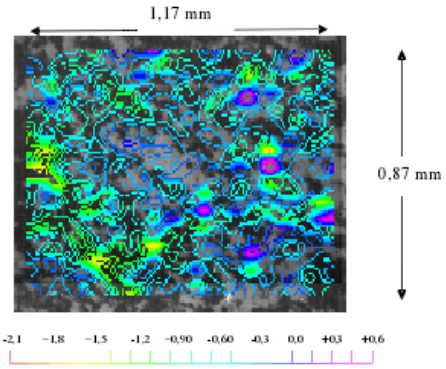

(d) Field of axial strain (in %) in a part of a argillite specimen under uniaxial compression of 43 MPa
[Bornert, 2001]

Fig 1.8 Micromechanism

strength, the volume dilation ...). The range of confining pressure varies form 0Mpa to 20Mpa, which was chosen according to the estimated value of in situ stress. In order to assurer the tests under quasi static condition, triaxial compression tests have been performed by axial strain controlled path with an average rate of $6\times10^{-6}s^{-1}$. The loading condition used for a triaxial test is the follows: $\Sigma=\Sigma_{11}(e_1\otimes e_1)+\Sigma_{22}(e_2\otimes e_2+e_3\otimes e_3)$, where Σ_{11} and Σ_{22} are negative en compression.

The Fig. 1.9 represents the different loading paths used in our study. Using the unloading-reloading cycles of deviatoric stress were included in each triaxial test (Fig.1.10 and Fig. 1.11), the progressive degradation of elastic stiffness and the macroscopic plastic deformation is observed. The stress-strain curves allow us to identify three important phenomena in the overall response of the argillite.

- Firstly, an elastic phase is noticed when the deviator stress is very small according to the rupture strength. A small anisotropy is demonstrated in the axial and lateral strains curves. Nevertheless it is assumed, in a first approach, the elastic, linear and isotropic initial behavior of the argillite. This linear phase is also observed in a hydrostatic test (Fig. 1.12) where the stress-strain curve is quasi linear without an obvious initiation of microcracking in material.

- Secondly, with the increase of deviatoric stress, the stress-strain curve becomes non-linear. Large residual strains are observed in both the axial and lateral

directions after unloading of deviatoric stress. Based on the microscopic analysis presented in previous sections, such irreversible strain are essentially relative plastic strains induced by clay sheet sliding. With the comparison of experimental results obtained on different geomechanical zone, one notice that the macroscopic plastic strain of argillite formation increase with the volumetric fraction of clay minerals (Fig. 1.10 and 1.11).

- Additionally, a progressive decrease of the elastic stiffness is obtained as a function of applied stress level. This degradation in the lateral direction is more important in the axial one. According to the analysis of microstructure of argillite formation, this degradation of elastic properties is considered as a consequence of induced damage by micro-cracks in clay matrix.

Finally, the influence of mineralogical composition on the mechanical behavior of argillite formation is studied. The macroscopic elastic modulus increases with calcite content while it decreases with clay content. Moreover, mineralogical composition has also an important influence on the plastic deformation and induced damage. That means that at the same stress level, the plastic strains decrease with calcite content increases, but become more important when quartz or clay content increase. The induced damage increases with calcite content. The increase of carbonate contents creates a non-negligible viscous behavior (long-term creep). The resistance of the argillite formations strongly depends on the volumetric fraction of carbonate in the argillites (Fig. 1.13).

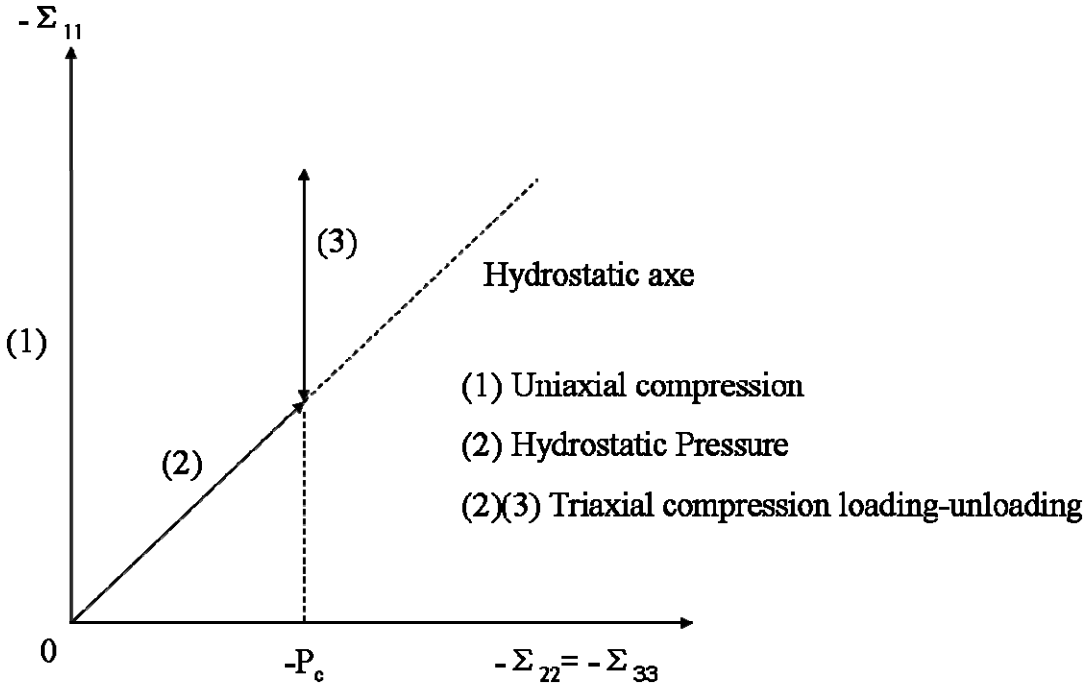

Fig 1.9 Loading paths

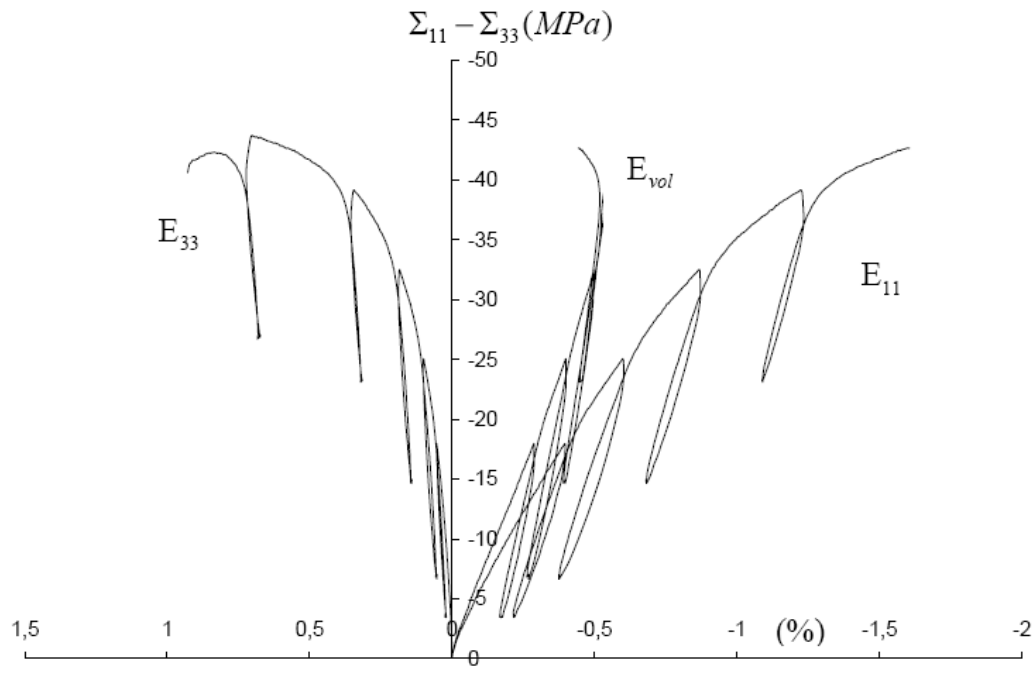

Fig 1.10 Uniaxial compression test with loading-unloading cycles [Chiarelli, 2000]
Depth: 466.9m (EST 104 02262-12)

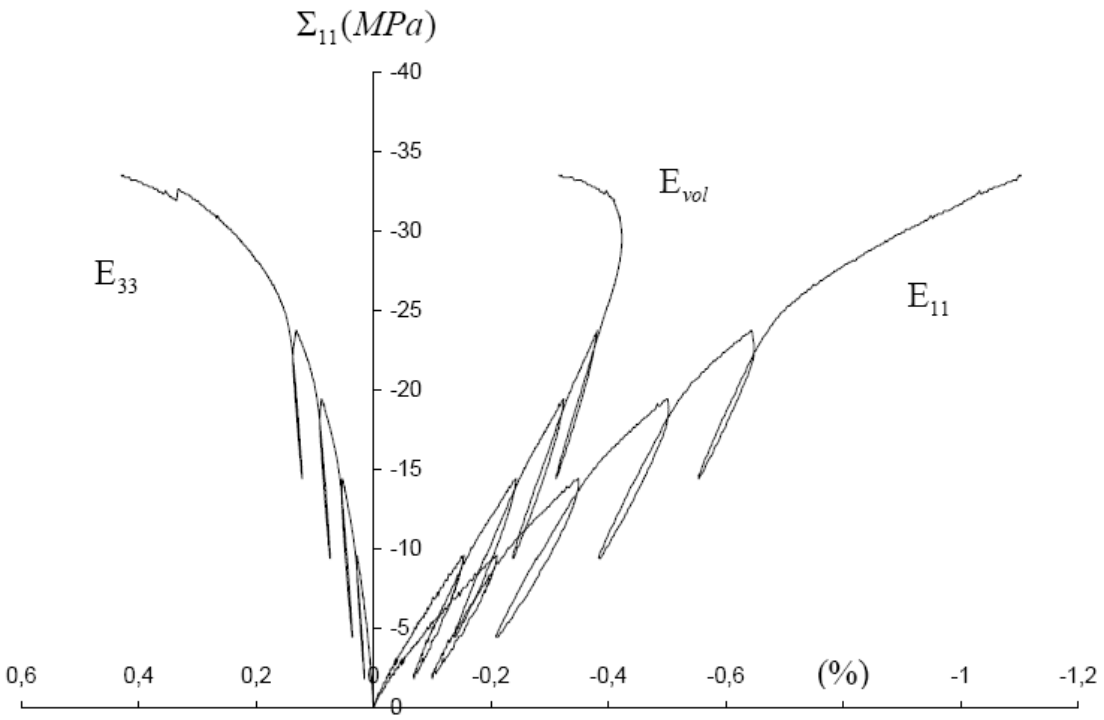

Fig 1.11 Triaxial compression test with loading-unloading cycles [Chiarelli, 2000]
Depth: 482.2m (EST 104 02354)

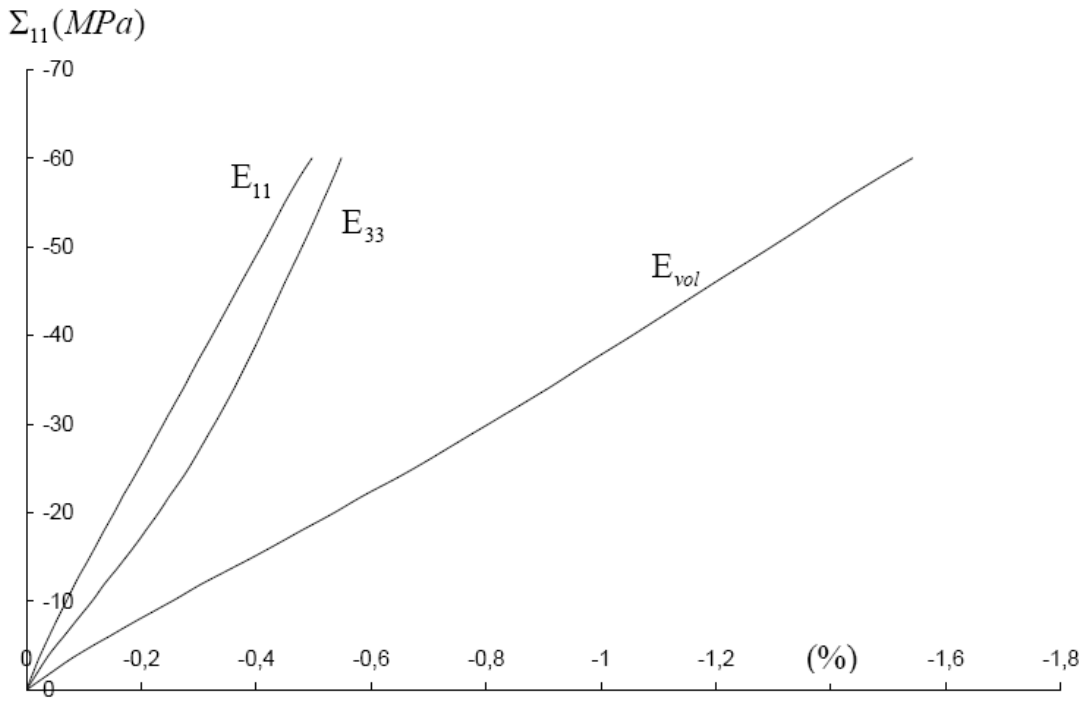

Fig 1.12 Hydrostatic pressure [Chiarelli, 2000]
Depth: 482.3m (EST 104 02354-22)

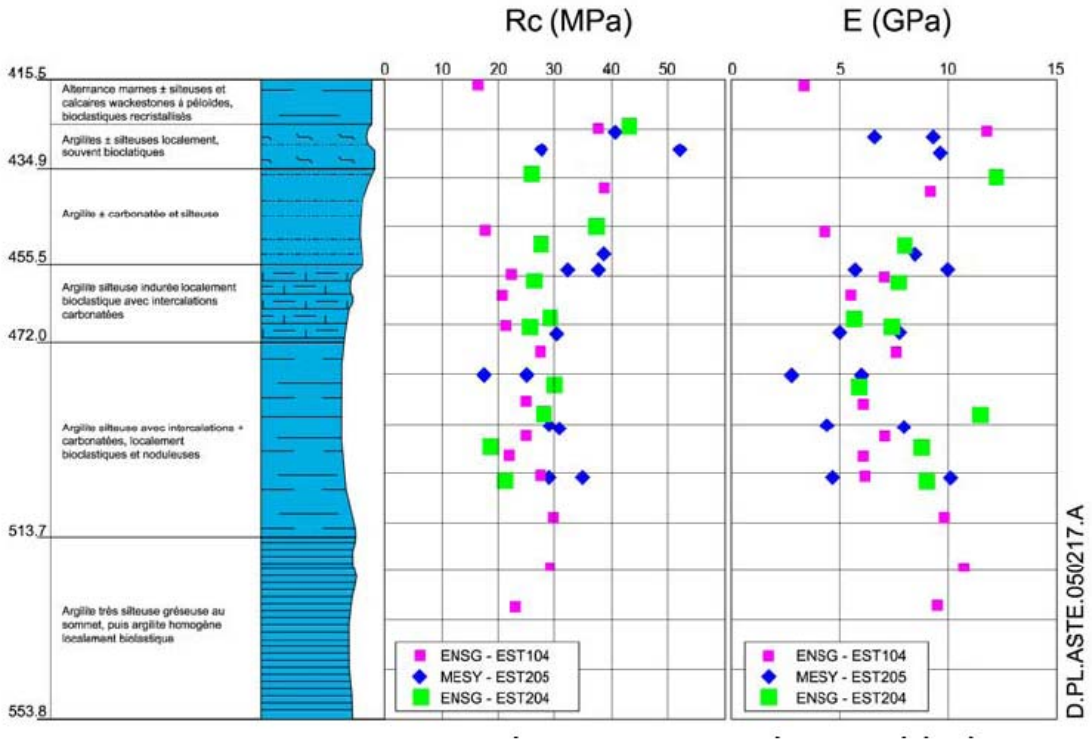

Fig 1.13 Uniaxial compressive strength and Young's modulus measured on samples as a function of vertical depth of the underground laboratory

1.3.3.2 Mechanical behavior in long term

In the context of underground repository, various mechanical, hydraulic, chemical and thermal may induce the time-dependent strains:

- The consolidation: decreases the volume over time with a drainage of the material (hydro-mechanical phenomenon);
- The swelling: increase in volume due to a chemical modification of the rock structure, such as the sorption of water molecules between the clay sheets, or the hydration of the anhydrite into gypsum;
- The creep: the time-dependant strains with the application of a constant load;
- The relaxation: relaxation of constraints at constant strain, which are related to the viscoplastic properties of the material;
- The ageing: degradation of mechanical properties induced by a chemical corruption of the constituent minerals of the rock;
- The cicatrization: the physico-chemical phenomena in which recrystallization of the rock recover its properties.

In the following section, the time-dependent behavior of argillite is studied by using some creep and stress relaxation tests. A creep test is carried out by applying a

constant load to a specimen and observing the increase in strain with time. Several test campaigns have been performed in order to study the time-dependent behavior of the argillite. The experimental results obtained on samples from the borehole EST205 (campaign of complementary investigations since 2000, Chanchole, 2004) is analyzed in this section. These creep tests are performed under different confining pressures and deviatroric stress under ambient temperature following an axial strain controlled path with an average rate of about 10^{-11} s^{-1}. The creep deformation rate depends on the applied stress level. Generally, with the increase of deviatoric stress, three distinct stages is identified:

- Stage I: Primary creep occurs at the beginning of the tests with a relatively high strain rate, but slows down with increasing time.
- Stage II: Secondary creep, the rate of creep becomes near constant. This stage is known as steady state creep;
- Stage III, or tertiary creep, the strain rate exponentially increases with stress till failure of material. The creep rate begins to accelerate as the cross sectional area of the specimen decreases due to necking or internal voiding decreases the effective area of the specimen. If stage III is allowed to proceed, fracture will occur.

According to the applied stress level, the different stages of creep are more or less pronounced in the experiment tests (Andra 2005). Thus, if the applied deviatoric tress does not exceed a certain limit (a stress value is equal to 50%~ 70% of the material strength), only the primary creep is observed. On the contrary, only the secondary creep and tertiary creep are shown in creep test. Consequently, the creep tests have been performed under different stress level (usually star with 50% of material compression strength at short term scale).

Additionally, several relaxation tests have been also performed [Zhang et al., 2002]. This type test consists to evaluate the stress evolution under a constant strain. In Figure 1.15, we observe that the stress decrease with time until its residual value corresponding to the upper limit of elasticity, known as" stabilization boundaries". Note also that the relaxation appears for an initial deviatoric stress 10 MPa and the relaxation stability very quickly, even at the end of three days.

Based on the microscopic analysis of argillite, the time dependant deformation in argillite is essentially relative to two basic phenomena: viscoplastic flow of the clay matrix, and subcritical propagation of microcracks at the inclusion/matrix interfaces and inside the clay matrix. The experimental observation exhibits the clay mineral

zones represent potentially more deformable. Consequently, the creep of the clay phase seems to be dominated and the process of pressure-dissolution of calcite plays a minor role on the short term scale. This does not exclude the possibility that the dissolution process becomes preponderant on long-term scale (beyond the century), but this requires that the creep strain rate related clay minerals becomes less than that created by the dissolution process.

Finally, the time-dependent behavior of the argillite may be affected by following phenomena:

- The viscous behavior of the clay matrix, which can be influenced by temperature and water content.
- Chemical-mechanical coupling. The chemically reactive environment can lead to stress corrosion in rock which induces the so-called sub-critical propagation of microcrack in the clay matrix [Anderson OL and al. 1977]. Subcritical crack growth is very important according to the generation of time-dependent behavior in argillites [Costin LS 1987].
- Hydraulic condition: The time-dependent behavior is induced purely by the hydraulic effect which is represented by the consecutive drainage of free water of a porous medium, following its reduction in volume caused by mechanical loading. However, for the argillite, the time-dependent strain related to water drainage is very limited due to the law permeability of material.

1.4 Conclusion

The experimental investigations show that the Callovo-Oxfordian argillite is a composite material mainly consisting of the quartz, calcite and clay minerals. This thesis focus on the long-term mechanic behavior of the Callovo-Oxfordian argillite, in addition to the viscoplastic deformation, it's worth noting that the subcritical crack growth is also one of main causes of time-dependent behavior in rock [Meredith, Atkinson. 1983]. In the 2nd chapter, we will test the relationship between the stress intensity factor and crack velocity, based on 3-point bending test and double torsion test, usually performed in fracture mechanics. In order to make a clearly explanation as to the physical mechanisms of creep deformation and furthermore to take into account influences of material microstructure on time-dependent behavior, based on Hill's incremental method, Abou-Chakra Guéry [Abou-Chakra Guéry et al., 2008] proposed a three phase composite model and Jiang [Jiang et al., 2009] proposed a two phase micromechanical model. In the 3rd chapter, a similar model considered the subcritical damage will be proposed. It's important to realize that, due to the

assumption of homogeneous distribution of the strain field in each phase, Hill's approach always leads to a too stiff response which would cause the accumulation of errors at each iteration step caused by the failure to adequately take account of the heterogeneity of the stain field in the phases. A suitable “isotropization procedure” will be thus necessary to apply the Hill type incremental homogenization method for the sake of making supple the predictions of the incremental method. Nevertheless, the so-called “isotropization procedure” doesn’t have any physical implication, for this reason, we need a “more rigorous” method which is able to consider the heterogeneity of the stain field within the phase.

Lahellec and Suquet [2007] proposed a new method based on incremental variational principles. Upon use of an implicit time-discretization scheme, the evolution equations describing the constitutive behavior of the phases can be reduced to the minimization of an incremental energy function. In the 4th chapter, we expand this model to apply for the geomaterials, more exactly, the Callovo-Oxfordian argillite. The characters of the geomaterials such as the dilatancy effect and the influence of confining pressure will be taken into account in the modified model. An isotropic and kinematic hardening effect is considered as well for the more general cases.

Chapter 2
Introduction of the homogenization methods

Résumé du chapitre

Le chapitre 2 présente l'homogénéisation du comportement des argilites en régime élastique. Le principe des méthodes de changement d'échelle est d'abord rappelé. Les schémas d'homogénéisation linéaires (schéma dilué, modèle Mori-Tanaka [Mori et Tanaka, 1973] et modèle autocohérent [Hill, 1965b]) ainsi que des bornes (bornes de Voigt et Reuss [Voigt, 1889; Reuss, 1929], bornes de Hashin et Shtrikman [Hashin et Shtrikman, 1962]) reposant sur les principes variationnels seront étudiés. Enfin, une introduction à une méthode d'homogénéisation du comportement non linéaire de l'argilite, l'approche incrémentale de Hill [Hill, 1965a], clôturera ce chapitre.

The first chapter of this memory has synthesized a certain number of specificities of the mechanical behavior of the argillite. The extent of the mineralogical composition of the material and the different mechanisms of deformation (plastic sliding in the clay matrix, intra and transgranular microcracking) on the scale of grain has been exposed. Therefore, the Callovo-Oxfordien argillite is treated as a nonlinear heterogeneous composite.

For estimating the macroscopic response of the nonlinear heterogeneous materials, two different techniques are usually applied: the direct finite element simulation (numerical approach) and the homogenization method (analytical approach). The direct numerical simulation consist in determining effective properties of linear or nonlinear heterogeneous materials by solving boundary values problems on the representative volumetric element (*r.v.e.*) by taking into account as close as possible the real microstructures of materials. The direct numerical simulations are generally computationally expensive compared with homogenization method. With homogenization method, the real microstructures of materials are described mathematically by the homogenization schemes as well as the macroscopic physical laws or the macroscopic material behaviors are derived from the ensemble average of massive micro-objects governed by the microscopic physical laws. This chapter focuses on some of the most fundamental homogenization methods for heterogeneous material, the linear homogenization schemes based on the Eshelby's equivalent eigenstrain theory and Hashin-Strikman variational principles will be introduced subsequently.

2.1 Separation of scales and representation of the representative volumetric element

The implementation of the homogenization method first requires identifying the different scales considered and the *r.v.e.* considered for the composite studied. Traditionally, in the field of micromechanics, two scales are distinguished if the heterogeneities are on a comparable scale:

- The macroscopic scale, which is that of the material point M of the continuum mechanics, it can be viewed as an ensemble microscope material space. We note that the volume is l, and the Cartesian coordinates of material point on the macroscopic scale is defined by $\mathbf{Z} = \left(Z_i \underline{e}_i \right)_{1 \le i \le 3}$.
- The microscopic scale is the local level where we distinguish the heterogeneity of the material. The Cartesian coordinates on this level is defined by $\mathbf{z} = \left(z_i \underline{e}_i \right)_{1 \le i \le 3}$

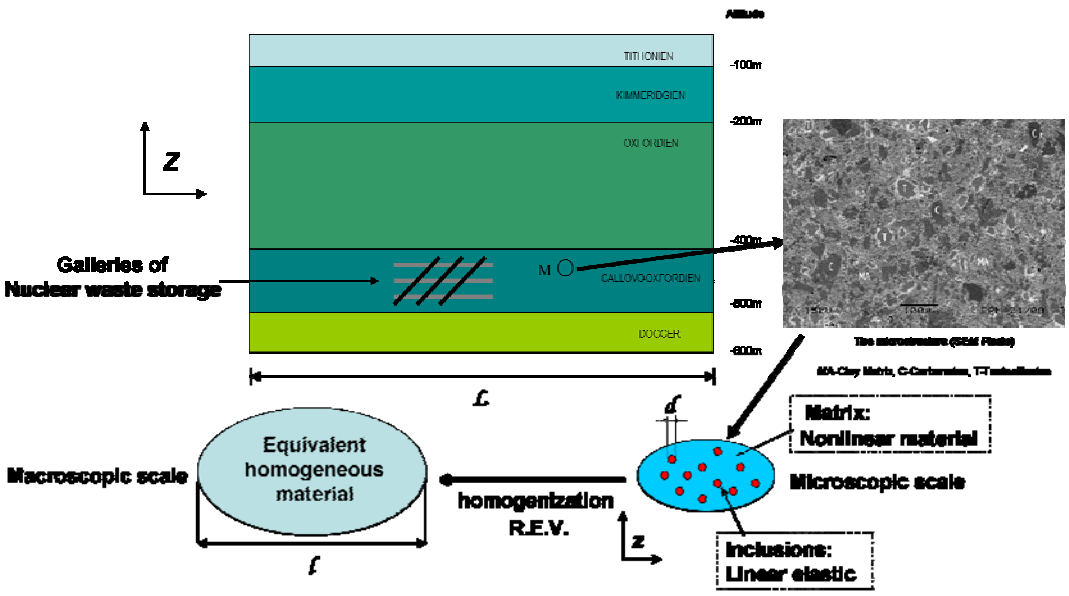

Fig.1. Macroscopic scale and Microscopic scale

In order to fulfill the usual conditions of separation of scales, it is assumed that the size of heterogeneities is sufficiently small compared to that of the *r.v.e.*, l. This results in $d \ll l$ (Fig.1). In the specific instance of argillite, the size of the heterogeneity is the order of $10\mu m$. In addition, the size of the *r.v.e.* must also be very small compared to that of the structure, $l \ll L$, in order that we can deal with the structure as a continuous medium. Again, for clarification, we know that for the argillite, the envisaged size of the storage structure is about a hundred meters. It can be concluded that the conditions of separation of scales may well be all verified by considering a following *r.v.e.* on the order of mm.

2.2 Boundary conditions

The representative volume element of material being defined, it is now necessary to clarify the boundary conditions of the problem of homogenization which will be studied. Two types of boundary conditions are generally considered in homogenization of medium with arbitrary microstructure: i) uniform stress on the boundary (Fig. 2 (b)); ii) uniform strain on the boundary (Fig. 2 (a)). For a detailed discussion of the issue of boundary conditions in homogenization, the reader can refer to (Zaoui, 2000) or (Bornert et al. 2001a). We adopt in this study the conditions of uniform strain on the boundary described in the following:

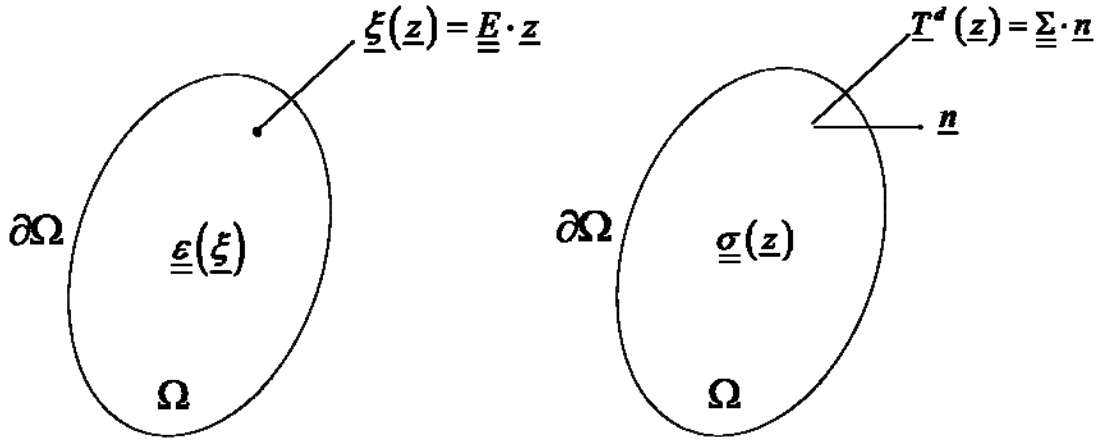

(a) uniform strain boundary condition (b) uniform stress boundary condition

Fig. 2. Boundary conditions

Ω denotes the geometrical domain occupied by the *r.v.e.* and $\partial\Omega$ the boundary of this domain. The uniform strain boundary condition on $\partial\Omega$ is written as:

$$\forall \mathbf{z} \in \partial\Omega, \quad \boldsymbol{\xi}(\mathbf{z}) = \mathbf{E} \cdot \mathbf{z} \tag{1}$$

in which ξ represents the displacement vector.

Upon the condition (2.1), we demonstrated that the volumetric average of microscopic stains $\boldsymbol{\varepsilon}$ is equal to the macroscopic strain $\mathbf{E}$:

$$\langle \boldsymbol{\varepsilon} \rangle_\Omega = \frac{1}{\Omega} \int_\Omega \boldsymbol{\varepsilon} d\Omega = \mathbf{E} \tag{2}$$

For the coherence of the mechanical energy, we define the macroscopic stress as the volumetric average of the microscopic stress field:

$$\langle \boldsymbol{\sigma} \rangle_\Omega = \frac{1}{\Omega} \int_\Omega \boldsymbol{\sigma} d\Omega = \boldsymbol{\Sigma} \tag{3}$$

2.3 Determination of the macroscopic elasticity

At this stage, it is assumed that all phases of the heterogeneous material have linear elastic behavior. The equations of the homogenization problem are then as follows:

- static equilibrium

$$div(\boldsymbol{\sigma}) = \mathbf{0} \tag{4}$$

- linear elastic constitutive law

$$\boldsymbol{\sigma}(\mathbf{z}) = \mathbb{C}(\mathbf{z}) : \boldsymbol{\varepsilon}(\mathbf{z}) \tag{5}$$

where $\mathbb{C}(\mathbf{z})$ represents the elasticity tensor at point $\mathbf{z}$

- compatibility condition

$$\underline{\underline{\varepsilon}} = \frac{1}{2}\left[\underline{\underline{grad}}\,\underline{\xi} + \left(\underline{\underline{grad}}\,\underline{\xi}\right)^T \right] \tag{6}$$

- boundary condition

$$\forall \mathbf{z} \in \partial\Omega, \quad \boldsymbol{\xi}(\mathbf{z}) = \mathbf{E} \cdot \mathbf{z} \tag{7}$$

The linearity of the equations of the problem implies the existence of a linear relationship between the fields of microscopic and macroscopic deformations. We then introduce a localization tensor $\mathbb{A}$ such as:

$$\forall \mathbf{z} \in \Omega, \quad \boldsymbol{\varepsilon}(\mathbf{z}) = \mathbb{A}(\mathbf{z}) : \mathbf{E} \tag{8}$$

Note that the localization tensor (8) is such that $\langle \mathbb{A} \rangle = \mathbb{I}$, reflecting the fact that the average of the microscopic strain is equal to the macroscopic strain. $\mathbb{I}$ denotes the fourth-order identity tensor: $\mathbb{I} = \frac{1}{2}\left(\delta_{ik}\delta_{jl} + \delta_{il}\delta_{jk}\right)$ with δ_{ij} the Kronecker symbol. Combining the localization relationship (8), the constitutive law of local constituents and taking the spatial average, we obtain the classical result:

$$\boldsymbol{\Sigma} = \mathbb{C}^{\text{hom}} : \mathbf{E} \quad \text{with} \quad \mathbb{C}^{\text{hom}} = \langle \mathbb{C} : \mathbb{A} \rangle \tag{9}$$

where $\mathbb{C}^{\text{hom}}$ is the homogenized elasticity tensor defining the macroscopic elastic constitutive law of heterogeneous material considered. If the material consists of clearly differentiated N phases, it is sufficient to know the averages $\mathbb{A}$ of each phase r, the behavior being given by:

$$\mathbb{C}^{\text{hom}} = \sum_{r=0}^{N} f_r \mathbb{C}_r : \mathbb{A}_r \tag{10}$$

where f_r represents the volume fraction of the phase r.

We can rewrite the expression (10) in the following form:

$$\mathbb{C}^{\text{hom}} = \mathbb{C}_0 + \sum_{r=1}^{N} f_r \left(\mathbb{C}_r - \mathbb{C}_0\right) : \mathbb{A}_r \quad \text{with} \quad \sum_{r=0}^{N} f_r = 1 \tag{11}$$

$\mathbb{C}_0$ is the elasticity tensor of the matrix.

2.4 Determining the effective behavior of composites

There are three categories of methods to determine the effective behavior of composites:

1) First, as good estimations of overall mechanical properties, we have techniques of estimating the overall mechanical properties based on generalizations of the Eshelby method. We can mention the dilute scheme [Eshelby, 1957], the Mori-Tanaka method [Mori and Tanaka, 1973], the self-consistent model [Hill, 1965b], etc.
2) Second, we consider exact solutions and theorem that deliver variational bounds, on the overall constitutive parameters. We can mention Voigt [Voigt, 1889] and Reuss [Reuss, 1929] bounds, Hashin-Strikman bounds[Hashin and Strikman, 1962].
3) Third, numerical techniques, most often are often limited to the quasi-periodic situations. Moreover, their cost is really high and their direct use inside a true structural analysis is presently limited to very special cases.

The scope of this chapter is to present the schemes of estimations and variational bounds which will use later to describe the non linear behavior of the Callovo-Oxfordian argillite.

2.4.1 Homogenization schemes

To determine the average $\mathbb{A}$ of each phase r, we introduce briefly in this section the linear homogenization schemes usually considered for a random microstructure medium: dilute scheme, Mori-Tanaka method, self-consistent model. Each of these schemes provides an estimate of the macroscopic elasticity tensor $\mathbb{C}^{\text{hom}}$ based on the Eshelby's equivalent eigenstrain theory (the so-called Eshelby problem) [Eshelby, 1957].

2.4.1.1 Dilute scheme

The dilute estimates of the macroscopic properties correspond to the simplest situation in which the second phase concentration or other phase concentrations are small in comparison with the concentration of the matrix. This scheme is based on the solution provided by Eshelby (Eshelby, 1957) to the problem of an ellipsoidal inhomogeneous inclusion with elasticity modulus $\mathbb{C}_r$ plunged into an infinite matrix

with elasticity modulus $\mathbb{C}_0$, subject to a homogeneous strain at infinity $\underline{\underline{E}}^{\infty}$. The solution of the Eshelby problem indicates that the strain is uniform in the inclusion when it is ellipsoidal in shape and is given by:

$$\boldsymbol{\varepsilon}_r = \left(\mathbb{I} + \mathbb{P}^0_{\mathrm{I}r} : \left(\mathbb{C}_r - \mathbb{C}_0\right)\right)^{-1} : \mathbf{E}^{\infty} \tag{12}$$

where $\mathbb{P}^0_{\mathrm{I}r}$ is the microstructural tensor (or so-called Hill tensor), fourth-order tensor with the symmetries: $P_{ijkl} = P_{jikl} = P_{ijlk} = P_{klij} = P_{lkji}$. Note that the exponent 0 is well reference to the elasticity modulus $\mathbb{C}_0$ and $\mathbb{I}r$ refers to the dependence of $\mathbb{P}$ with the shape and direction of inclusion. The general expression of $\mathbb{P}$ which thus depends on the geometry of the inclusion and properties of the reference medium can be written with the aid of the Green function $\mathbf{G}^0_{\infty}$ as:

$$P^0_{\mathrm{I}_r injk} = -\left(\int_{\mathrm{I}_r} G^0_{\infty ij}\left(\mathbf{x}-\mathbf{y}\right) dy\right)_{kl_{(il)(jk)}} \qquad \forall \mathbf{x} \in \mathbb{I}_r \text{, ellipsoid} \tag{13}$$

where the notation $(il)(jk)$ indicates symmetrization over indices i and l on one hand and j and k on the other hand.

For spherical inclusion and given the hypothesis of local and global isotropy, the Hill tensor has the following analytical formulation:

$$\mathbb{P}^0_{\mathrm{I}_r} = \frac{\beta_0}{2\mu_0}\mathbb{K} + \frac{\alpha_0}{3k_0}\mathbb{J} \tag{14}$$

with $\alpha_0 = \dfrac{3k_0}{3k_0 + 4\mu_0}$ and $\beta_0 = \dfrac{6\left(k_0 + 2\mu_0\right)}{5\left(3k_0 + 4\mu_0\right)}$.

The modules k_0 and μ_0 represent respectively the bulk and shear modulus of the clay matrix.

Can be noted that in the next chapter the matrix has an anisotropic module (the analytical expression of Green's function then not necessarily known), we shall employ an alternative approach that is used to express the tensor $\mathbb{P}$ in the form of an integral over the unit sphere ([Kinoshita and Mura, 1971], [Faivre, 1971] and [Willis, 1977]).

$$\mathbb{P}^0_{\mathrm{I}_r} = \frac{\det\left(\mathbf{Z}^0_{\mathrm{I}_r}\right)}{4\pi}\int_{|\xi|=1} H_0\left(\xi\right)\left|\mathbf{Z}^0_{\mathrm{I}_r}\xi\right|^{-3} dS \tag{15}$$

with $K^0_{ik} = C^0_{ijkl}\xi_j\xi_l$, $N^0_{ij} = (K^0_{ij})^{-1}$ and $H^0_{ijkl}\left(\underline{\xi}\right) = N^0_{ik}\xi_j\xi_l$. The tensor $\mathbf{Z}$ characterized the geometric of the ellipsoid is equal to the second-order identity tensor in the case of spherical inclusions. The tensor $\mathbb{P}^0_{\mathrm{I}_r}$ is then evaluated using a procedure of Gauss type integration (numerical):

$$\mathbb{P}^0_{\mathrm{I}_r} = \frac{1}{4\pi}\sum_{n=1}^{M}\varpi_p H_0\left(\xi_p\right)\left|\xi_p\right|^{-3} \tag{16}$$

where M is the number of integration points and ϖ_p the weight associated with the *n*th integration point. The directions and the weights correspond to the integration schemes with 21, 33, 37 or 61 integration points spread out over half a unit sphere are given in Bazant and Oh [Bazant and Oh, 1986]. We selected the schema with 33 points which seems to provide a good correspondence between precision and computation (see for example [Pensee et al., 2002]).

It is now to determine the localization tensor for the dilute scheme. The latter being dedicated to the situation or the phases, in low concentrations, do not interact with each other, it is permissible to consider that:

$$\mathbf{E}^{\infty} \cong \mathbf{E} \tag{17}$$

and upon the relation (8), we adopt (12) as location tensor:

$$\mathbb{A}_r = \left(\mathbb{I} + \mathbb{P}^0_{\mathrm{I}_r} : \left(\mathbb{C}_r - \mathbb{C}_0\right)\right)^{-1} \tag{18}$$

From which we deduce in (11), the expression of the macroscopic elasticity tensor for a matrix containing N families of inclusions in low concentrations is given as:

$$\mathbb{C}^{\mathrm{hom}} = \mathbb{C}_0 + \sum_{r=1}^{N} f_r\left[\left(\mathbb{C}_r - \mathbb{C}_0\right)^{-1} + \mathbb{P}^0_{\mathrm{I}_r}\right]^{-1} \tag{19}$$

Using equation (19), the macroscopic compression and shear modules derived from the dilute scheme are written

$$k^{\mathrm{hom}} = k_0 + \sum_{r=1} f_r \frac{\left(k_r - k_0\right)\left(3k_0 + 4\mu_0\right)}{3k_r + 4\mu_0} \tag{20}$$

$$\mu^{\mathrm{hom}} = \mu_0 + \sum_{r=1} f_r \frac{5\mu_0\left(\mu_r - \mu_0\right)\left(3k_0 + 4\mu_0\right)}{\mu_0\left(9k_0 + 8\mu_0\right) + 6\mu_r\left(k_0 + 2\mu_0\right)} \tag{21}$$

2.4.1.2 Mori-Tanaka method

We now consider a distribution of ellipsoidal inclusions N families such that it is no longer possible to neglect the interactions. The main idea of the Mori-Tanaka method [Mori and Tanaka, 1973] is to simplify the localization problem in representing the inclusions of the same shape, orientation and elastic behavior, such equivalent single ellipsoidal inclusion is embedded in an infinite medium with elasticity modulus of the matrix $\mathbb{C}_0$ and subjected at infinity to a uniform stain field $\mathbf{E}^0$ to be determined. Then based on the Eshelby solution, the strain in a phase "r" is written:

$$\boldsymbol{\varepsilon}_r = \left(\mathbb{I} + \mathbb{P}_{\mathrm{I}r}^0 : \left(\mathbb{C}_r - \mathbb{C}_0\right)\right)^{-1} : \mathbf{E}^0 \tag{22}$$

where as previously $\mathbb{I}_r$ defines the geometry of the rth family of inclusions whose elastic moduli is $\mathbb{C}_r$.

It can be shown that the deformation $\mathbf{E}^0$ is given, based on the rule of average $\langle\boldsymbol{\varepsilon}\rangle = \mathbf{E}$, by:

$$\mathbf{E}^0 = \left(\sum_{r=0}^{N} f_r \left(\mathbb{P}_{\mathrm{I}_r}^0 : \left(\mathbb{C}_r - \mathbb{C}_0\right)^{-1} + \mathbb{I} \right)^{-1} \right) : \mathbf{E} \tag{23}$$

It should be noted then $\mathbb{A}_r^0 = \left(\mathbb{P}_{\mathrm{I}_r}^0 : \left(\mathbb{C}_r - \mathbb{C}_0\right)^{-1} + \mathbb{I}\right)^{-1}$ for easy in writing. Hence we deduce the localization tensor for the rth inclusions:

$$\mathbb{A}_r = \mathbb{A}_r^0 : \left(\sum_{s=0}^{N} f_s \mathbb{A}_s^0 \right)^{-1} \tag{24}$$

and consequently the macroscopic elasticity tensor:

$$\mathbb{C}^{\mathrm{hom}} = \sum_{r=0} f_r \mathbb{C}_r : \mathbb{A}_r = \sum_{r=0} f_r \mathbb{C}_r : \mathbb{A}_r^0 \left(\sum_{s=0}^{N} f_s \mathbb{A}_s^0 \right)^{-1} \tag{25}$$

which is also written as:

$$\mathbb{C}^{\mathrm{hom}} = \mathbb{C}_0 + \sum_{r=1} f_r \left[\left(\mathbb{C}_r - \mathbb{C}_0\right)^{-1} + \mathbb{P}_{\mathrm{I}_r}^0 \right]^{-1} \left(\sum_{s=0}^{N} f_s \mathbb{A}_s^0 \right)^{-1} \tag{26}$$

Comparison of (26) with the dilute estimate (19) shows that taking into account the interactions between phases is through the quantity $(\sum_{s=0}^{N} f_s \mathbb{A}_s^0)^{-1}$ in which all the phases involve.

According to (26), the macroscopic compression and shear modules from the Mori-Tanaka method are given by:

$$k^{\hom} = \left(\sum_{r=0} f_r \frac{k_r}{3k_r + 4\mu_0} \right) \left(\sum_{s=0} \frac{f_s}{3k_s + 4\mu_0} \right)^{-1} \tag{27}$$

$$\mu^{\hom} = \frac{\sum_{r=1} f_r \dfrac{\mu_r}{\mu_0 (9k_0 + 8\mu_0) + 6\mu_r (k_0 + 2\mu_0)}}{\sum_{s=1} \dfrac{f_s}{\mu_0 (9k_0 + 8\mu_0) + 6\mu_s (k_0 + 2\mu_0)}} \tag{28}$$

It is worth noting that the Mori-Tanaka method is particularly well suited to the situations of a matrical type morphology (the matrix is the phase 0 in which the inclusions are plunged). In the case of granular type morphology, the best homogenization scheme seems to be that provided by the self-consistent model.

2.4.1.3 Self-consistent model

As just mentioned, the self-consistent model is generally considered for the polycrystalline microstructures: there is no clearly identified matrix phase and all phases play a similar role. The general idea is to replace the localization problem relative to a grain family r of the same orientation, characterized by a module tensor $\mathbb{C}_r$, and of the same considerably ellipsoidal geometry $\mathbb{I}_r$ by the inclusion problem derived from that of Eshelby. The inclusion is embedded in an infinite medium with homogenized elastic properties $\mathbb{C}^{\hom}$ and subjected to a uniform loading $\mathbf{E}^{\infty}$ at infinity.

$$\boldsymbol{\varepsilon}_r = \left(\mathbb{I} + \mathbb{P}_{\mathrm{I}_r}^{\hom} : \left(\mathbb{C}_r - \mathbb{C}^{\hom} \right) \right)^{-1} : \mathbf{E}^{\infty} \tag{29}$$

Proceeding in a manner similar to the Mori-Tanaka model, we obtain an implicit equation to determining $\mathbb{C}^{\hom}$:

$$\mathbb{C}^{\hom} = \sum_{r=0} f_r \mathbb{C}_r : \mathbb{A}_r^{\hom} \left(\sum_{s=0}^{N} f_s \mathbb{A}_s^{\hom} \right)^{-1} \tag{30}$$

$$\mathbb{A}_r^{\hom} = \left(\mathbb{P}_{\mathrm{I}_r}^{\hom} : \left(\mathbb{C}_r - \mathbb{C}^{\hom} \right)^{-1} + \mathbb{I} \right)^{-1} \tag{31}$$

In the case of the polycrystalline with inclusions of the same shape and same orientation, the equation is simplified by the fact that $\mathbf{E}$ is equal to the macroscopic stain $\mathbf{E}^{\infty}$. It derives:

$$\left(\sum_{s=0}^{N} f_s \mathbb{A}_s^{\text{hom}}\right)^{-1} = \mathbb{I} \tag{32}$$

and hence the tensor $\mathbb{C}^{\text{hom}}$:

$$\mathbb{C}^{\text{hom}} = \sum_{r=0} f_r \mathbb{C}_r : \mathbb{A}_r^{\text{hom}} \tag{33}$$

where $\mathbb{A}_r^{\text{hom}}$ was given by (31).

With expression (33), the macroscopic compression and shear modules from the self-consistent model are known as:

$$k^{\text{hom}} = \sum_{r=0} f_r \frac{k_r\left(3k^{\text{hom}} + 4\mu^{\text{hom}}\right)}{3k_r + 4\mu^{\text{hom}}} \tag{34}$$

$$\mu^{\text{hom}} = \sum_{r=0} f_r \frac{5\mu_r\mu^{\text{hom}}\left(3k^{\text{hom}} + 4\mu^{\text{hom}}\right)}{\mu^{\text{hom}}\left(9k^{\text{hom}} + 8\mu^{\text{hom}}\right) + 6\mu_r\left(k^{\text{hom}} + 2\mu^{\text{hom}}\right)} \tag{35}$$

The implicit character of (33) makes the self consistent model of employment more difficult than the Mori-Tanaka method. The recourse of iterative algorithms such as the fixed point method is often indispensable.

2.4.2 Variational principles

2.4.2.1 Voigt bound

Consider a linear elastic solid, V. The total potential energy of the elastic solid is:

$$\begin{aligned}\Pi(u_i) &= \frac{1}{2}\int_V \sigma_{ij}\varepsilon_{ij}dV - \int_V f_i u_i dV - \int_{\Gamma_t} t_i^0 u_i dS \\ &= \frac{1}{2}\int_V C_{ijkl}u_{i,j}u_{k,l}dV - \int_V f_i u_i dV - \int_{\Gamma_t} t_i^0 u_i dS\end{aligned}$$

with the following boundary conditions:

natural boundary condition $\quad t_i = \sigma_{ij}n_j = t_i^0 = \varepsilon_{ij}^0 x_j, \qquad \forall \mathbf{x} \in \Gamma_t \tag{36}$

essential boundary condition $\quad u_i = u_i^0, \qquad \forall \mathbf{x} \in \Gamma_u \tag{37}$

The displacement boundary conditions are essential boundary conditions for ensuring variational principles, and a necessary condition that $\Pi(u_i)$ reaches to an extreme is the stationary condition of its first variation with respect to function u_i:

$$\delta\Pi(u_i, \delta u_i) = \int_V C_{ijkl}u_{i,j}\delta u_{k,l}dV - \int_V f_i \delta u_i dV - \int_{\Gamma_t} t_i^0 \delta u_i dS = 0 \tag{38}$$

which is often called virtual displacement principle in solid mechanics.
The expression (38) can be easily proved via integration by parts,

$$\begin{aligned}\delta\Pi\left(u_i,\delta u_i\right) &= \int_V \sigma_{ij}\delta u_{i,j}dV - \int_V f_i\delta u_i dV - \int_{\Gamma_t} t_i^0\delta u_i dS \\ &= \int_V\left[\left(\sigma_{ij}\delta u_i\right)_{,j} - \sigma_{ij,j}\delta u_i\right]dV - \int_V f_i\delta u_i dV - \int_{\Gamma_t} t_i^0\delta u_i dS \\ &= \int_{\partial V}\sigma_{ij}n_j\delta u_i dS - \int_V\left(f_i+\sigma_{ij,j}\right)\delta u_i dV - \int_{\Gamma_t} t_i^0\delta u_i dS \\ &= \int_{\Gamma_t}\left(\sigma_{ij}n_j - t_i^0\right)\delta u_i dS - \int_V\left(f_i+\sigma_{ij,j}\right)\delta u_i dV\end{aligned} \tag{39}$$

which yields the condition of static equilibrium and the natural boundary condition, respectively:

$$\begin{aligned} f_i+\sigma_{ij,j} &= 0 \qquad \forall\mathbf{x}\in V \\ \sigma_{ij}n_j - t_i^0 &= 0 \qquad \forall\mathbf{x}\in\Gamma_t\end{aligned} \tag{40}$$

Now, the perturbance of the potential energy $\Delta\Pi\left(u_i,\delta u_i\right)$ can be expressed as follows:

$$\begin{aligned}\Delta\Pi\left(u_i,\delta u_i\right) &= \Pi\left(u_i+\delta u_i, u_{i,j}+\delta u_{i,j}\right) - \Pi\left(u_i,u_{i,j}\right) \\ &= \frac{1}{2}\int_V C_{ijkl}\left(u_{i,j}+\delta u_{i,j}\right)\left(u_{k,l}+\delta u_{i,j}\right)dV \\ &\quad -\int_V f_i\left(u_i+\delta u_i\right)dV - \int_{\Gamma_t} t_i^0\left(u_i+\delta u_i\right)dS - \frac{1}{2}\int_V C_{ijkl}u_{i,j}u_{k,l}dV \\ &\quad -\int_V f_i u_i dV - \int_{\Gamma_t} t_i^0 u_i dS \\ &= \int_V C_{ijkl}u_{i,j}\delta u_{k,l}dV - \int_V f_i\delta u_i dV - \int_{\Gamma_t} t_i^0\delta u_i dS + \frac{1}{2}\int_V C_{ijkl}\delta u_{i,j}\delta u_{i,j}dV \\ &= \delta\Pi + \frac{1}{2}\delta^2\Pi\end{aligned} \tag{41}$$

For the stationary condition (38), $\delta\Pi = 0$, then $\Delta\Pi(u_i,\delta u_i) = (1/2)\delta^2\Pi > 0$. It means that $\Pi(u_i,\delta u_i)$ is not only stationary, but also the global minimum. Therefore, the minimum potential energy principle is expressed as: among all kinematically admissible displacement fields $\mathbf{u}$, the real displacement field $\tilde{\mathbf{u}}$ makes the potential energy functional an absolute minimum.
If macroscopic strain boundary condition is applied on entire boundary ∂V,

$$\mathbf{u} = \mathbf{x}\cdot\mathbf{E} \qquad \mathbf{x}\in\partial V \tag{42}$$

where $\mathbf{E}$ is macroscopic strain field and the average of each admissible local strain

field $\boldsymbol{\varepsilon}$ over V must be satisfied the condition: $\mathbf{E}=\langle\boldsymbol{\varepsilon}\rangle_V$.

Then $\Gamma_t=\emptyset$ and $\Pi(\mathbf{u})=V\times W(\boldsymbol{\varepsilon})$, where:

$$W(\boldsymbol{\varepsilon})=\frac{1}{2V}\int_V C_{ijkl}\varepsilon_{ij}\varepsilon_{kl}dV \tag{43}$$

The minimum potential energy principle reads as:

$$W(\tilde{\boldsymbol{\varepsilon}})=\inf_{\mathbf{u}\in V}W(\boldsymbol{\varepsilon}) \tag{44}$$

For the real solution $\tilde{\boldsymbol{\varepsilon}}$,

$$W(\tilde{\boldsymbol{\varepsilon}})=\frac{1}{2V}\int_V\boldsymbol{\sigma}\cdot\boldsymbol{\varepsilon}dV=\frac{1}{2}\langle\tilde{\boldsymbol{\sigma}}\rangle_V\cdot\langle\tilde{\boldsymbol{\varepsilon}}\rangle_V=\frac{1}{2}\mathbf{E}:\mathbb{C}^{\text{hom}}:\mathbf{E} \tag{45}$$

On the other hand,

$$W(\boldsymbol{\varepsilon})=\frac{1}{2V}\int_V\boldsymbol{\sigma}\cdot\boldsymbol{\varepsilon}dV=\frac{1}{2}\langle\boldsymbol{\sigma}\rangle_V\cdot\langle\boldsymbol{\varepsilon}\rangle_V=\frac{1}{2}\left(\sum_{r=1}^{n}f_r\mathbb{C}_r:\langle\boldsymbol{\varepsilon}\rangle_r\right):\mathbf{E} \tag{46}$$

with $\langle\boldsymbol{\varepsilon}\rangle_r$ the average of local stain field in the phase r. We set that the localisation tensor of strain field $\mathbb{A}=\mathbb{I}$ for every point x in V, then we have $\langle\boldsymbol{\varepsilon}\rangle_r=\mathbf{E}$, it leads:

$$W(\boldsymbol{\varepsilon})=\frac{1}{2}\mathbf{E}:\left(\sum_{r=1}^{n}f_r\mathbb{C}_r\right):\mathbf{E} \tag{47}$$

According to (44), we have:

$$\mathbf{E}:\mathbb{C}^{\text{hom}}:\mathbf{E}<\mathbf{E}:\left(\sum_{r=1}^{n}f_r\mathbb{C}_r\right):\mathbf{E} \tag{48}$$

Then the so-called Voigt bound (upper bound) is known as:

$$\mathbb{C}^{\text{hom}}<\sum_{r=1}^{n}f_r\mathbb{C}_r \tag{48}$$

2.4.2.2 Reuss bound

Considering the following complementary potential energy:

$$\Pi_c(\sigma_{ij})=\frac{1}{2}\int_V D_{ijkl}\sigma_{i,j}\sigma_{k,l}dV-\int_{\Gamma_u}u_i\sigma_{ij}n_jdS \tag{49}$$

with the following boundary conditions:

natural boundary condition $\quad u_i=u_i^0, \qquad \forall\mathbf{x}\in\Gamma_u$ (50)

essential boundary condition $\quad t_i=\sigma_{ij}n_j=t_i^0=\varepsilon_{ij}^0x_j, \qquad \forall\mathbf{x}\in\Gamma_t$ (51)

The perturbance of the potential energy $\Delta\Pi_c(u_i,\delta u_i)$ is given by:

$$\begin{aligned}\Delta\Pi_c\left(\sigma_{ij},\delta\sigma_{ij}\right)&=\Pi\left(\sigma_{ij}+\delta\sigma_{ij}\right)-\Pi\left(\sigma_{ij}\right)\\&=\frac{1}{2}\int_V D_{ijkl}\left(\sigma_{ij}+\delta\sigma_{ij}\right)\left(\sigma_{kl}+\delta\sigma_{kl}\right)dV-\int_{\Gamma_u}u_i\left(\sigma_{ij}+\delta\sigma_{ij}\right)n_j dS\\&\quad-\frac{1}{2}\int_V D_{ijkl}\sigma_{ij}\sigma_{kl}dV-\int_{\Gamma_u}u_i\sigma_{ij}n_j dS\\&=\int_V D_{ijkl}\sigma_{ij}\delta\sigma_{ij}dV-\int_{\Gamma_u}u_i\delta\sigma_{ij}n_j dS+\frac{1}{2}\int_V D_{ijkl}\delta\sigma_{ij}\delta\sigma_{kl}dV\\&=\delta\Pi_c+\frac{1}{2}\delta^2\Pi_c\end{aligned}\tag{52}$$

The necessary condition for $\Pi_c\left(\sigma_{ij}\right)$ attaining extreme value is the stationary condition,

$$\delta\Pi_c=0\tag{53}$$

Then,

$$\Delta\Pi_c\left(\sigma_{ij}\right)=\frac{1}{2}\delta^2\Pi_c>0\tag{54}$$

Hence the minimum complementary potential energy principle is expressed as: among all statically admissible stress fields $\boldsymbol{\sigma}$, the real displacement field $\tilde{\boldsymbol{\sigma}}$ makes the complementary potential energy functional an absolute minimum, *i.e.*

$$\Pi_c\left(\tilde{\boldsymbol{\sigma}}\right)<\Pi_c\left(\boldsymbol{\sigma}\right),\qquad\forall\mathbf{x}\in V\tag{55}$$

If macroscopic stress boundary condition is applied on entire boundary ∂V,

$$\mathbf{t}=\mathbf{n}\cdot\boldsymbol{\Sigma}\qquad\mathbf{x}\in\partial S\tag{56}$$

where $\boldsymbol{\Sigma}$ is macroscopic stree field and the average of each admissible local stress field $\boldsymbol{\sigma}$ over V must be satisfied the condition: $\boldsymbol{\Sigma}=\left\langle\boldsymbol{\sigma}\right\rangle_V$.

Then $\Gamma_u=\emptyset$ and $\Pi_c\left(\boldsymbol{\sigma}\right)=V\times W_c\left(\boldsymbol{\sigma}\right)$, where:

$$W_c\left(\boldsymbol{\sigma}\right)=\frac{1}{2V}\int_V D_{ijkl}\sigma_{ij}\sigma_{kl}dV\tag{57}$$

is the complementary energy density.

The minimum complementary potential energy principle reads as:

$$W_c\left(\tilde{\boldsymbol{\sigma}}\right)=\inf_{\mathbf{u}\in V}W_c\left(\boldsymbol{\sigma}\right)\tag{58}$$

For the real solution $\tilde{\boldsymbol{\sigma}}$,

$$W_c\left(\tilde{\boldsymbol{\sigma}}\right)=\frac{1}{2V}\int_V\boldsymbol{\sigma}\cdot\boldsymbol{\varepsilon}dV=\frac{1}{2}\left\langle\tilde{\boldsymbol{\sigma}}\right\rangle_V\cdot\left\langle\tilde{\boldsymbol{\varepsilon}}\right\rangle_V=\frac{1}{2}\boldsymbol{\Sigma}:\mathbb{D}^{\hom}:\boldsymbol{\Sigma}\tag{59}$$

On the other hand,

$$W_c(\boldsymbol{\sigma}) = \frac{1}{2V}\int_V \boldsymbol{\sigma}\cdot\boldsymbol{\varepsilon} dV = \frac{1}{2}\langle\boldsymbol{\sigma}\rangle_V \cdot \langle\boldsymbol{\varepsilon}\rangle_V = \frac{1}{2}\boldsymbol{\Sigma} : \left(\sum_{r=1}^{n} f_r \mathbb{D}_r : \langle\boldsymbol{\sigma}\rangle_r\right) \qquad (60)$$

with $\langle\boldsymbol{\sigma}\rangle_r$ the average of local stain field in the phase r. We set that the localisation tensor of stress field $\mathbb{B} = \mathbb{I}$ for every point $\mathbf{x}$ in V, then we have $\langle\boldsymbol{\sigma}\rangle_r = \boldsymbol{\Sigma}$, it leads:

$$W_c(\boldsymbol{\sigma}) = \frac{1}{2}\boldsymbol{\Sigma} : \left(\sum_{r=1}^{n} f_r \mathbb{D}_r\right) : \boldsymbol{\Sigma} \qquad (61)$$

According to (58), we have:

$$\boldsymbol{\Sigma} : \mathbb{D}^{\text{hom}} : \boldsymbol{\Sigma} < \boldsymbol{\Sigma} : \left(\sum_{r=1}^{n} f_r \mathbb{D}_r\right) : \boldsymbol{\Sigma} \qquad (62)$$

Then the so-called Reuss bound (lower bound) is known as:

$$\mathbb{C}^{\text{hom}} > \left(\sum_{r=1}^{n} f_r \mathbb{C}_r^{-1}\right)^{-1} \qquad (63)$$

2.4.2.3 Hashin-Shtrikman variational procedure

Beside the homogenization schemes mentioned in the previous section, Hashin and Shtrikman introduced a variational procedure to estimate the effective modulus tensor of random, linear-elastic composites with statistically isotropic microstructures [Hashin and Shtrikman, 1962a]. The Hashin-Shtrikman variational principles consist in an alternative representation of the classical variational principles (such as those we apply for the Voigt bound and the Reuss bound) for heterogeneous linear-elastic medium in terms of suitably chosen polarization fields relative to a homogeneous reference material with modulus tensor $\mathbb{C}^{(0)}$. Making use of the Green's function for the elasticity problem associated with the linear homogeneous reference material, and using the hypothesis of statistical isotropy, Hashin and Shtrikman were able to obtain rigorous upper and lower bounds for the effective modulus tensor $\mathbb{C}^{\text{hom}}$ of the composites, by respectively choosing $\mathbb{C}^{(0)}$ to be equal to the "maximum" and "minimum" modulus tensors of the phases $\mathbb{C}^{(r)}$ [Hashin and Shtrikman, 1962a, 1963]. In keeping with the research sequence, the Hashin-Shtrikman variational principles will be presented first, and later specialized to estimate the effective modulus with Hashin-Shtrikman bounds.

2.4.2.3.1 Hashin-Shtrikman variational principles

For the linear elastic homogeneous material, from the minimum potential energy principle and the minimum complementary potential energy principle, the Voigt bound (upper bound) and the Reuss bound (lower bound) can be derived respectively. In order to narrow the gap between these two bounds mentioned above, and especially for the composites, we need new mathematical tools. One of powerful such tools is the celebrated Hashin-Shtrikman (HS) variational principle. The essence of the HS variational principles is that they are the variational principles specifically designed for composites, or heterogeneous medium. To measure the differences between homogeneous field and heterogeneous field, a homogeneous reference field is used to identify the heterogeneous fields.

First, consider a boundary value problem of the original composite (*r.v.e.*):

$$\left.\begin{aligned} \sigma_{ij,j} &= 0, \quad \text{for } \mathbf{x} \in V, \\ \sigma_{ij} &= C_{ijkl}(x)\varepsilon_{kl}, \quad \text{for } \mathbf{x} \in V, \\ W(\boldsymbol{\varepsilon}) &= \left\langle \frac{1}{2} C_{ijkl}\varepsilon_{ij}\varepsilon_{kl} \right\rangle_v, \quad \text{for } \mathbf{x} \in V, \\ u_i &= \bar{u}_i, \quad \text{for } \mathbf{x} \in \Gamma_u, \ (\Gamma_t = \emptyset, \ \Gamma_u = \partial V). \end{aligned}\right\} \tag{64}$$

Then, consider a homogeneous reference medium (a reference *r.v.e.*):

$$\left.\begin{aligned} \sigma^{(0)}_{ij,j} &= 0, \quad \text{for } \mathbf{x} \in V, \\ \sigma^{(0)}_{ij} &= C^{(0)}_{ijkl}(x)\varepsilon^{(0)}_{kl}, \quad \text{for } \mathbf{x} \in V, \\ W^{(0)}\left(\boldsymbol{\varepsilon}^{(0)}\right) &= \left\langle \frac{1}{2} C^{(0)}_{ijkl}\varepsilon^{(0)}_{ij}\varepsilon^{(0)}_{kl} \right\rangle_v, \quad \text{for } \mathbf{x} \in V, \\ u^{(0)}_i &= \bar{u}_i, \quad \text{for } \mathbf{x} \in \Gamma_u, \ (\Gamma_t = \emptyset, \ \Gamma_u = \partial V). \end{aligned}\right\} \tag{65}$$

To comparing the two *r.v.e.*s, we introduce the following decomposition in strain field and stress field:

$$u_i = u^{(0)}_i + u^d_i \tag{66}$$

$$\varepsilon_{ij} = \varepsilon^{(0)}_{ij} + \varepsilon^{(d)}_{ij} \tag{67}$$

and

$$\begin{aligned} \sigma_{ij} &= p_{ij} + C^{(0)}_{ijkl}\varepsilon_{kl} \\ &= p_{ij} + C^{(0)}_{ijkl}\left(\varepsilon^{(0)}_{kl} + \varepsilon^{d}_{kl}\right) \end{aligned} \tag{68}$$

where u_i^d is the disturbance displacement field and p_{ij} is called polarization stress that is defined by:

$$p_{ij} = \sigma_{ij} - C_{ijkl}^{(0)}\varepsilon_{kl} = \left(C_{ijkl} - C_{ijkl}^{(0)}\right)\varepsilon_{kl} \tag{69}$$

which indicates that the polarization stress is due to the heterogeneity of the composite.

Furthermore, since

$$u_i = \bar{u}_i, \ \forall \mathbf{x} \in \partial V \quad \text{and} \quad u_i^{(0)} = \bar{u}_i, \ \forall \mathbf{x} \in \partial V$$

it leads to a homogeneous boundary condition for the disturbance displacement field:

$$u_i^d = 0, \ \forall \mathbf{x} \in \partial V \tag{70}$$

We note that because $u_i^d = 0, \ \forall \mathbf{x} \in \partial V$, it can be readily to show that the average work done by the disturbance filed over any self-equilibrium stress field will be zero, that is

$$\int_V \sigma_{ij}\varepsilon_{ij}^d dV = \int_V \sigma_{ij}u_{i,j}^d dV \overset{Guass' \text{ theorem}}{=} \int_{\partial V} u_i^d n_j \sigma_{ij} dS + \int_V u_i^d \sigma_{ij,j} dV = 0 \tag{71}$$

From (68), the stress field can be divided into the homogeneous stress filed, $\sigma_{ij}^{(0)}$, and the inhomogeneous stress field:

$$\sigma_{ij} = \sigma_{ij}^{(0)} + t_{ij}, \quad \text{where} \ \ t_{ij} = p_{ij} + C_{ijkl}^{(0)}\varepsilon_{kl}^d \tag{72}$$

Note that $\sigma_{ij,j} = 0$ and $\sigma_{ij,j}^{(0)} = 0$, both homogeneous stress field $\sigma_{ij}^{(0)}$ and inhomogeneous stress field t_{ij} satisfy thus the equilibrium condition: $\sigma_{ij,j}^{(0)} = 0$, $t_{ij,j} = 0$. The latter is often called “the subsidiary condition”:

$$t_{ij,j} = p_{ij,j} + \left(C_{ijkl}^{(0)}\varepsilon_{kl}^d\right)_{,j} = 0 \tag{73}$$

We define:

$$\mathbf{U} = \left\{u_i \,\middle|\, u_i \in H(V), \ u_i = 0, \ \forall \mathbf{x} \in \partial V\right\}$$

$$\mathbf{S} = \left\{\sigma_{ij} \,\middle|\, \sigma_{ij} \in L(V)\right\}$$

Consider the following functional,

$$\Pi : \mathbf{S} \times \mathbf{U} \to \mathbb{R}$$

where

$$\begin{aligned}\Pi\left(p_{ij},\varepsilon_{ij}^{d}\right)&=\frac{1}{2}\int_{V}\sigma_{ij}\varepsilon_{ij}dV\\&=\frac{1}{2}\int_{V}\left(C_{ijkl}^{(0)}\varepsilon_{ij}^{(0)}\varepsilon_{kl}^{(0)}-\Delta C_{ijkl}^{-1}p_{ij}p_{kl}+p_{ij}\varepsilon_{ij}^{d}+2p_{ij}\varepsilon_{ij}^{(0)}\right)dV\end{aligned}\tag{74}$$

with $\Delta C_{ijkl}=C_{ijkl}-C_{ijkl}^{(0)}$, $p_{ij}=\Delta C_{ijkl}\varepsilon_{kl}$ and $\varepsilon_{ij}^{d}=\varepsilon_{ij}-\varepsilon_{ij}^{(0)}$.

On the basis of the expression (74), we have:

$$\begin{aligned}\Delta\Pi&=\Pi\left(p_{ij}+\delta p_{ij},\varepsilon_{ij}+\delta\varepsilon_{ij}\right)-\Pi\left(p_{ij},\varepsilon_{ij}\right)\\&=\frac{1}{2}\int_{V}\left(-2\Delta C_{ijkl}^{-1}p_{ij}\delta p_{kl}+p_{ij}\delta\varepsilon_{ij}^{d}+\delta p_{ij}\varepsilon_{ij}^{d}+2\delta p_{ij}\varepsilon_{ij}^{(0)}\right)dV\\&+\frac{1}{2}\int_{V}\left(-\Delta C_{ijkl}^{-1}\delta p_{ij}\delta p_{kl}+\delta p_{ij}\delta\varepsilon_{ij}^{d}\right)dV=\delta\Pi+\frac{1}{2!}\delta^{2}\Pi\end{aligned}$$

It can be proved [see Li, 2005] that the functional Π is stationary, i.e. $\delta\Pi=0$:

$$\delta\Pi=\frac{1}{2}\int_{V}\left(-2\Delta C_{ijkl}^{-1}p_{ij}\delta p_{kl}+p_{ij}\delta\varepsilon_{ij}^{d}+\delta p_{ij}\varepsilon_{ij}^{d}+2\delta p_{ij}\varepsilon_{ij}^{(0)}\right)dV=0\tag{75}$$

if the subsidiary condition (45) is satisfied, i.e. $t_{ij,j}=0$.

And then $\Delta\Pi=\delta^{2}\Pi$, we have the Hashin-Shtrikman variational principles:

if $\Delta\mathbb{C}>0$, $\Delta\Pi=\delta^{2}\Pi<0$, Π achieves a maximum value,

if $\Delta\mathbb{C}<0$, $\Delta\Pi=\delta^{2}\Pi>0$, Π achieves a minimum value.

Note that:

$$\begin{aligned}\Pi\left(p_{ij},\varepsilon_{ij}^{d}\right)&=\frac{1}{2}\int_{V}\sigma_{ij}\varepsilon_{ij}dV=W\left(\boldsymbol{\varepsilon}\right)V\\&=\frac{1}{2}\int_{V}\left(C_{ijkl}^{(0)}\varepsilon_{ij}^{(0)}\varepsilon_{kl}^{(0)}-\Delta C_{ijkl}^{-1}p_{ij}p_{kl}+p_{ij}\varepsilon_{ij}^{d}+2p_{ij}\varepsilon_{ij}^{(0)}\right)dV\\&=W^{(0)}\left(\boldsymbol{\varepsilon}^{(0)}\right)V+W^{\pi}\left(\mathbf{p},\boldsymbol{\varepsilon}^{d}\right)V\end{aligned}$$

where $W^{\pi}\left(\mathbf{p},\boldsymbol{\varepsilon}^{d}\right):=\frac{1}{2V}\int_{V}\left(-\Delta C_{ijkl}^{-1}p_{ij}p_{kl}+p_{ij}\varepsilon_{ij}^{d}+2p_{ij}\varepsilon_{ij}^{(0)}\right)dV$. If $\Delta\mathbb{C}<0$,

$W^{\pi}\left(\mathbf{p},\boldsymbol{\varepsilon}^{d}\right):=\underline{W}^{\pi}\left(\mathbf{p},\boldsymbol{\varepsilon}^{d}\right)$; whereas if $\Delta\mathbb{C}>0$, $W^{\pi}\left(\mathbf{p},\boldsymbol{\varepsilon}^{d}\right):=\overline{W}^{\pi}\left(\mathbf{p},\boldsymbol{\varepsilon}^{d}\right)$.

Therefore the Hashin-Strikman variational principles provide the following bound:

$$\underline{W}^{\pi}\left(\mathbf{p},\boldsymbol{\varepsilon}^{d}\right)+W^{(0)}\left(\boldsymbol{\varepsilon}^{(0)}\right)\leq W\left(\boldsymbol{\varepsilon}\right)\leq\overline{W}^{\pi}\left(\mathbf{p},\boldsymbol{\varepsilon}^{d}\right)+W^{(0)}\left(\boldsymbol{\varepsilon}^{(0)}\right)\tag{76}$$

2.4.2.3.2 Bound for the effective properties

In this section, we will derive the bounds for the macroscopic compression and shear modules from the expression (76).

Consider prescribed macro strain boundary condition for both the composite and the reference medium:

$$\mathbf{u} = \mathbf{x} \cdot \mathbf{E}, \quad \forall \mathbf{x} \in \partial V \quad \left(\Gamma_t = \emptyset\right)$$

$$\mathbf{u}^0 = \mathbf{x} \cdot \mathbf{E}, \quad \forall \mathbf{x} \in \partial V \quad \left(\Gamma_t = \emptyset\right)$$

where $\mathbf{E}$ is the macroscopic strain of the *r.v.e.*, given by the averaging theorem $\mathbf{E} = \langle \boldsymbol{\varepsilon} \rangle_V$.

The minimum potential energy principle reads as:

$$W(\mathbf{E}) = \inf_{\langle \boldsymbol{\varepsilon} \rangle = \mathbf{E}} W(\boldsymbol{\varepsilon}) \tag{77}$$

Under such condition, the Hashin-Strikman variational principles are rewritten as:

$$\underline{I} \le \inf_{\langle \boldsymbol{\varepsilon} \rangle = \mathbf{E}} W(\boldsymbol{\varepsilon}) \le \overline{I} \tag{78}$$

where

$$\underline{I}\left(\text{or } \overline{I}\right) = W^{(0)}\left(\boldsymbol{\varepsilon}^{(0)}\right) + \frac{1}{2V}\int_V \left(-\Delta C^{-1}_{ijkl} p_{ij} p_{kl} + p_{ij}\varepsilon^d_{ij} + 2 p_{ij}\varepsilon^{(0)}_{ij}\right) dV \tag{79}$$

Assume that there are N-phases in the composite (including the matrix). In each phase (inclusion), the elastic tensor as well as stress polarization tensor is constant,

$$\mathbb{C}(x) = \sum_{r=1}^{N} \mathbb{C}^r H(\Omega_r) \tag{80}$$

$$\mathbf{p}(x) = \sum_{r=1}^{N} \mathbf{p}^r H(\Omega_r) \tag{81}$$

where Ω_r is the domain of each phase and $H(\bullet)$ is the Heaviside function defined by:

$$H(\Omega_r) = \begin{cases} 1, & \forall \mathbf{x} \in \Omega_r \\ 0, & \forall \mathbf{x} \notin \Omega_r \end{cases} \tag{82}$$

We now calculate each term in (78)

1)

$$\begin{aligned} \inf_{\langle \boldsymbol{\varepsilon} \rangle = \mathbf{E}} W(\boldsymbol{\varepsilon}) &= \frac{1}{2V}\int_V \boldsymbol{\sigma} : \boldsymbol{\varepsilon} dV = \frac{1}{2}\langle \boldsymbol{\sigma} \rangle : \langle \boldsymbol{\varepsilon} \rangle \\ &= \frac{1}{2}\langle \boldsymbol{\varepsilon} \rangle : \mathbb{C}^{\text{hom}} : \langle \boldsymbol{\varepsilon} \rangle = \frac{1}{2}\mathbf{E} : \mathbb{C}^{\text{hom}} : \mathbf{E} \end{aligned} \tag{83}$$

2)

$$W^{(0)}\left(\boldsymbol{\varepsilon}^{(0)}\right)=\frac{1}{2V}\int_V \boldsymbol{\sigma}^{(0)}:\boldsymbol{\varepsilon}^{(0)}dV=\frac{1}{2}\left\langle\boldsymbol{\sigma}^{(0)}\right\rangle:\left\langle\varepsilon^{(0)}\right\rangle$$
$$=\frac{1}{2}\left\langle\boldsymbol{\varepsilon}^{(0)}\right\rangle:\mathbb{C}^{(0)}:\left\langle\boldsymbol{\varepsilon}^{(0)}\right\rangle=\frac{1}{2}\mathbf{E}:\mathbb{C}^{(0)}:\mathbf{E} \tag{84}$$

3)

$$\frac{1}{2V}\int_V \mathbf{p}^r:\Delta\mathbb{C}^{-1}:\mathbf{p}^r dV=\frac{1}{2}\sum_{r=1}^{N}\frac{1}{V}\int_{\Omega_r}\mathbf{p}^r:\Delta\mathbb{C}_r^{-1}:\mathbf{p}^r dV$$
$$=\frac{1}{2}\sum_{r=1}^{N} f_r\mathbf{p}^r:\Delta\mathbb{C}_r^{-1}:\mathbf{p}^r \tag{85}$$

4)

$$\frac{1}{V}\int_V \mathbf{p}:\boldsymbol{\varepsilon}^{(0)}dV=\left(\frac{1}{V}\int_V \mathbf{p}dV\right):\mathbf{E}=\langle\mathbf{p}\rangle:\mathbf{E}=\sum_{r=1}^{N} f_r\mathbf{p}_r:\mathbf{E} \tag{86}$$

5) The last undetermined term is $(1/2V)\int_V \mathbf{p}:\boldsymbol{\varepsilon}^d dV$. Considering the subsidiary condition $p_{ij,j}+C_{ijkl}^{(0)}u_{k,lj}^d=0$, and solving u_k^d in term of p_{ij} by using Green's function method [see Li, 2005], we can obtain:

$$\frac{1}{2V}\int_V \mathbf{p}:\boldsymbol{\varepsilon}^d dV=-\frac{1}{2}\sum_{r=1}^{N} f_r\mathbf{p}_r:\mathbb{P}^0:\left(\mathbf{p}_r-\langle\mathbf{p}_r\rangle\right) \tag{87}$$

Where $\mathbb{P}^0$ is the Hill tensor defined by expression (13), the superscript 0 denotes the reference medium.

With the expressions (83)-(87), the inequality (78) can be transformed into the bound on elastic tensor. For simplicity, we only illustrate here Hashin-Shtrikman bound for a two-phase composite ($k^{(2)}>k^{(1)}$ and $\mu^{(2)}>\mu^{(1)}$) with spherical inclusion and isotropic reference medium.

Therefore the Hill tensor $\mathbb{P}^0$ can be described by expression (14):

$$\mathbb{P}^0=\frac{1}{3k^0+4\mu^0}\mathbb{J}+\frac{3\left(k^0+2\mu^0\right)}{5\mu^0\left(3k^0+4\mu^0\right)}\mathbb{K}$$

And combining the stationary conditions: $\partial\overline{I}/\partial\mathbf{p}=0$ and $\partial\underline{I}/\partial\mathbf{p}=0$, for the special case of two-phase composites with well-ordered (i.e., when $(\mu^{(1)}-\mu^{(2)})\cdot$

$(k^{(1)} - k^{(2)}) > 0$), isotropic phases and statistically isotropic microstructures, the Hashin-Shtrikman bounds may be written in the form [Ponte Castañeda, 2004]:

$$k_{HS}^{\hom} = f^{(1)}k^{(1)} + f^{(2)}k^{(2)} - \frac{f^{(1)}f^{(2)}\left(k^{(1)} - k^{(2)}\right)^2}{f^{(2)}k^{(1)} + f^{(1)}k^{(2)} + 4\mu^{(0)}/3} \tag{88}$$

$$\mu_{HS}^{\hom} = f^{(1)}\mu^{(1)} + f^{(2)}\mu^{(2)} - \frac{f^{(1)}f^{(2)}\left(\mu^{(1)} - \mu^{(2)}\right)^2}{f^{(2)}\mu^{(1)} + f^{(1)}\mu^{(2)} + \mu^{(0)}\left(9k^{(0)} + 8\mu^{(0)}\right)/\left[6\left(k^{(0)} + 2\mu^{(0)}\right)\right]} \tag{89}$$

where setting $k^{(0)}$ and $\mu^{(0)}$ equal to $k^{(2)}$ and $\mu^{(2)}$ yield upper bounds for $k_{HS}^{\hom}$ and $\mu_{HS}^{\hom}$, respectively, while setting $k^{(0)}$ and $\mu^{(0)}$ equal to $k^{(1)}$ and $\mu^{(1)}$ yield lower bounds for $k_{HS}^{\hom}$ and $\mu_{HS}^{\hom}$, respectively. Interestingly, the lower bounds for $k_{HS}^{\hom}$ and $\mu_{HS}^{\hom}$ are exactly the same as the $k^{\hom}$ and $\mu^{\hom}$ from Mori-Tanaka method given by (27) and (28).

2.5 Hill's incremental approach

Hill's incremental approach is one of the most commonly used approaches of nonlinear homogenization methods for nonlinear heterogeneous materials. The incremental method is easy to implement in standard computer codes and it is particularly suitable for complex loading paths with unloading cycles. In order to estimate the macroscopic response of the Callovo-Oxfordien argillite, based on Hill's incremental approach, Abou-Chakra Guéry [Abou-Chakra Guéry et al., 2008] proposed a three phase composite model and Jiang [Jiang et al., 2009] proposed a two phase micromechanical model, both the two models have an overall good agreement with experimental data after a suitable "isotropization procedure". These proposed micromechanical models in view of Hill's incremental approach are thus considered being able to describe the main features of mechanical behaviors observed in laboratory tests, such as pressure dependency, transition from volumetric compressibility to dilatancy, plastic damage coupling, progressive degradation of elastic properties and material softening due to damage by microcracks.

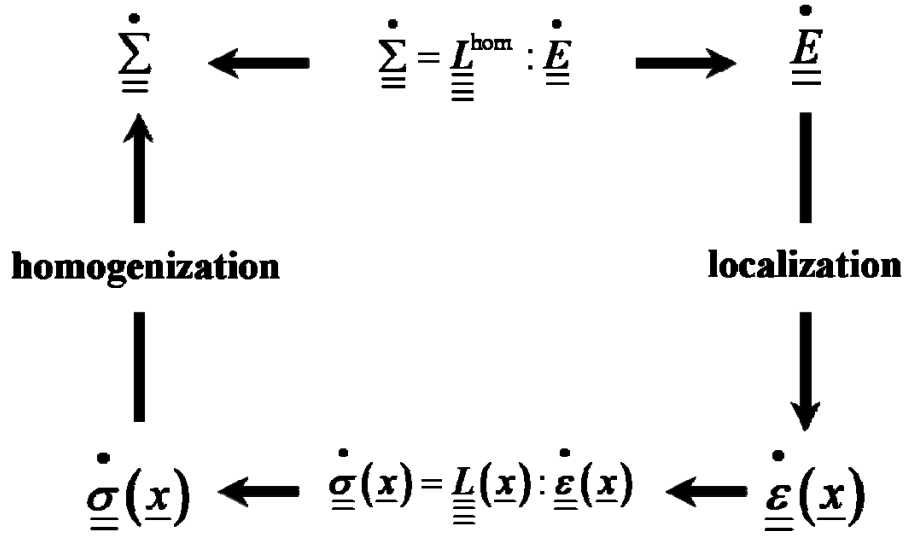

Fig.3. Diagram of non linear homogenization method with incremental approach

The main steps of nonlinear homogenization method in incremental form for micromechanical modeling of heterogeneous materials are illustrated in Fig.3. The incremental method is proposed by Rodney Hill [Hill, 1965] to linearize the nonlinear homogenization problem in an incremental way and then based on estimates from the linear homogenization for resolving this linearized problem. It consists in the determination of the overall tangent stiffness tensor $\mathbb{L}^{\text{hom}}$ for each incremental loading step, in the term of the local constitutive behaviors.

This method thus requires a rate formulation of the local constitutive relations for each phase:

$$\dot{\boldsymbol{\sigma}}(\mathbf{x}) = \mathbb{L}(\mathbf{x}) : \dot{\boldsymbol{\varepsilon}}(\mathbf{x}) \tag{90}$$

It should be noted that the linearized law (90) is characterized by non-linear tangent modulus. As for linear elastic materials we mentioned, at each iteration step, to make use of a localization tensor: the difference with the linear case is found essentially in the nature of the module considered. The rate of macroscopic strain is linked to the rate of local stain by:

$$\dot{\boldsymbol{\varepsilon}}(\mathbf{x}) = \mathbb{A}(\mathbf{x}) : \dot{\mathbf{E}} \tag{91}$$

$\mathbb{A}(\mathbf{x})$ denotes the localization tensor in the linear comparison material resulting from the linearization procedure.

It follows that the macroscopic constitutive law is written:

$$\dot{\boldsymbol{\Sigma}} = \mathbb{L}^{\text{hom}} : \dot{\mathbf{E}} \tag{92}$$

with effective tangent modulus:

$$\mathbb{L}^{\text{hom}} = \langle \mathbb{L} : \mathbb{A} \rangle \tag{93}$$

Hypotheses

The Hill's incremental method implies the following approximation:

At any point $\mathbf{x}$ of a phase (r), the relationship linking the rate of deformation in strain rate can be approximated by:

$$\forall \mathbf{x} \in (r), \quad \dot{\boldsymbol{\sigma}}(\mathbf{x}) = \mathbb{L}_r : \dot{\boldsymbol{\varepsilon}}(\mathbf{x}) \tag{94}$$

The solution of the Eshelby problem without initial stain is applied to each increment of loading, by adopting a uniform tangent operator $\mathbb{L}_r$ for each phase. This is rather a rough approximation because in reality the field of plastic strain around and in the inclusion in many cases can be significantly heterogeneous.

In accordance with above approximations, the incremental relationship of stain locationzation is simplified as:

$$\dot{\overline{\boldsymbol{\varepsilon}}}_r = \mathbb{A}_r : \dot{\mathbf{E}} \tag{95}$$

where $\overline{\boldsymbol{\varepsilon}}_r$ is the average value of local stain field in phase r and $\mathbb{A}_r$ is the uniform localization tensor for each phase.

It was recognized early on that Hill's approach always leads to a too stiff response which would cause the accumulation of errors at each iteration step caused by the failure to adequately take account of the heterogeneity of the stain field in the phases.

Many works in the context of the plasticity of two-phase metal (matrix von Mises) indicate that it is possible to make supple the predictions of the incremental method by considering an Eshelby tensor evaluated from an isotropic approximation of the tangent operator of the matrix. Some predictions that seem quite convincing were obtained by [Kanoute and Chaboche, 2005] and [Doghri and Ouaar, 2003] including in laws with nonlinear kinematic hardening. In view of these results, it appears that despite the defect mentioned above, the incremental approach, via the implementation of an isotropization procedure, provides the possibilities for the study of dissipative behavior of structural materials.

2.6 Conclusion

We have presented in this chapter three different schemes of estimation and three different variational bounds in the linear context. These provide the basis for the study of nonlinear behavior of composites. For linearizing the local behavior, we can mention incremental approach, tangent or secant formulations or second order estimates. The Hill's incremental approach is one of the most commonly used approaches of nonlinear homogenization methods for nonlinear heterogeneous materials, it will employed in chapter 3 and chapter 4. However, in view of its failure to adequately take account of the heterogeneity of the stain field in the phases, in chapter 5, we will introduce a variational method based on incremental variational principles for the mechanical behavior of geomaterial.

Chapter 3
A micromechanical analysis of time-dependent behavior based on subcritical damage in claystones

Résumé du chapitre

Pour la caractérisation du comportement différée de l'argilite, deux mécanismes de fluage sont envisagés: la déformation viscoplastique de la matrice argileuse et la propagation subcritique de microfissures. Dans ce chapitre, l'accent est mis sur le deuxième mécanisme. L'argilite du Callovo-Oxfordien est considéré comme un matériau composite à trois phases: matrice argileuse élastique endommageable, deux types d'inclusions minérales élastiques, grains de quartz et grains de calcite. Un modèle mésomécanique est proposé pour décrire les déformations différées des argilites dues à l'endommagement différé de la matrice argileuse. Le modèle est basé sur des méthodes d'homogénéisation linéaires des matériaux hétérogènes.

Un modèle d'endommagement différé est utilisé pour la matrice argileuse. En vue de la forte dissymétrie entre les réponses sous contraintes de traction et de compression pour la roche argileuse, la loi d'endommagement isotrope adoptée dans ce chapitre permet de prendre en compte la différence de cinétique de l'endommagement sous la sollicitation de traction et de compression. L'évolution de l'endommagement spécifiquement développée pour décrire la propagation subcritique de microfissures est définie à partir des données expérimentales.

Une fois les lois de comportement locales explicitées, on se propose d'appliquer trois schémas d'homogénéisation linéaires (borne de Voigt [Voigt, 1889], schéma dilué [Eshelby, 1957] et modèle de Mori-Tanaka [Mori et Tanaka, 1973]) à l'argilite du Callovo-Oxfordien. On compare ensuit les résultats issus des trois schémas d'homogénéisation. Dans ce stade, l'objectif visé est double: i) montrer l'impact de la microstructure de l'argilite sur ses propriétés élastiques macroscopiques; ii) construire un modèle macroscopique à partir d'un schéma d'homogénéisation et puis tester la capacité prédictive de ce modèle.

Le chapitre se termine par une validation par comparaison avec deux essais de fluage uniaxiale.

A micromechanical analysis of time-dependent behavior based on subcritical damage in claystones

Abstract:

In this paper, a micromechanical model is proposed for time-dependent strain in claystones. The representative volume element (RVE) of claystone is characterized by a three-phase composite. Quartz and calcite grains are embedded inside clay matrix. The time-dependent strain is related to subcritical propagation of microcracks inside the clay matrix. A two-step homogenization procedure is proposed. A micromechanics-based isotropic damage model is first formulated for the subcritical growth of microcracks inside the clay matrix. Different homogenization schemes are considered by taking into account opening and closure of microcracks. Two driving forces are used respectively for the subcritical evolution of damage under tensile and compressive stresses. Then the macroscopic properties of the claystone are determined by a second-level homogenization procedure using three different schemes. The numerical algorithm for numerical implementation of the proposed model in standard finite element code is proposed. Numerical evaluations of the proposed model are performed through simulations of creep tests under different loading paths and using different homogenization schemes. Finally, comparisons between numerical results and experimental data are presented.

Keywords: Damage, creep, claystone, subcritical damage, micromechanics, homogenization

3.1 Introduction

Claystones are extensively investigated in Europe as a potential geological barrier in the framework of research projects devoted to underground repository of nuclear waste. Under the coordination of the French Agency for radioactive waste management (ANDRA), laboratory tests and numerical modeling have been performed for the characterization of thermo-hydromechanical properties of such rocks. In situ experiments have also been realized in the underground research laboratory of ANDRA in Bure in the North-East of France. The geological layer of claystones, called claystones, investigated in that context is located at a depth of 445m to 490m (Lebon and Mouroux, 1999). According to microstructural analyses (Chiarelli et al., 2003; Robinet, 2008), the claystones mainly contains 45% of clay minerals, 28% of calcite, 23 % of quartz and less than 5 % of other minerals

(feldspars, pyrite etc.). For the purpose of characterization of thermo-hydromechanical properties, two basic material scales should be taken into account (Abou-Chakra et al., 2008, Robinet, 2008, Shen et al., 2012). At the mesoscopic scale, the claystones can be seen as a three-phase composite constituted by a clay matrix in which are embedded calcite and quartz grains. At the microscopic scale, the clay matrix is a porous material composed by a solid phase containing a distribution of pores between clay particles. The porosity of the claystones is about 15 % and the pore size varies between 20 nm and 50 nm. Due to the very long life of radioactive waste, the characterization of long term hydromechanical behaviors of claystones is a crucial issue. For this purpose, laboratory creep tests associated with microstructural analysis have been performed on claystones with different degrees of saturation. It is found that two main mechanisms are at the origin of macroscopic time dependent deformation. The first one is related to viscoplastic flow of clay matrix and the second one is due to subcritical propagation of microcracks in clay matrix (Zhu et al., 2008; Abou-Chakra et al., 2009; Bornert et al., 2010). Indeed, various microscopic observations have revealed the existence of different propagation modes of microcracks inside the claystone under mechanical loading and moisture variation (Robinet, 2008; Bornert, 2010; Yang et al. 2012). On the other hand, based on experimental data, macroscopic and micromechanical formulations have been proposed for the description of viscoplastic deformation in the claystones (Chau and Wong, 1997; Zhou et al., 2008, Abou-Chakra, 2009) just to mention a few. Different constitutive models have also been proposed for damage and plastic damage coupling in quasi-brittle materials such as rocks and concrete (Ju, 1989, 2012; Haml and Dragon, 1996; Hayakawa and Murakami; Voyiadjis et al., 2008; Comi and Perego, 2011). Constitutive models taking into account the evolution of rock microstructure such as microcrack and bedding planes have also been developed (Chan et al., 1997; Shao et al., 2003; Pietruszczak et al., 2004; Zhu et al. 2008). However, most damage models are devoted to time-independent behaviors of materials. Time-dependent strains are classically described by viscoplastic models. In some cases such as subcritical growth of microcracks, the physical background of viscoplastic models is not properly established. In the present work, we present a micromechanical analysis for time-dependent deformation related to subcritical growth of damage in claystones. For this purpose, the claystones are considered as a three phase composite, namely composed of a clay matrix and two families of mineral inclusions: calcite and quartz grains. The clay matrix exhibits a time-dependent subcritical evolution of microcracks while a linear elastic behavior is used for calcite and quartz grains. Based on the reference Eshelby's solution for the inclusion problem, the macroscopic behavior of

equivalent homogeneous medium is found from a linear homogenization technique. Influences of homogenization schemes on the macroscopic responses are discussed. Comparisons between theoretical predictions and experimental data are also presented.

3.2 Local damage model for clay matrix

The local mechanical behavior of the clay matrix is described by a time-dependent damage model. It is assumed that the material damage is generated by a random distribution of microcracks which evolve in time due to subcritical propagation of microcracks. The physical mechanism of subcritical crack growth is complex. In most geomaterials, the stress corrosion is widely considered as one of essential phenomena (Anderson and Grew, 1977; Atkinson, 1984; Nara and Kaneko, 2005, 2006). The sub-critical crack growth is generally influenced by environmental conditions such as temperature, water content and interstitial fluid chemistry (Henry et al., 1977; Waza et al., 1980; Atkinson, 1984). In the present work, for the sake of simplicity, the sub-critical crack growth is described by an isotropic damage model. Therefore, the distribution of microcracks is represented by a scalar internal damage variable which is related to the density of microcracks $\propto Na^3/\Omega$, as defined by Budiansky and O'Connell (1978), N being the number of microcracks, a the average radius of microcracks and Ω the volume of representative volume element (RVE). However, it is known that the mechanical behavior of geomaterials depends on loading path. For instance, there is a strong dissymmetry between the responses under tensile and compression stresses respectively. This dissymmetry is directly related to the state of opening of microfissure. Under a tensile stress, the microcracks are open and their propagation is generally unstable in nature. Under compression, the microcracks are mostly closed and their propagation is associated with the frictional sliding along the crack surfaces. The kinetics of damage evolution is also different between compressive and tensile loading. Moreover, the mechanical behaviors of the damaged materials are different depending on whether the microcracks are open or closed. It involves unilateral effects that must be taken into account in modeling. Inspired by previous works on damage modeling of geomaterials (Mazars, 1986; Chen et al., 2010), two scalar internal variables d_t, d_c are introduced to describe the state of damage in tension and compression respectively. In order to determine the effective mechanical properties of damaged material, we assume the existence of a thermodynamic potential, for instance represented by the free energy function. Assuming a linear response for a fixed damage state, the free energy function is

written in the following quadratic form (Chaboche, 1981; Lemaitre, 1984):

$$W\left(\boldsymbol{\varepsilon}, d_t, d_c\right) = \frac{1}{2}\boldsymbol{\varepsilon} : \mathbb{C}\left(d_t, d_c\right) : \boldsymbol{\varepsilon} \tag{1}$$

$\boldsymbol{\varepsilon}$ is the local the strain tensor of clay matrix, $\mathbb{C}\left(d_t, d_c\right)$ the elastic stiffness tensor of damaged clay matrix. The elastic constitutive relation is then deduced as:

$$\boldsymbol{\sigma} = \frac{\partial W}{\partial \boldsymbol{\varepsilon}} = \mathbb{C}\left(d_t, d_c\right) : \boldsymbol{\varepsilon} \tag{2}$$

As an isotropic material is concerned, the elastic stiffness tensor is expressed by:

$$\mathbb{C}\left(d_t, d_c\right) = 3k\left(d_t, d_c\right)\mathbb{J} + 2\mu\left(d_t, d_c\right)\mathbb{K} \tag{3}$$

$k\left(d_t, d_c\right)$ and $\mu\left(d_t, d_c\right)$ are respectively the bulk modulus and shear modulus of damaged clay matrix. Two forth order symmetric tensors, $\mathbb{J}$ and $\mathbb{K}$, are the spherical and deviatoric operators respectively defined by :

$$\mathbb{J} = \frac{1}{3}\boldsymbol{\delta} \otimes \boldsymbol{\delta}\ ,\ \mathbb{I} = \frac{1}{2}\left(\boldsymbol{\delta} \underline{\otimes} \boldsymbol{\delta} + \boldsymbol{\delta} \overline{\otimes} \boldsymbol{\delta}\right)\ ,\ \mathbb{K} = \mathbb{I} - \mathbb{J} \tag{4}$$

$\boldsymbol{\delta}$ is the second order unit tensor. The thermodynamic forces associated with two damage variables can also be deduced:

$$Y_t = -\frac{\partial W}{\partial d_t} = -\frac{1}{2}\boldsymbol{\varepsilon} : \frac{\partial \mathbb{C}\left(d_t, d_c\right)}{\partial d_t} : \boldsymbol{\varepsilon}\ ,\quad Y_c = -\frac{\partial W}{\partial d_c} = -\frac{1}{2}\boldsymbol{\varepsilon} : \frac{\partial \mathbb{C}\left(d_t, d_c\right)}{\partial d_c} : \boldsymbol{\varepsilon} \tag{5}$$

The mechanical dissipation related to the evolution of damage must satisfy the following fundamental inequality:

$$Y_t \dot{d}_t + Y_c \dot{d}_c \geq 0 \tag{6}$$

It is now necessary to determine the effective elastic properties of the damaged material. To this end, an overall damage coefficient is defined to represent the effect of microcracks on the elastic properties of the material. A linear combination of the two damage variables is here used:

$$d = \alpha_t d_t + \left(1 - \alpha_t\right) d_c \tag{7}$$

The coefficient α_t determines the relative importance of the damage respectively induced by the tensile and compression stresses and therefore it depends on the loading path. Based on previous works related to this feature (Mazars 1986; Chen et

al. 2011), we propose to use the following simple expression for the loading coefficient:

$$\alpha_t = \frac{\left\|\boldsymbol{\sigma}^+\right\|}{\left\|\boldsymbol{\sigma}\right\|} \quad , \quad \boldsymbol{\sigma}^+ = \sum_{i=1}^{3} \left\langle \sigma_i \right\rangle \vec{V}^i \otimes \vec{V}^i \tag{8}$$

σ_i denotes three principal stresses and $\vec{V}^i$ the corresponding principal eigen vectors. The operator $\langle x \rangle$ defines $\langle x \rangle = (|x| + x)/2$. We easily find that the loading coefficient varies between $\alpha_t = 1$ for the uniaxial tension to $\alpha_t = 0$ for the uniaxial compression.

As an isotropic material is here concerned, the effect of induced damage on the elastic properties is reflected by the degradation of the two elastic moduli, which evolve as functions of the two damage variables d_t and d_c. In order to establish the relations between elastic moduli and damage variables, some relevant results from the micromechanical analysis are used here. Consider an isotropic linear elastic solid, characterized by the bulk and shear modulus $\tilde{k}_0$ and $\tilde{\mu}_0$, containing a family of randomly distributed microcracks. The effective elastic properties of the cracked material can be evaluated using the linear homogenization technique based on the fundamental solution of Eshelby (1957) for the inclusion problem (Zaoui et al., 2000; Zhu et al., 2008). The effective elastic moduli depend on the homogenization scheme used and the opening state of microcracks. In this work, two widely used schemes are considered: dilute scheme and Ponte-Castaneda and Willis (PCW) scheme (Ponte-Castaneda and Willis, 1995). The corresponding expressions of effective elastic moduli given below for both open and closed cracks.

Dilute scheme for open crack:

$$\frac{k(d)}{\tilde{k}_0} = 1 - \frac{16}{9}\frac{\left(1-\tilde{\nu}_0^2\right)}{\left(1-2\tilde{\nu}_0\right)}d, \quad \frac{\mu(d)}{\tilde{\mu}_0} = 1 - \frac{32}{15}\frac{\theta\left(1-\tilde{\nu}_0\right)}{\left(2-\tilde{\nu}_0\right)}d, \ \theta = \frac{5-\tilde{\nu}_0}{3} \tag{9}$$

Dilute scheme for closed crack:

$$\frac{k(d)}{\tilde{k}_0} = 1, \quad \frac{\mu(d)}{\tilde{\mu}_0} = 1 - \frac{32}{15}\frac{\left(1-\tilde{\nu}_0\right)}{\left(2-\tilde{\nu}_0\right)}d \tag{10}$$

PCW scheme for open crack:

$$\frac{k(d)}{\tilde{k}_0}=1-\frac{16\left(1-\tilde{\nu}_0^2\right)d}{9\left(1-2\tilde{\nu}_0\right)+\frac{16d}{9}\left(1+\tilde{\nu}_0\right)^2},$$
$$\frac{\mu(d)}{\tilde{\mu}_0}=1-\frac{480d\left(1-\tilde{\nu}_0\right)\theta}{225\left(2-\tilde{\nu}_0\right)+64d(4-5\tilde{\nu}_0)\theta},\ \theta=\frac{5-\tilde{\nu}_0}{3} \tag{11}$$

PCW scheme for closed crack:

$$\frac{k(d)}{\tilde{k}_0}=1,\quad \frac{\mu(d)}{\tilde{\mu}_0}=1-\frac{480d\left(1-\tilde{\nu}_0\right)}{225\left(2-\tilde{\nu}_0\right)+64d(4-5\tilde{\nu}_0)} \tag{12}$$

$\tilde{\nu}_0$ is Poisson's ratio of the undamaged material.

From these results obtained, it is found that two elastic moduli are affected by the induced damage in an independent way. Practically, this means that both the elastic modulus and Poisson's ratio are affected by the damage and with a different proportion. This is clearly different with a number of macroscopic damage models (Marigo, 1985; Mazars, 1986; Lemaitre, 1984), in which only Young's modulus is affected by damage while Poisson ratio remains unchanged.

2.1 Subcritical damage evolution

In the present work, the time-dependent subcritical damage evolution is considered. In order to determine the damage evolution rate, it is needed to define a subcritical damage criterion and a damage evolution law for both tensile and compressive stresses. Classically, the damage criterion is a scalar-valued function of the thermodynamic forces associated with the damage variables, as those defined in (5). However, to facilitate experimental identification and more explicitly interpret some physical phenomena in geomaterials, it is generally proposed to adopt a more physical approach while remaining consistent with the fundamental inequality of the mechanical dissipation (6). For example, it is known that the tensile damage is directly related to tensile strains leading to opening of microcracks while the compressive damage is generally related to frictional sliding along closed microcracks surfaces. Therefore, introduce two driving forces which are responsible for the damage evolution in tension and compression respectively. Inspired by previous works, the following damage driving forces are proposed:

$$F_t = \max\left(F_{t0}, \varepsilon_{eq}^t\right), \quad \varepsilon_{eq}^t = \sqrt{\sum_{i=1}^{3}\left\langle \varepsilon_i \right\rangle^2}$$
$$F_c = \max\left(F_{c0}, \varepsilon_{eq}^c\right), \quad \varepsilon_{eq}^c = \sqrt{\frac{1}{2}e_{ij}e_{ij}}, \ e_{ij} = \varepsilon_{ij} - \frac{1}{3}\varepsilon_{kk}\delta_{ij} \tag{13}$$

F_{t0} and F_{c0} denote the initial damage threshold for tensile and compressive damage respectively. Using these driving forces, the damage criteria are expressed in the following exponential forms:

$$f_t = \left(1 - \frac{1}{\exp\left[B_t\left(F_t - F_{t0}\right)\right]}\right) - d_t \tag{14}$$

$$f_c = \left(1 - \frac{1}{\exp\left[B_c\left(F_c - F_{c0}\right)\right]}\right) - d_c \tag{15}$$

The parameters B_t and B_c control the kinetics of damage evolution in tension and compression, respectively. Based on the classical power law used for subcritical propagation of cracks, the following damage evolution laws are proposed:

$$\dot{d}_t = \xi_t\left(\frac{f_t + |f_t|}{2}\right)^{n^t} \tag{16}$$

$$\dot{d}_c = \xi_c\left(\frac{f_c + |f_c|}{2}\right)^{n^c} \tag{17}$$

The parameters n^t and n^c control the evolution of subcritical damage rate while ξ_t and ξ_c define the initial slopes of damage evolution curves versus time. These parameters may be identified from creep or relaxation tests.

3.3 Macroscopic behaviour of claystone

After the formulation of local damage model for the clay matrix, the macroscopic behavior of the claystone is now investigated. As mentioned above, the claystone is seen as a three-phase composite constituted by the clay matrix, quartz and calcite grains. The clay matrix is described by the isotropic damage model presented above and characterized by two current elastic moduli, $k(d)$ and $\mu(d)$, determined by either dilute and PCW schemes. A linear elastic behavior is assumed for both quartz and

calcite, respectively characterized by the constant moduli k_1 and μ_1 for quartz and k_1 and μ_1 for calcite. For a given state of damage in the clay matrix, the macroscopic free energy of the claystone can be expressed in the following relation:

$$W^{\hom}(\mathbf{E},d)=\frac{1}{2}\mathbf{E}:\mathbb{C}^{\hom}(d):\mathbf{E} \tag{18}$$

$\mathbf{E}$ is the macroscopic strain tensor and $\mathbb{C}^{\hom}(d)$ denotes the macroscopic elastic stiffness tensor taking into account the induced damage inside the clay matrix. In a general way, the macroscopic elastic stiffness tensor is determined by volumetric averaging procedure on the RVE, that is:

$$\mathbb{C}^{\hom}(d)=\left\langle \mathbb{C}^{r}(d):\mathbb{A}^{r}\right\rangle,\ \ \boldsymbol{\varepsilon}^{r}=\mathbb{A}^{r}:\mathbf{E} \tag{19}$$

The fourth order concentration tensor $\mathbb{A}^{i}$ relates the local strain tensor $\boldsymbol{\varepsilon}^{r}$ of the r^{th} constituent phase to the uniform macroscopic strain $\mathbf{E}$, applied to the boundary of the RVE. Accordingly, the effective elastic relation of the claystone is given by:

$$\boldsymbol{\Sigma}=\mathbb{C}^{\hom}(d):\mathbf{E} \tag{20}$$

$\boldsymbol{\Sigma}$ is the macroscopic stress tensor. Due to the isotropic behaviors of all constituents of the claystone, the macroscopic elastic stiffness tensor writes:

$$\mathbb{C}^{\hom}(d)=3k^{\hom}(d)\mathbb{J}+2\mu^{\hom}(d)\mathbb{K} \tag{21}$$

Now it is needed to evaluate the macroscopic elastic moduli of the claystone, namely $k^{\hom}(d)$ and $\mu^{\hom}(d)$ using linear homogenization method. We propose to compare two different homogenization schemes, dilute and Mori-Tanaka (1975), together with Voigt upper bound. The macroscopic elastic moduli of the claystone corresponding to these schemes are given below.

Voigt bound:

Putting $\mathbb{A}^{r}=\mathbb{I}$, the Voigt bound of the effective elastic moduli is given by:

$$\begin{aligned} k^{\hom}(d) &= f_0k_0(d)+f_1k_1+f_2k_2 \\ \mu^{\hom}(d) &= f_0\mu_0(d)+f_1\mu_1+f_2\mu_2 \end{aligned} \tag{22}$$

$f^r (r = 0,1,2)$ represents the volumetric fraction of each constituent. For the sake of convenience, the clay matrix is indicated by the index 0.

Dilute scheme:

By neglecting interactions between different constituents, one gets strain concentration tensor:

$$\mathbb{A}^r = \left(\mathbb{I} + \mathbb{P}_{\mathrm{I}_r}^0 : \left(\mathbb{C}_r - \mathbb{C}_0(d) \right) \right)^{-1} \tag{23}$$

Assuming spherical inclusions for quartz and calcite grains, Hill tensor is given by:

$$\mathbb{P}_{\mathrm{I}_r}^0 = \frac{\beta_0(d)}{2\mu_0(d)} \mathbb{K} + \frac{\alpha_0(d)}{3k_0(d)} \mathbb{J} \tag{24}$$

with $\alpha_0(d) = \dfrac{3k_0(d)}{3k_0(d) + 4\mu_0(d)}$ and $\beta_0(d) = \dfrac{6\left(k_0(d) + 2\mu_0(d)\right)}{5\left(3k_0(d) + 4\mu_0(d)\right)}$.

Finally, the effective elastic moduli are given by:

$$\begin{aligned} k^{\mathrm{hom}}(d) &= k_0(d) + \sum_{r=1}^{2} f_r \frac{\left(k_r - k_0(d)\right)\left(3k_0(d) + 4\mu_0(d)\right)}{3k_r + 4\mu_0(d)} \\ \mu^{\mathrm{hom}}(d) &= \mu_0(d) + \sum_{r=1}^{2} f_r \frac{5\mu_0(d)\left(\mu_r - \mu_0(d)\right)\left(3k_0(d) + 4\mu_0(d)\right)}{\mu_0(d)\left(9k_0(d) + 8\mu_0(d)\right) + 6\mu_r\left(k_0(d) + 2\mu_0(d)\right)} \end{aligned} \tag{25}$$

Mori-Tanaka Estimation:

In this estimation, interactions between three constituents are taken into account by considering suitable uniform strain boundary conditions (Nemat-Nasser and Hori, 1993). The strain concentration tensor writes:

$$\mathbb{A}^r = \left(\mathbb{P}_{\mathrm{I}_r}^0 : \left(\mathbb{C}_r - \mathbb{C}_0(d) \right)^{-1} + \mathbb{I} \right)^{-1} : \left(\sum_{s=0}^{2} f_s \left(\mathbb{P}_{\mathrm{I}_s}^0 : \left(\mathbb{C}_s - \mathbb{C}_0(d) \right)^{-1} + \mathbb{I} \right)^{-1} \right)^{-1} \tag{26}$$

The effective elastic moduli are then determined:

$$k^{\hom}(d)=\left(\sum_{r=0}^{2} f_r \frac{k_r}{3k_r+4\mu_0(d)}\right)\left(\sum_{s=0}^{2}\frac{f_s}{3k_s+4\mu_0(d)}\right)^{-1}$$
$$\mu^{\hom}(d)=\frac{\sum_{r=1}^{2} f_r \dfrac{\mu_r}{\mu_0(d)\left(9k_0(d)+8\mu_0(d)\right)+6\mu_r\left(k_0(d)+2\mu_0(d)\right)}}{\sum_{s=1}^{2}\dfrac{f_s}{\mu_0(d)\left(9k_0(d)+8\mu_0(d)\right)+6\mu_s\left(k_0(d)+2\mu_0(d)\right)}} \quad (27)$$

As shown above, the macroscopic behavior of the claystone depends on the damage evolution of the clay matrix. Due to the time-dependent subcritical propagation of microcracks inside the clay matrix, the effective elastic properties of the claystone will progressively evolve generating additional strains in the material. In order to show the time-dependent evolution of strains, it is convenient to express the constitutive relations (18) in the inverse form:

$$\mathbf{E}=\mathbb{M}(d):\boldsymbol{\Sigma}\ ,\ \ \mathbb{M}(d)=\mathbb{C}(d)^{-1}=\frac{1}{3k^{\hom}(d)}\mathbb{J}+\frac{1}{2\mu^{\hom}(d)}\mathbb{K} \quad (28)$$

$\mathbb{M}(d)$ denotes the macroscopic compliance tensor of the claystone. The rate form of the constitutive relations (26) can be written as:

$$\dot{\mathbf{E}}=\mathbb{M}(d):\dot{\boldsymbol{\Sigma}}+\left(\frac{\partial\mathbb{M}(d)}{\partial d}:\boldsymbol{\Sigma}\right)\dot{d} \quad (29)$$

We can see that in creep loading conditions with $\dot{\Sigma}_{ij}=0$, the evolution of strains is fully generated by the subcritical damage growth in the clay matrix.

3.4 Numerical implementation

In view of application of the proposed model to general loading conditions, the proposed micromechanical model is implemented in the standard ABAQUS code using the UMAT subroutine. We present here the numerical algorithm used for the local integration of the constitutive model at each Gauss point. Note that the algorithm proposed here is quite general with the possibility to consider other local constitutive models of constituents and other homogenisation schemes.

The loading path is divided into a number of steps. At the step $(n+1)$, the strain at the step (n) is known and the strain increment $\Delta\mathbf{E}_{n+1}$ is given. Therefore, the material point at the macroscopic scale is subjected to the macroscopic strain $\mathbf{E}_{(n+1)}=\mathbf{E}_{(n)}+\Delta\mathbf{E}_{(n+1)}$. The problem to be solved here is to find the corresponding

macroscopic stress state at the end of loading step by using the homogenization method presented above. The following numerical algorithm is proposed.

1. Input data at the time step (t_{n+1}): $\mathbf{E}_{(n+1)}$, $\Delta\mathbf{E}_{(n+1)}$, Δt_{n+1} and local strain fields in all constituents:
   - clay matrix, $\boldsymbol{\varepsilon}_{0(n)}$, d_n
   - quartz grains $\boldsymbol{\varepsilon}_{1(n)}$
   - calcite grains: $\boldsymbol{\varepsilon}_{2(n)}$
2. Put trial strain fields in the quartz and calcite phases as:

$$\left(\Delta\boldsymbol{\varepsilon}_1\right)^i_{(n+1)} := \Delta\mathbf{E}_{(n+1)}, \qquad \left(\Delta\boldsymbol{\varepsilon}_2\right)^i_{(n+1)} := \Delta\mathbf{E}_{(n+1)}$$

3. The local strain in the clay matrix is evaluated by:

$$\left(\Delta\boldsymbol{\varepsilon}_0\right)^i_{(n+1)} = \frac{\Delta\mathbf{E}_{(n+1)} - f_1\left(\Delta\boldsymbol{\varepsilon}_1\right)^i_{(n+1)} - f_2\left(\Delta\boldsymbol{\varepsilon}_2\right)^i_{(n+1)}}{1 - f_1 - f_2}$$

4. At the iterate i, for the clay matrix, the values of $\left(\Delta\boldsymbol{\varepsilon}_0\right)^i_{(n+1)}$, $\left(\boldsymbol{\varepsilon}_0\right)_{(n)}$ and d_n are known. One can compute $\left(\boldsymbol{\varepsilon}_0\right)^i_{(n+1)}$, d^i_{n+1}, $\mu_0\left(d^i_{n+1}\right)$, $k_0\left(d^i_{n+1}\right)$ and $\mathbb{C}_0\left(d^i_{n+1}\right)$. For the phase (1) and phase (2), the elastic stiffness $\mathbb{C}_1$ and $\mathbb{C}_2$ are constant.
5. The Hill tensor is evaluated using (24).
6. According to the homogenization scheme, the strain concentration tensors $\mathbb{A}^i_0$, $\mathbb{A}^i_1$ and $\mathbb{A}^i_2$ are evaluated.
7. Check the compatibility of local strains between two iterates for the phase (1) and phase (2) and compute the errors:

$$\mathbf{R}^i_1 := \mathbb{A}^i_1 : \Delta\mathbf{E} - \Delta\boldsymbol{\varepsilon}^i_1$$

$$\mathbf{R}^i_2 := \mathbb{A}^i_2 : \Delta\mathbf{E} - \Delta\boldsymbol{\varepsilon}^i_2$$

If $\left\|\mathbf{R}^i_1\right\| < tolerance\ 1$ and $\left\|\mathbf{R}^i_2\right\| < tolerance\ 2$, the compatibility is reached.

Else an additional iteration is required until the two above convergence criteria are attained and in that situation, one sets:

$$\left(\Delta\boldsymbol{\varepsilon}_1\right)_{(n+1)}^{i+1} = \left(\Delta\boldsymbol{\varepsilon}_1\right)_{(n+1)}^{i} + \mathbf{R}_1^i$$

$$\left(\Delta\boldsymbol{\varepsilon}_2\right)_{(n+1)}^{i+1} = \left(\Delta\boldsymbol{\varepsilon}_2\right)_{(n+1)}^{i} + \mathbf{R}_2^i$$

and return to the step 3.

8. According to the homogenization scheme, the macroscopic is updated using (21) and the macroscopic stress tensor is calculated as:

$$\boldsymbol{\Sigma}_{(n+1)} = \mathbb{C}^{\text{hom}}\left(d_{(n+1)}\right) : \left(\mathbf{E}_{(n)} + \Delta\mathbf{E}_{(n+1)}\right)$$

4. Numerical evaluation and experimental validation

Using the implementation algorithm presented above, we present now the numerical evaluation and experimental validation of the proposed model. For this purpose, typical mechanical parameters are given in Table 1 for three constituents of the claystone.

Table 1: Typical parameters for three constituents of claystone

constituent	Elastic parameters	Damage parameters
Clay matrix $f_0 = 60\%$	$\tilde{E}_0 = 3000\,\text{MPa}$, $\tilde{\nu}_0 = 0.2$	$B_t = 400$, $B_c = 400$, $n^t = 1.5$, $n^c = 1.5$, $\xi_t = 0.1$, $\xi_c = 0.1$
Calcite $f_1 = 20\%$	$E_1 = 95000\,\text{MPa}$, $\nu_1 = 0.27$	
Quartz $f_2 = 20\%$	$E_2 = 100000\,\text{MPa}$, $\nu_2 = 0.06$	

3.5 Uniaxial compression creep test

Consider first a uniaxial compression creep test under a constant axial stress of $\Sigma_{11} = -8\,\text{MPa}$. The numerical simulation is done using the dilute damage scheme for closed cracks inside the clay matrix, as indicated in the relations (10). In Fig.1, we

present the evolutions of axial strain with time respectively for the clay matrix alone without inclusion and the claystone with inclusions using three different homogenization schemes: dilute, Mori-Tanaka and Voigt bound. Logically, the creep strain of the clay matrix without inclusions is much larger than that of the claystone with mineral inclusions which reinforce the macroscopic mechanical strength and reduce the creep rate. Comparing now the results obtained by three homogenization schemes. It is found that the homogenization based on Voigt bounds drastically reduces the creep strain of the clay matrix on the macroscopic scale by overestimating the reinforcement of quartz and calcite inclusions. The creep strain from the dilute scheme is larger than that from Mori-Tanaka one. This difference may be due to the interactions between constituent phases inside the claystone, which are taken into account in the Mori-Tanaka scheme while neglected in the dilute one.

In order to further exploit the numerical results, the evolution of axial compliance with time is evaluated. Under a uniaxial compression, the axial compliance is defined by the macroscopic stress-strain relation: $E_{11} = M^{\hom}(d) \times \sum_{11}$, with the axial compliance given by:

$$M^{\hom}(d) = \frac{3k^{\hom}(d) + \mu^{\hom}(d)}{9(1-d)k^{\hom}(d)\mu^{\hom}(d)} \tag{30}$$

The effective elastic moduli $k^{\hom}(d)$ and $\mu^{\hom}(d)$ are calculated by three homogenization scheme. The evolutions of axial elastic compliance are given in Fig.2. One can see that the elastic compliance is reduced by the presence of mineral inclusions and the compliance for the dilute scheme is larger than that from MT scheme. This is in concordance with the creep strain presented in Fig. 1.

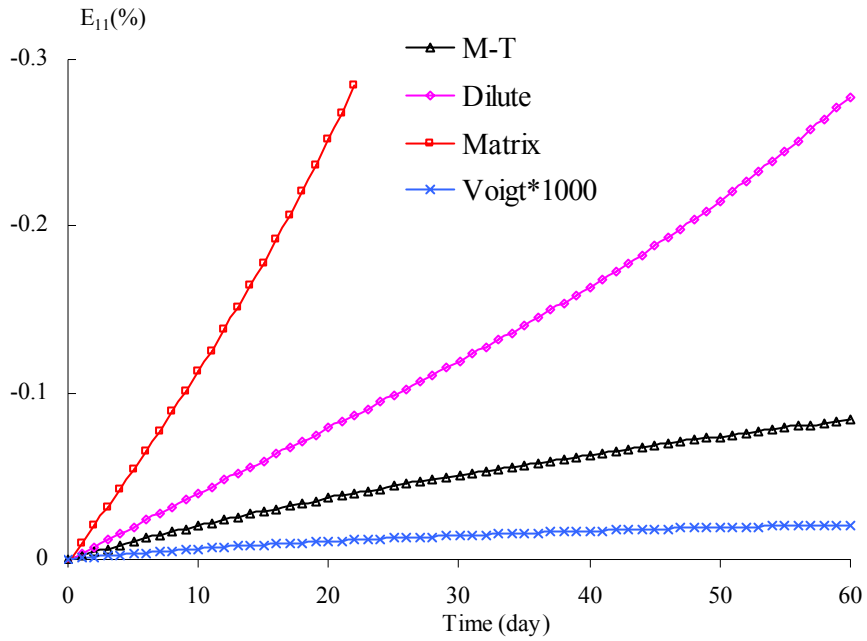

Fig.1 Evolutions of axial strain with time in uniaxial compression creep obtained by different homogenization schemes

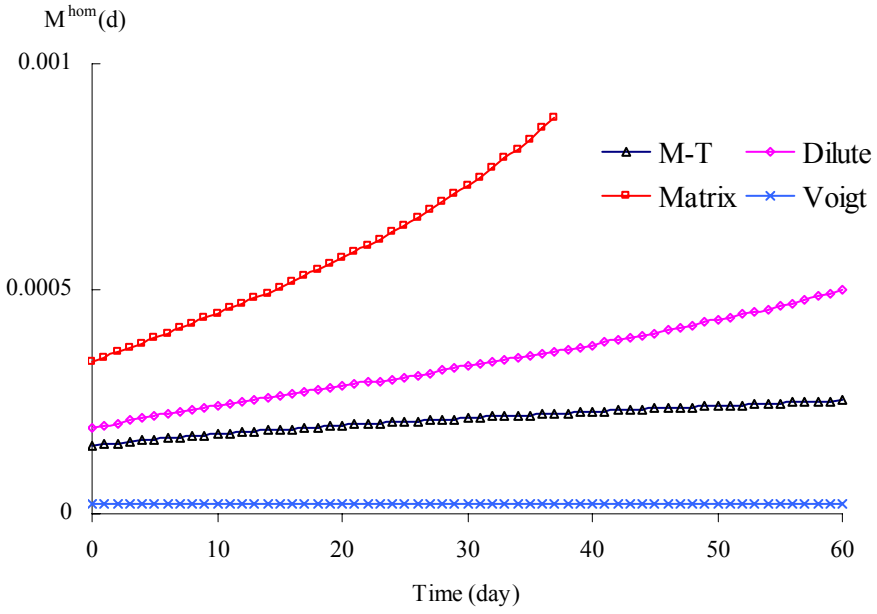

Fig.2 Evolutions of axial compliance with time in uniaxial compression creep obtained by different homogenization schemes

The evolutions of damage variable with time inside the clay matrix are presented in Fig.3. It is interesting to find that the presence of inclusions significantly reduces the

evolution kinetics of damage inside the clay matrix. The differences between different homogenization schemes are important and related to different distribution of local strain fields inside the mineral constituents. One can note that there is a notable effect of the interaction between constituent phases on the evolution of time-dependent growth of microcracks. For the sake of completeness, the relationship between the macroscopic axial compliance and the local damage inside clay matrix is shown in Fig.4. One can observe that there is a certain limit value of damage variable at mesoscopic scale, generating an accelerated increase of the macroscopic compliance. This can be the origin of macroscopic material failure by secondly or tertiary creep deformation.

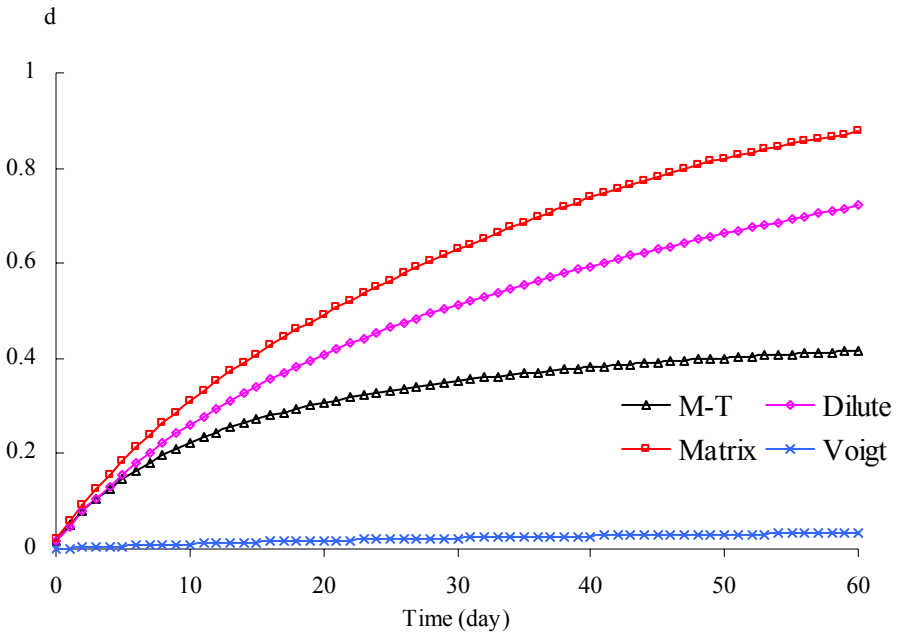

Fig.3 Evolutions of damage in clay matrix with time in uniaxial compression creep obtained by different homogenization schemes

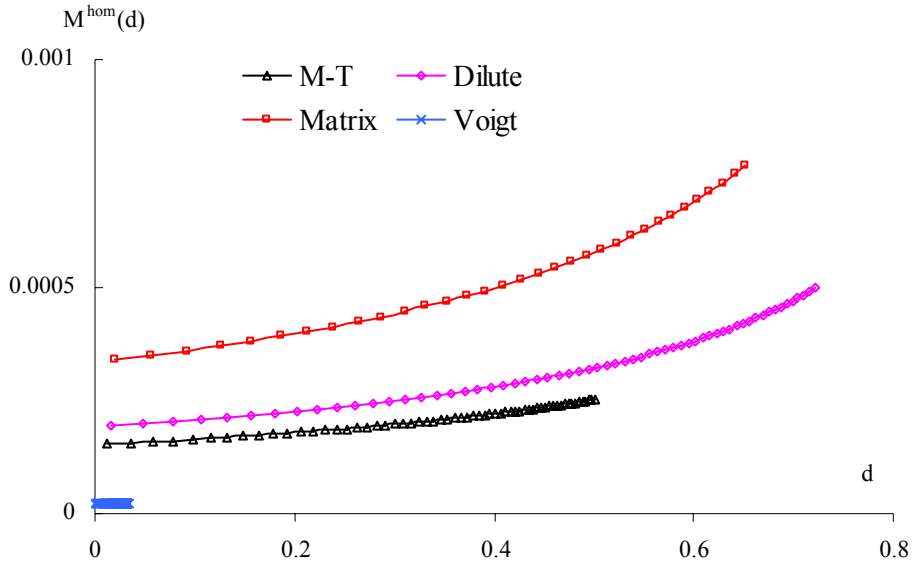

Fig.4 Relationships between macroscopic elastic compliance and local damage in clay matrix

3.6 Uniaxial tensile creep test

For the purpose of comparison, consider now a uniaxial tensile creep test under a constant axial stress of $\Sigma_{11} = 8\,\mathrm{MPa}$. In this case, the numerical simulation is done using the dilute damage scheme for open cracks inside the clay matrix, as indicated in the relations (9). However, for the determination of macroscopic behaviour of the claystone, only the Mori-Tanaka scheme is adopted leading to the affective elastic moduli given by (27). This scheme is preferred because it allows taking into account of interactions between three constituents. The emphasis here is to show the influence of loading path on the macroscopic creep strain of the claystone. In Fig. 5a, the evolutions of axial strain with time are presented and compared between the uniaxial compression and tension. The evolutions of damage in the clay matrix are shown in Fig.5b. One can see a strong influence of loading path on both damage evolution and macroscopic creep strain. Under the tensile stress, due to opening of microcracks, the damage evolution is faster than that under the compressive stress and may become unstable with time. The difference of damage evolution in the clay matrix leads to significantly different creep deformation of the claystone at macroscopic scale. The creep strain is much larger under the tensile stress than under the compressive one. Further, the creep strain under the tensile stress exhibits the transition from primary to tertiary creep leading to unstable failure of material.

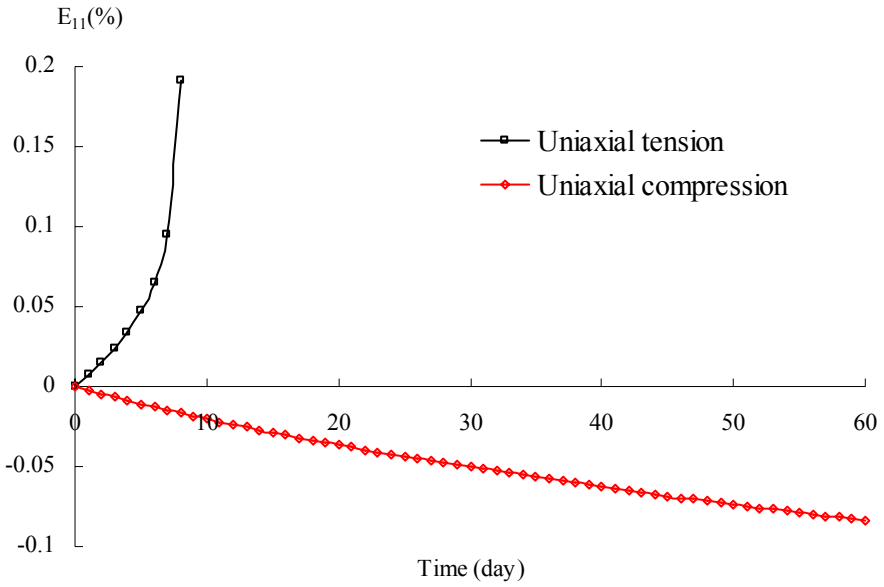

(a)

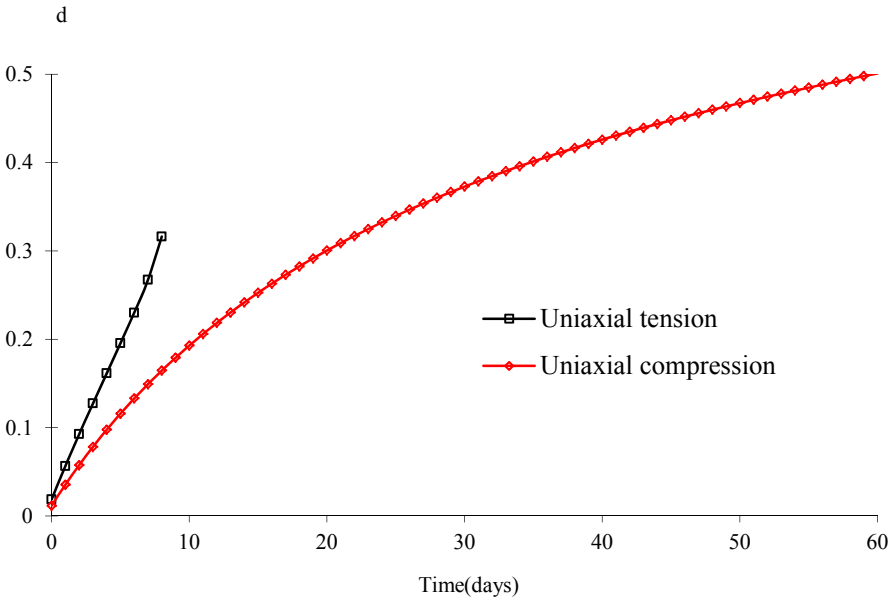

(b)

Fig.5 Evolutions of axial strain (a) and local damage (b) with time: comparison between uniaxial tension and compression creep using MT scheme

3.7 Influence of damage homogenization scheme

In the numerical simulations presented above, the dilute damage scheme is used for the determination of effective elastic properties of cracked clay matrix. In order to capture influences of homogenization scheme for local damage modelling in the clay

matrix, comparative simulations are performed using the PCW scheme as mentioned by the relations (11) and (12) for both open and closed microcracks. In Fig. 6, we present the evolutions of axial strain with time during the uniaxial compression creep, respectively obtained by using the dilute and PCW schemes for damage modelling in the clay matrix. It is found that the creep strain obtained with PCW damage scheme is smaller than that with the dilute one. This difference is due to the effect of interactions between microcracks, which is taken into account in PCW scheme but neglected in the dilute one. However, it seems that the difference between two scheme remains quite small compared with that between the homogenization schemes used for the macroscopic behaviour of the claystone.

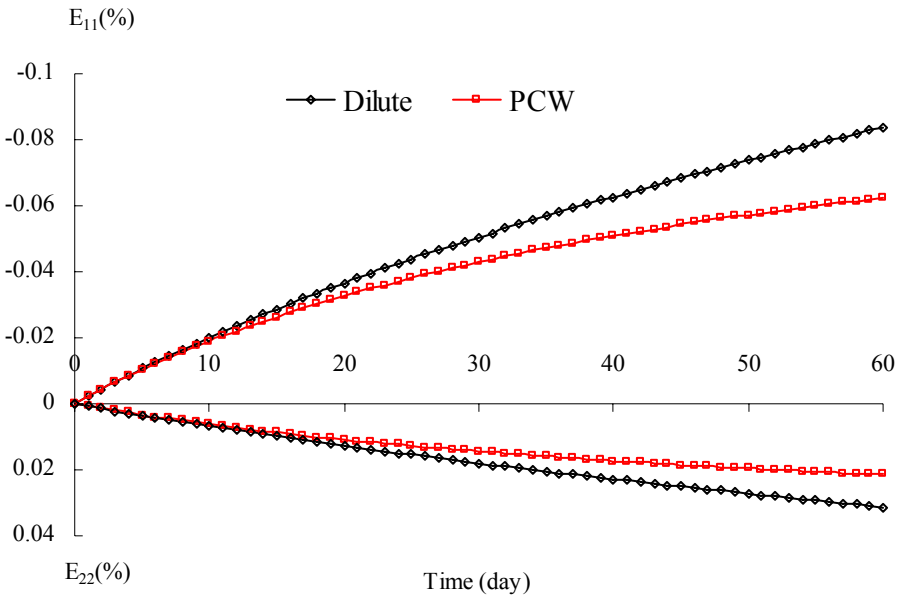

Fig.6 Evolutions of axial strain with time in uniaxial compression creep: comparisons between dilute and PCW schemes for damage modelling in clay matrix

3.8 Experimental validation

After the numerical evaluation of the proposed model in different loading paths and using different homogenization schemes, we present now the comparisons between numerical results and experimental data. The numerical results are obtained by using the dilute scheme for damage modeling in the clay matrix at mesoscopic scale and the MT scheme for the macroscopic behavior of the claystone. The mechanical parameters used are given in Table 1. In Fig. 7, we present the evolutions of axial strain during two uniaxial creep tests with different stress levels for two claystone samples with different mineral compositions. One can see that the

numerical results are in good agreement with experimental data. The proposed model seems to correctly capture time-dependent behaviors of the claystone due to sub-critical propagation of microcracks inside the clay matrix. The influences of mineral compositions are also well reproduced.

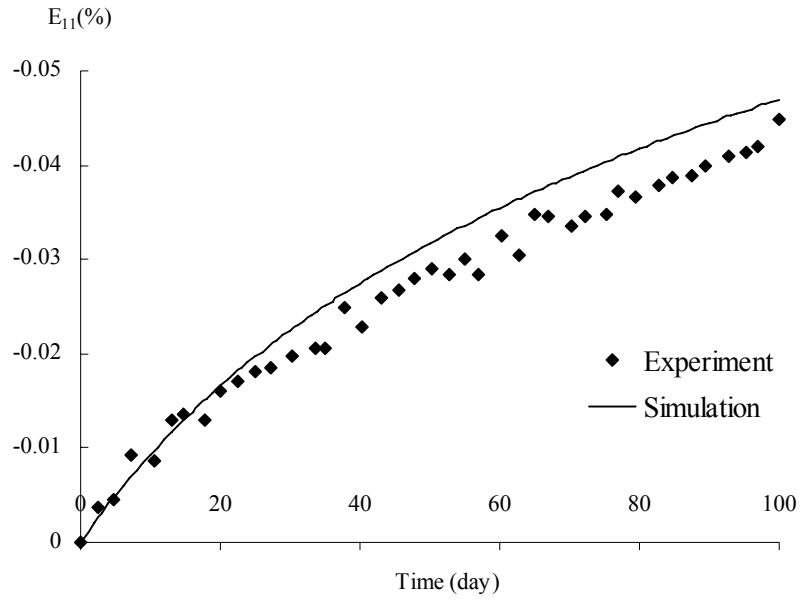

(a) $f_0 = 0.30$, $f_1 = 0.36$, $f_2 = 0.34$, $\Sigma_{11} = -9.9\,\mathrm{MPa}$

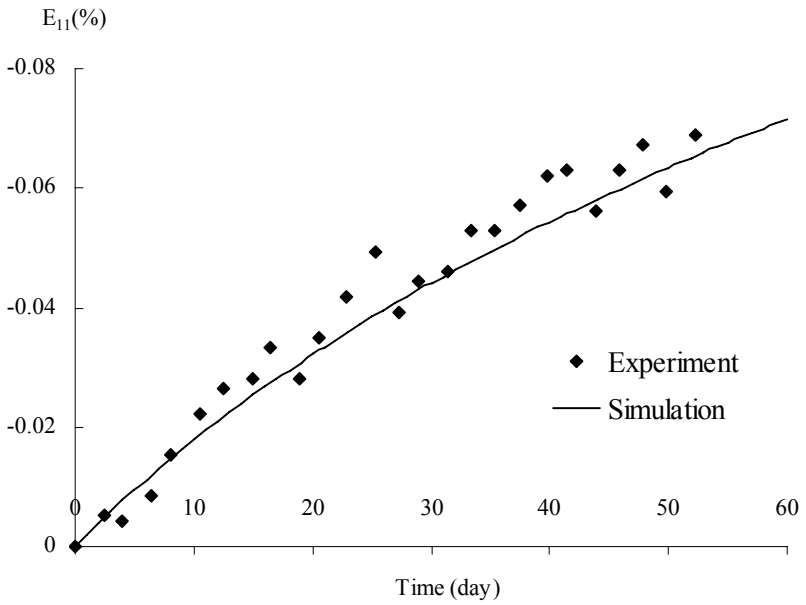

(b) $f_0 = 0.56$, $f_1 = 0.20$, $f_2 = 0.24$, $\Sigma_{11} = -8\,\mathrm{MPa}$

Fig.7 Comparison between numerical results and experimental data in uniaxial compression creep

3.9 Conclusion

In this work, a micromechanical constitutive model is proposed for the description of time-dependent behavior of the Callovo-Oxfordian claystone. The claystone is considered as a three-phase composite containing a clay matrix in which quartz and calcite grains are embedded. The time-dependent strains are related to the subcritical growth of microcracks inside the clay matrix. A two-step homogenization approach is developed. A micromechanics-based isotropic damage model is first formulated for modeling the subcritical damage of the clay matrix using both the dilute and PCW schemes. Dissymmetric responses between open and closed cracks as well as interactions between cracks are taken into account. A second-step homogenization process is used for the determination of macroscopic behavior of the claystone by taking into account effects of quartz and calcite grains. Numerical evaluations of the proposed model are performed for tensile and compressive creep tests to capture the influences of homogenization schemes respectively used in the two steps of homogenization process. It is found that the macroscopic response of the claystone is more sensitive to the scheme used for the mesoscopic to macroscopic upscaling than that used for the microscopic to mesoscopic upscaling. When the interaction between microcracks is taken into account using PCW scheme for the damage modeling of clay matrix, the macroscopic creep strain is smaller than that obtained with the dilute scheme when the interaction is neglected. On the other hand, the macroscopic creep strain of the claystone is significantly reduced by the presence of mineral inclusions and strongly depends on the averaging scheme used. The scheme based on Voigt bound largely overestimates the effect of inclusions while the dilute one leads to an underestimation. The model based on MT scheme provides most consistent results. Finally, the numerical results are in good agreement with experimental data in creep tests. The proposed model correctly reproduces the effects of stress level and mineral compositions. The present work can be extended to include various aspects, for instance effects of interfaces between the clay matrix and mineral inclusions, anisotropic damage in the clay matrix, time-dependent healing of microcracks.

References

Abou-Chakra Guery A, Cormery F, Shao JF, Kondo D. (2008), A micromechanical model of elastoplastic and damage behavior of a cohesive geomaterial. Int J. Solids Struct. 45, 1406–29.

Abou-Chakra Guery A, Cormery F, Shao JF, Kondo D. (2009), A multiscale modeling of damage and time-dependent behavior of cohesive rocks. Int. J. for numerical and analytical methods in Geomechanics 33, 567-589

Anderson OL, Grew PC. (1977), Stress corrosion theory of crack propagation with application to geophysics. Rev. Geophys. Space Phys. 15, 77-104.

Atkinson BK. (1984), Subcritical crack growth in geological materials. J. Geophys. Res. 89, 4077-4114.

Bornert M, Vales F, Gharbi H, Nguyen Minh D. (2010), Multiscale full-field strain measurements for micromechanical investigations of the hydromechanical behaviour of clayey rocks. Strain 46, 33–46.

Budiansky, B., O'Connell, RJ. (1976). Elastic moduli of a cracked solid, International Journal of Solids and Structures 12, 81-97

Chaboche, J.L. (1981), Continuous damage mechanics – A tool to describe phenomena before crack initiation, Nuclear Engineering and Design 64, 233-247

Chan, K. S., Bodner, S. R., Fossum, A. F. and Munson D. E. (1997). A Damage Mechanics Treatment of Creep Failure in Rock Salt, International Journal of Damage Mechanics 6(2), 121-152.

Chau, K. T. and Wong R.H. C. (1997). Effective Moduli of Microcracked Rocks: Theories and Experiments, International Journal of Damage Mechanics 6(3), 258-277

Chen L., Duveau G. and Shao J.F. (2011), Modelling of plastic deformation and damage in cement-based material subjected to desiccation, International journal for numerical and analytical methods in Geomechanics 35, 1877-1898

Chiarelli A.S., Shao JF, Hoteit N. (2003), Modeling of elastoplastic damage behaviour of a claystone. Int. J. Plasticity 19, 23–45.

Comi, C., Perego, U. (2010). Anisotropic Damage Model for Concrete Affected by Alkali-Aggregate Reaction, International Journal of Damage Mechanics 20, 598-617

Eshelby, J., (1957). The determination of the elastic field of an ellipsoidal inclusion and related problems, Proc. R. Soc. London A. 241, 375–396

Halm, D., Dragon, A., (1996). A model of anisotropic damage by mesocrack growth: unilateral effect. Int. J. Damage Mech. 5, 384-402.

Hayakawa, K. and Murakami, S. (1997). Thermodynamical modeling of elastic-plastic damage and experimental validation of damage potential, Int. J. Damage Mech. 6, 333-363.

Henry JP, Paquet J, Tancrez JP. (1977), Experimental study of crack propagation in calcite rocks, Int. J. Rock Mech Min Sci Geomech Abstr 14, 85-91.

Ju, J.W. (1989). On energy based coupled elastoplastic damage theories: constitutive modeling and computational aspects, Int. J. Solids Structures 25(7), 803-833. 1989

Ju JW, Yuan KY, Kuo AW (2012), Novel strain energy based coupled elastoplastic damage and healing models for geomaterials – Part I: formulations, Int. J. of damage Mechanics 21, 525- 549

Lebon P., Mouroux B. (1999), Knowledge of the three French underground laboratory sites, Engineering Geology 52, 251-256

Lemaitre, J. (1984). How to use damage mechanics, Nuclear Engineering and Design 80, 233-245

Marigo, J.J. (1985). Modeling of brittle and fatigue damage for elastic material by growth of microvoids, Engineering Fracture Mechanics 21, 861-874

Mazars, J. (1986). A description of micro-and macroscale damage of concrete structures, Engineering Fracture Mechanics 25, 729-737

Mori, T., Tanaka, K. (1973), Average stress in matrix and average elastic energy of materials with misfitting inclusions. Acta Metallurgica. 21, 571-574

Nara Y., K. Kaneko. (2005), Study of subcritical crack growth in Andesite using the Double Torsion test. International Journal of Rock Mechanics & Mining Sciences 42, 521-530.

Nara Y, Kaneko K, (2006), Sub-critical crack growth in anisotropic rock, International Journal of Rock Mechanics & Mining Sciences 43, 437–453

Nemat-Nasser, S. and Hori, M. (1993). Micromechanics: overall properties of heterogeneous materials, North-Holland, Amsterdam, The Netherlands.

Pietruszczak S, Lydzba D, Shao JF. (2004), Description of creep in frictional materials in terms of microstructure evolution, Journal of Engineering Mechanics ASCE 130, 681-690

Pijaudier-Cabot, G,. and Bazant, Z. P. (1987), Nonlocal Damage Theory. Journal of Engineering Mechanics ASCE 113(10), 1512-1533

Ponte-Castaneda, P., Willis, J.-R., (1995), The effect of spatial distribution of effective behavior of composite materials and cracked media. Journal of the Mechanics and Physics of Solids 43, 1919-1951

Robinet JC. (2008), Mineralogie, porosite et diffusion des solutes dans l'argilite du callovo-oxfordien de bure (meuse/haute-marne, France) de l'échelle centimétrique à micrométrique. Doctoral thesis, University of Poitiers, France

Shao JF, Zhu QZ, Su K. (2003), Description of creep in rock materials in terms of material degradation, Computer and Geotechnics 30, 549-555

Shen WQ, Shao JF, Kondo D, Gatmiri B. (2012), A micro-macro model for clayey rocks with a plastic compressible porous matrix, International journal of plasticity 36, 64–85

Voyiadjis G.Z., Taqieddin Z.N. and Kattan P.I. (2008), Theoretical Formulation of a

Coupled Elastic—Plastic Anisotropic Damage Model for Concrete using the Strain Energy Equivalence Concept, International Journal of Damage Mechanics 18, 603-638

Yang DS, Billiotte J, Su K. (2010), Characterization of the hydromechanical behavior of argillaceous rocks with effective gas permeability under deviatoric stress. Engineering Geology 114, 116-122

Waza T, Kurita K, Mizutani H. (1980), The effect of water on the subcritical crack growth in silicate rocks. Tectonophys 67, 25-34.

Zhou H, Jia Y, Shao JF. (2008), A unified elastic - plastic and viscoplastic damage model for quasi brittle rocks. International journal of rock mechanics and mining sciences 45, 1237-1251

Zhu, QZ., Kondo, D., Shao, JF. (2008). Micromechanical analysis of coupling between anisotropic damage and friction in quasi brittle materials: role of the homogenization scheme. International Journal of Solids and Structures 45, 1385-1405

Chapter 4
Micro-macro modeling of time-dependent behavior of argillite with effects of clay matrix porosity

Résumé du chapitre

Comme indiqué dans le chapitre précédent, deux mécanismes peuvent être envisagés pour le comportement différé des argilites du Callovo-Oxfordien : déformation viscoplastique de la matrice argileuse et la propagation subcritique de microfissures. Le deuxième mécanisme a été abordé dans le chapitre précédent. Dans ce chapitre nous nous intéressons au comportement différé lié à la déformation viscoplastique de la matrice argileuse. Nous rappelons que l'argilite du Callovo-Oxfordien est principalement composée de quartz, calcite et minéraux argileux [Sammartino, 2001]) et une petite quantité de dolomite, feldspath et pyrite [Valès, 2001]). On trouve des grains principaux (quartz et de calcite) dans l'ordre du micron et on observe également des vides infra micrométriques à nanométriques qui sont préférentiellement associé à l'arrangement des particules argileuse: porosité intra-agrégats; il n'y a pas ou pratiquement pas de porosité intra grains. Selon cette analyse minéralogique, une modélisation à deux échelles doit être considérée: à l'échelle mésoscopique, les argilites sont composées d'une matrice argileuse poreuse dans laquelle sont noyés des inclusions minérales élastiques; à plus petite échelle (l'échelle microscopique), la matrice argileuse est elle-même constituée d'une phase solide qui est un assemblage de particules d'argiles et de pores. Un modèle micro-macro basé sur une procédure d'homogénéisation en deux étapes, du micro au méso et du méso à macro, a été récemment proposé par Shen et al. [Shen et al. 2011] pour le comportement élastoplastique de l'argilite du Callovo-Oxfordien. Dans ce chapitre nous proposons une extension du modèle homogénéisé en deux étapes pour le comportement différé de l'argilite du Callovo-Oxfordien. Pour ce faire, l'argilite est considéré comme un composite à deux phases avec la matrice poreuse et des inclusions minérales. La matrice d'argile poreuse est décrite par un modèle élasto-viscoplastique, tandis que les inclusions sont considérées comme des milieux élastiques linéaires. Pour déterminer le comportement différé macroscopique de l'argilite, une approche incrémentale modifiée basée sur les travaux de [Hill, 1965a] est proposée pour cette nouvelle représentation des argilites.

S'agissant du comportement différé d'un composite avec des phases viscoplastiques,

un opérateur tangent algorithmique est souvent introduit à partir d'une linéarisation des équations constitutives pour déterminer le tenseur de localisation car un opérateur tangent physique ne peut être défini dans ce cas [Guéry Abou-Chakra, 2008]. Cependant, cet opérateur algorithmique n'a pas de base physique. Dans notre étude, une nouvelle méthode est proposée. Considérant que le comportement plastique instantané est un cas particulier de celui viscoplastique, il est possible de définir un opérateur tangent élastoplastique à un instant donné. Nous proposons d'utiliser cet opérateur tangent instantané pour la détermination des tenseurs d'Eshelby. Par ailleurs, pour l'homogénéisation micro-méso, une fonction de charge de type Drucker-Prager est adoptée pour tenir compte de la sensibilité à la pression de confinement et de la compressibilité plastique de la phase solide au sein de la matrice argileuse. Une loi d'écoulement viscoplastique associée sera appliquée comme une première approche. Les résultats de simulation montrent que même si le modèle décrit qualitativement le comportement non linéaire de l'argilite sous la compression uniaxiale et triaxiale, il existe un écart quantitatif important entre la prédiction et les données expérimentales. En vue de mieux reproduire les comportements mécaniques de la roche argileuse, une loi d'écoulement viscoplastique non associée sera ensuite introduite. La validité du modèle proposé est vérifiée en comparant les résultats numériques avec les données expérimentales.

This chapter is devoted to a micro-macro modeling of time-dependent behavior of the Callovo-Oxfordian argillite. As largely known, the Callovo-Oxfordian argillite is mainly composed of quartz, calcite and clay minerals (Sammartino, 2001) and a small quantity of dolomite, feldspar and pyrite (Valès, 2001). The main grains (quartz and calcite) are in micron scale and the majority of porosity is due to inter-aggregates pores, from sub-micron to nanometer, which are preferentially associated with the arrangement of clay particles. According to this mineralogical analysis, a two-scale micro-macro modeling should be considered: at a mesoscopic scale, the argillite is composed of a continuous porous clay matrix which is embedded by mineral inclusions; at a smaller scale, the clay matrix is itself constituted of a solid phase which is an assembly of clay particles and pores between such particles. The present work extends the two scale micro-macro modeling of instantaneous elastoplastic behavior of argillites, recently proposed by Shen and al. (2012), to time dependent behavior. Therefore, the argillite is considered as a two phase composite with the porous clay matrix and mineral inclusions. The effective properties of the porous clay matrix are described by an elastic-viscoplastic model while the inclusions are considered as linear elastic media. The loading function of viscoplastic flow for the clay matrix is issued from a first homogenization step considering a plastically compressible solid phase described by a Drucker-Prager type criterion (Maghous, Dormieux and Barthèlemy, 2009) taking into account the influence of confining pressure. Further, the loading function depends explicitly on the porosity of clay matrix. For the determination of macroscopic time-dependent behavior of the argillite, a modified Hill's incremental method is used (Hill, 1965).

4.1 Modeling of the porous clay matrix with associated viscoplastic flow rule of the clay matrix

Fig.1 shows the two-step procedures of homogenization adopted in this chapter. It contains two steps: the porous clay matrix is transformed to the homogeneous nonlinear material through "the first homogenization" in microscopic scale and then, by means of "the second homogenization", the heterogeneous argillite is equivalent to a homogeneous material in macroscopic scale.

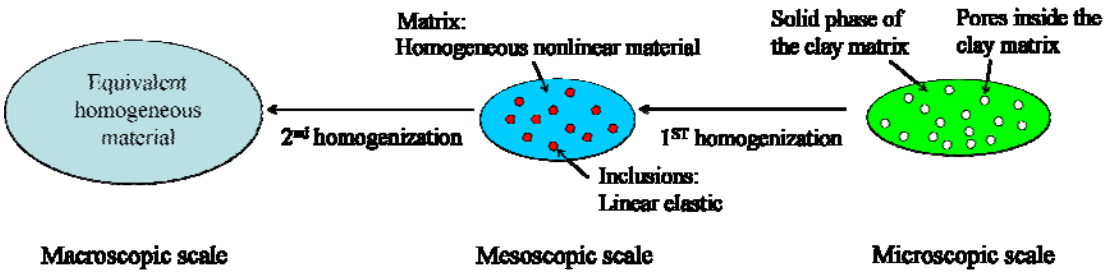

Fig.1 Two-step procedures of homogenization

4.1.1 Formulation of the model

In the first step we consider the homogenization of the porous clay matrix, which constitutes the micro-meso upscaling. In order to describe the dependence of plastic yield condition on the mean stress, a Drucker-Prager type criterion (Drucker and Prager, 1952) is adopted for the solid phase of clay matrix:

$$\phi^m(\boldsymbol{\sigma}) = q + \alpha\left(\sigma_m - c_{vp}\right) \tag{1}$$

where q and σ_m represent the local equivalent deviatoric stress and mean stress respectively in the solid phase. The parameter c_{vp} corresponds to hydrostatic tensile strength related to material (solid phase) cohesion. α represents the material friction coefficient which is used as a hardening function to define current yield stress of solid phase.

According to the previous works by Maghous and al. (Maghous et al. 2009), the macroscopic plastic criterion of the porous clay matrix can be explicitly determined from a suitable non-linear homogenization method and written in the following form:

$$f\left(\tilde{\boldsymbol{\Sigma}}, \alpha, \varphi\right) = \frac{1+2\varphi/3}{\alpha^2}\tilde{Q}^2 + \left(\frac{3\varphi}{2\alpha^2} - 1\right)\tilde{\Sigma}_m^2 + 2\left(1-\varphi\right)c_{vp}\tilde{\Sigma}_m - \left(1-\varphi\right)^2 c_{vp}^2 \tag{2}$$

where $\tilde{\boldsymbol{\Sigma}}$ is the local stress tensor inside the clay matrix and, $\tilde{Q} = \sqrt{\tilde{\boldsymbol{\Sigma}}_d : \tilde{\boldsymbol{\Sigma}}_d}$, $\tilde{\boldsymbol{\Sigma}}_d = \tilde{\boldsymbol{\Sigma}} - \tilde{\Sigma}_m \mathbb{I}$. Note that this macroscopic criterion depends explicitly on the porosity of the clay matrix φ.

In our work, the previous plastic yield criterion is adopted and used as the loading function of viscoplastic behavior of the clay matrix. As the mechanical behavior of the clay matrix prior to failure state is generally not elastic, an elastic perfect plastic

model is not suitable. An appropriate viscoplastic hardening law is needed. In this study, the viscoplastic hardening process of solid phase is described by the variation of the friction coefficient α as a function of the equivalent viscoplastic strain of the solid phase of clay matrix γ^{vp}:

$$\alpha\left(\gamma^{vp}\right)=\left[\alpha_m^{vp}-\left(\alpha_m^{vp}-\alpha_0^{vp}\right)e^{-b\gamma^{vp}}\right] \tag{3}$$

in which α_0^{vp} and α_m^{vp} represent the initial threshold (at the point of elastic limit) and the ultimate value when the failure state is reached, respectively. The parameter b controls the kinetics of the evolution of viscoplastic hardening.

At the same time, on the basis of Mori-Tanaka homogenization estimate (Mori and Tanaka, 1973), the elastic properties of the clay matrix are related to those of its solid phase and porosity by:

$$k_0=\frac{4\left(1-\varphi\right)k_s\mu_s}{4\mu_s+3\varphi k_s},\qquad \mu_0=\frac{\left(1-\varphi\right)\mu_s}{1+6\varphi\dfrac{k_s+2\mu_s}{9k_s+8\mu_s}} \tag{4}$$

k_s and μ_s are respectively the bulk and shear moduli of the solid phase of the clay matrix. According to the experimental investigation, the overall porosity varies from 11% to 13.85% in the Callovo-Oxfordian argillite and the volumetric fraction of clay matrix is about 40% to 50%. Therefore, the initial porosity of the clay matrix at the microscopic scale is then typically $\varphi_0=25\%$.

Then, an associated viscoplastic flow rule is adopted for the solid phase of the clay matrix. As mentioned above, the yield function (2) is derived from a first homogenization step and used as the loading function for viscoplastic flow of the porous clay matrix at the mesoscopic scale. Thus, the clay matrix obeys also to an associated flow rule. The viscoplastic flow rule of the clay matrix can be written as follows:

$$\dot{\tilde{\mathbf{E}}}^{vp}=\dot{\lambda}\frac{\partial f}{\partial\tilde{\boldsymbol{\Sigma}}}\left(\tilde{\boldsymbol{\Sigma}},\alpha,\varphi\right) \tag{5}$$

where $\dot{\tilde{\mathbf{E}}}^{vp}$ is the viscoplastic strain rate of clay matrix. The viscoplastic multiplier $\dot{\lambda}$ is defined by:

$$\begin{aligned} \dot{\lambda} &= 0 && \text{if } f \le 0 \text{ (elasticity)} \\ \dot{\lambda} &= \frac{c_{vp}}{\eta}\left(\frac{f}{c_{vp}}\right)^m && \text{if } f > 0 \text{ (viscoplasticity)} \end{aligned} \tag{6}$$

Two parameters are introduced: the viscoplastic modulus η and the viscoplastic exponent m, which will be identified from experimental data.

By following an energy-based reasoning introduced by Gurson in the case of a porous material with a von-Mises solid phase (Gurson, 1977), it is possible to relate the viscoplastic strain rate of the clay matrix to that of the solid phase. In the present case of a Drucker-Prager solid phase, one obtains then:

$$\left(1-\varphi\right)\alpha\dot{\gamma}^{vp} = \tilde{\boldsymbol{\Sigma}} : \dot{\tilde{\mathbf{E}}}^{vp} \tag{7}$$

$\dot{\gamma}^{vp}$ denotes the rate of equivalent viscoplastic strain of the clay matrix.

The variation of porosity can be determined from the kinematical compatibility condition as follows:

$$\dot{\varphi} = \left(1-\varphi\right)\mathrm{tr}\dot{\tilde{\mathbf{E}}}^{vp} - \Omega^{-1}\int_{\Omega_m}\mathrm{tr}\dot{\boldsymbol{\varepsilon}}^{vp}\mathrm{d}\Omega \tag{8}$$

where Ω_m represents the volume of the solid phase while Ω the total volume of the unit cell of clay matrix, $\dot{\boldsymbol{\varepsilon}}^{vp}$ is the rate of viscoplastic strain in the solid phase. According to the local viscoplastic criterion for the solid phase given in (1), the viscoplastic dilation is related to the viscoplastic shear strain by $\mathrm{tr}\dot{\boldsymbol{\varepsilon}}^{vp} = 3\alpha\dot{\gamma}^{vp}$. Therefore, (8) can be rewritten as:

$$\dot{\varphi} = \left(1-\varphi\right)\left(\mathrm{tr}\dot{\tilde{\mathbf{E}}}^{vp} - 3\alpha\dot{\gamma}^{vp}\right) \tag{9}$$

From (5) and (7), with the associated flow rule, we have:

$$\dot{\gamma}^{vp} = \frac{\tilde{\boldsymbol{\Sigma}} : \dfrac{\partial f}{\partial \tilde{\boldsymbol{\Sigma}}}}{\left(1-\varphi\right)\alpha}\dot{\lambda} \tag{10}$$

Substituting (10) into (9), the variation of porosity is given by:

$$\dot{\varphi} = \left(1-\varphi\right)\left(\frac{\partial f}{\partial \tilde{\Sigma}_m} - 3\alpha\frac{\tilde{\boldsymbol{\Sigma}} : \dfrac{\partial f}{\partial \tilde{\boldsymbol{\Sigma}}}}{\left(1-\varphi\right)\alpha}\right)\dot{\lambda} \tag{11}$$

Finally, the tangent operator should be determined in view of the second step

homogenization. As mentioned above, an algorithmic tangent operator is generally defined for the determination of strain localization tensor in the viscoplastic model (Abou-Chakra Guéry, 2008). However, such an algorithmic operator is not physically based. Thus, in this study, a tangent operator derived from the plastic counterpart of constitutive model (Shen and al., 2012), seen as the asymptotic state of viscoplastic flow, is used rather than the mathematic algorithmic one. This elastoplastic operator is given by:

$$\mathbb{L}_0 = \begin{cases} \mathbb{C} & \text{if } f\left(\tilde{\boldsymbol{\Sigma}},\alpha,\varphi\right) \le 0, \\ \mathbb{C} - \dfrac{\mathbb{C}:\dfrac{\partial f}{\partial \tilde{\boldsymbol{\Sigma}}} \otimes \dfrac{\partial f}{\partial \tilde{\boldsymbol{\Sigma}}}:\mathbb{C}}{H^a} & \text{if } f\left(\tilde{\boldsymbol{\Sigma}},\alpha,\varphi\right) > 0. \end{cases} \tag{12}$$

with $H^a = \dfrac{\partial f}{\partial \tilde{\boldsymbol{\Sigma}}}:\mathbb{C}:\dfrac{\partial f}{\partial \tilde{\boldsymbol{\Sigma}}} - \dfrac{\partial f}{\partial \tilde{\boldsymbol{\Sigma}}}(1-\varphi)\left[\dfrac{\partial f}{\partial \tilde{\Sigma}_m} - 3\alpha\dfrac{\tilde{\boldsymbol{\Sigma}}:\dfrac{\partial f}{\partial \tilde{\boldsymbol{\Sigma}}}}{(1-\varphi)\alpha}\right] - \dfrac{\partial f}{\partial \alpha}\dfrac{\partial \alpha}{\partial \gamma^{vp}}\dfrac{\tilde{\boldsymbol{\Sigma}}:\dfrac{\partial f}{\partial \tilde{\boldsymbol{\Sigma}}}}{(1-\varphi)\alpha}$.

It's worth noting that the tangent operator $\mathbb{L}_0$ derived from the associated viscoplastic flow is an isotropic tensor. It means that, for the case of isotropic clay matrix and spherical inclusions, the Eshelby tensor is also isotropic and can be easily evaluated by the following analytical expression:

$$\mathbb{S}^0 = 3\hat{k}_s\mathbb{J} + 2\hat{\mu}_s\mathbb{K}$$

with $\hat{k}_s = \dfrac{k_t}{3k_t + 4\mu_t}$ and $\hat{\mu}_s = \dfrac{3\left(k_t + 2\mu_t\right)}{5\left(3k_t + 4\mu_t\right)}$.

k_t and μ_t are respectively tangent elastoplastic moduli of the clay matrix.

4.1.2 Numeric implementation

The proposed micromechanical model is implemented in a standard finite element code (Abaqus) as a UMAT subroutine. We present here the numerical scheme for the local integration of the model at each Gauss point.

The loading path is divided into a limit number of steps. At the step $n+1$, the material point of argillite at the macroscopic scale is subjected to a macroscopic strain $\mathbf{E}_{n+1} = \mathbf{E}_n + \Delta\mathbf{E}_{n+1}$, the strain at the step (n) is known and the strain increment $\Delta\mathbf{E}_{n+1}$ is given. The problem to be solved here is to find the corresponding macroscopic stress state at the end of loading step by using the homogenization method presented in the chapter 2 concerning the Hill's incremental method. The

following numerical scheme is adopted:

5. At time t_{n+1}, input data : $\mathbf{E}_n$, $\Delta\mathbf{E}_{n+1}$, Δt_{n+1}

   phase (0) clay matrix: $\left(\tilde{\mathbf{E}}_0\right)_n$, $\left(\tilde{\mathbf{E}}_0^{vp}\right)_n$, φ_n, γ_n^{vp}

   phase (1) calcite grains: $\left(\boldsymbol{\varepsilon}_1\right)_n$

   phase (2) quartz grains: $\left(\boldsymbol{\varepsilon}_2\right)_n$

6. Initial local strain increments in the phase (1) and phase (2) are configured as:

$$\left(\Delta\boldsymbol{\varepsilon}_1\right)_{n+1}^i := \Delta\mathbf{E}_{n+1}, \qquad \left(\Delta\boldsymbol{\varepsilon}_2\right)_{n+1}^i := \Delta\mathbf{E}_{n+1}$$

3. Then, the average local strain increment in the clay matrix (phase (0)) is given by:

$$\left(\Delta\tilde{\mathbf{E}}_0\right)_{n+1}^i := \frac{\Delta\mathbf{E}_{n+1} - f_1\left(\Delta\boldsymbol{\varepsilon}_1\right)_{n+1}^i - f_2\left(\Delta\boldsymbol{\varepsilon}_2\right)_{n+1}^i}{1 - f_1 - f_2}$$

where f_1 and f_2 are volume fractions for the phase (1) and phase (2), respectively.

6. At the iterate i, for the clay matrix, the values of $\left(\Delta\tilde{\mathbf{E}}_0\right)_{n+1}^i$, $\left(\tilde{\mathbf{E}}_0\right)_n$, $\left(\tilde{\mathbf{E}}_0^{vp}\right)_n$, φ_n and γ_n^{vp} are known, one can in turn compute: $\left(\tilde{\mathbf{E}}_0\right)_{n+1}^i$, , $\left(\gamma_{n+1}^{vp}\right)^i$, φ_{n+1}^i, $\left(\tilde{\mathbf{E}}_0^{vp}\right)_{n+1}^i$ and L_0. For the phase (1) and phase (2), the local elastic stiffness tensor L_1 and L_2 are invariable in each incremental step because they are regarded as the linear elastic phases.

7. The Hill tensor is explicitly evaluated using the isotropic elastoplastic tangent operator ($\mathbb{L}_0$) given in (12).

6. According to the Mori-Tanaka scheme, the localization tensors of the 3 phases can be determined as: $\mathbb{A}_0^i$, $\mathbb{A}_1^i$ and $\mathbb{A}_2^i$.

7. Check the compatibility of local strains between two iterates for the phase (1) and phase (2) and compute the error $\mathbf{R}$:

$$\mathbf{R}_1^i := \mathbb{A}_1^i : \Delta\mathbf{E} - \Delta\boldsymbol{\varepsilon}_1^i$$

$$\mathbf{R}_2^i := \mathbb{A}_2^i : \Delta\mathbf{E} - \Delta\boldsymbol{\varepsilon}_2^i$$

If $\left\|\mathbf{R}_1^i\right\| < tolerance\ 1$ and $\left\|\mathbf{R}_2^i\right\| < tolerance\ 2$, the compatibility is reached. Else,

an additional iterate is required until the two above convergence criteria are attained and in that situation, one sets:

$$\left(\Delta\boldsymbol{\varepsilon}_1\right)_{n+1}^{i+1} = \left(\Delta\boldsymbol{\varepsilon}_1\right)_{n+1}^{i} + \mathbf{R}_1^i$$

$$\left(\Delta\boldsymbol{\varepsilon}_2\right)_{n+1}^{i+1} = \left(\Delta\boldsymbol{\varepsilon}_2\right)_{n+1}^{i} + \mathbf{R}_2^i$$

and return to the step 3.

9. For the phase(0), $\Delta\tilde{\mathbf{E}}_0^{vp}$ is known, the increment of macroscopic viscoplastic strain is given by: $\Delta\mathbf{E}_{n+1}^{vp} = f_0\Delta\tilde{\mathbf{E}}_0^{vp}$

9. The increment of macroscopic stress tensor can be calculated as:

$$\Delta\boldsymbol{\Sigma}_{n+1} = \mathbb{C}^{\text{hom}} : \left(\Delta\mathbf{E}_{n+1} - \Delta\mathbf{E}_{n+1}^{vp}\right)$$

$\mathbb{C}^{\text{hom}}$ is the macroscopic elastic stiffness tensor of the argillite given in Chapter 2.

4.1.3 Experimental validation of micro-macro model with associated flow rule

The proposed micro-macro model is now used in the simulation of some laboratory tests performed on the Callovo-Oxfordian argillite. The local parameters are identified based on typical laboratory tests. Indeed, no local measurements (strains and stresses) inside constituent phases are available for the COX argillite. Direct identification of local parameters is not possible. An alternative indirect method is used and based on an optimization procedure. Given the elastic parameters of calcite and quartz grains collected from literature, the key point is the determination of parameters for the clay matrix. For a given mineralogical composition, the parameters of the clay matrix are obtained from an iterative optimization procedure by the simulation of representative triaxial compression tests and creep tests. Then the obtained values are used in the simulations of other tests performed on argillite samples with different mineralogical compositions in order to check their validity. Typical values of parameters are illustrated in Table 1. The typical numerical results for uniaxial and triaxial compression are shown in Fig. 2. One can see that though the micro-macro model correctly predicts axial strains of the argillite in uniaxial compression and triaxial compression tests, it fails to reproduce lateral and volumetric strains. In order to improve the quality of numerical results, a non-associated flow rule is then needed in the clay matrix.

Table 1 Parameters of micro-macro model with associated flow rule

	Phase (0) Clay matrix	Phase (1) Calcite grain	Phase (2) Quartz grain
Elastic parameters	$E_0 = 5GPa$ $\nu_0 = 0.3$	$E_1 = 95GPa$ $\nu_1 = 0.27$	$E_2 = 100GPa$ $\nu_2 = 0.06$
Viscoplastic parameters	$\alpha_0^{vp} = 0.05$ $\alpha_m^{vp} = 0.88$ $c_{vp} = 14$ $b = 150$ $m = 3$ $\eta = 5\times10^7$		
Initial porosity	$f_0 = 0.25$		

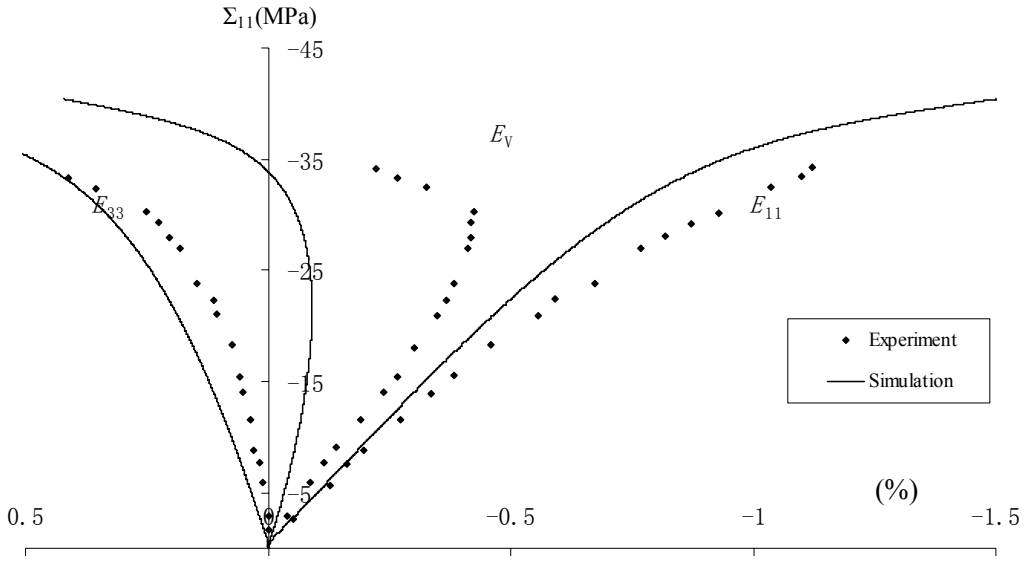

(a) Depth 466.8*m*, f_0=51%, f_1=26%, f_2=23%

Uniaxial compression test

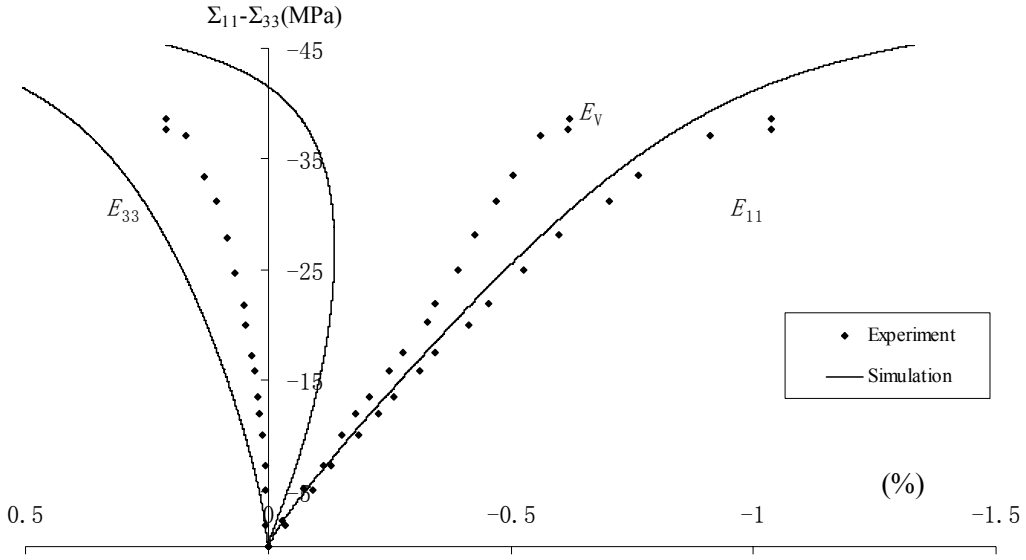

(b) Depth 451.8*m*, f_0=49%, f_1=19%, f_2=32%

Triaxial compression test, $\sigma_c = 5MPa$

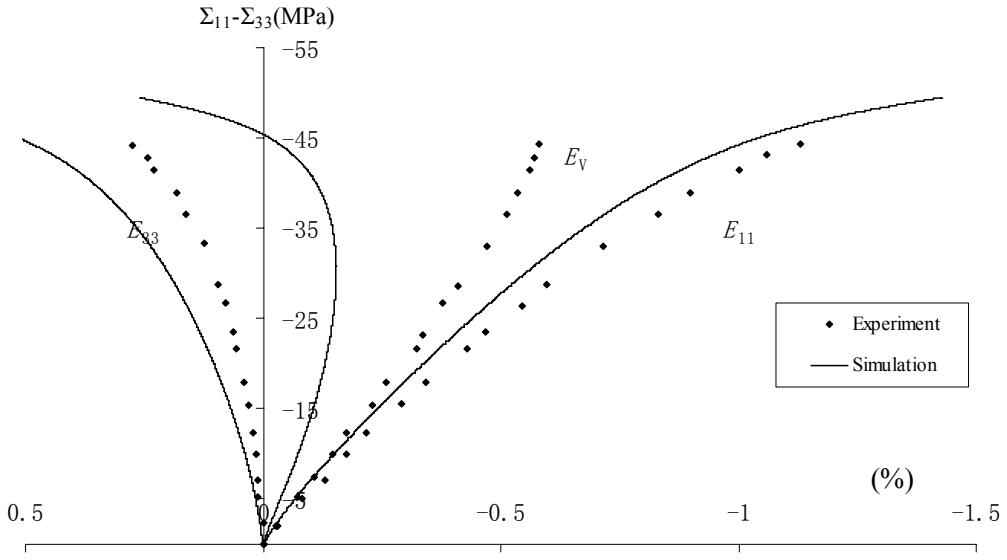

(c) Depth 451.4*m*, f_0=47%, f_1=31%, f_2=22%

Triaxial compression test, $\sigma_c = 10MPa$

Fig.2 Comparison between numerical results and experimental data in uniaxial and triaxial compression tests

4.2 Formulation of a non-associated micro-macro model

In order to improve the predictive performance of the micro-macro model, a non-associated viscoplastic model is proposed for the clay matrix. For this purpose,

based on the macroscopic yield function (2) issued from the homogenization of the porous clay matrix, the following non-associated viscoplastic potential is defined:

$$G\left(\tilde{\boldsymbol{\Sigma}},\alpha,\beta,\varphi\right)=\frac{1+2\varphi/3}{\alpha^2}\tilde{Q}^2+\left(\frac{3\varphi}{2\alpha\beta}-1\right)\tilde{\Sigma}_m^2+2\left(1-\varphi\right)c_{vp}\tilde{\Sigma}_m \tag{13}$$

The function $\beta(\gamma^{vp})$ is here introduced in order to better control the volumetric strain of the clay matrix. In order to describe the compressibility-dilatancy transition largely observed in clayey rocks, it is assumed that the function $\beta(\gamma^{vp})$ evolves from an initial value β_0^{vp} to an asymptotic one β_m^{vp}:

$$\beta\left(\gamma^{vp}\right)=\left[\beta_m^{vp}-\left(\beta_m^{vp}-\beta_0^{vp}\right)e^{-b'\gamma^{vp}}\right] \tag{14}$$

The parameter b' controls the compressibility-dilatancy transition of the clay matrix. Hence, the viscoplastic flow rule of the clay matrix writes:

$$\dot{\tilde{\mathbf{E}}}^{vp}=\dot{\lambda}\frac{\partial G}{\partial\tilde{\boldsymbol{\Sigma}}}\left(\tilde{\boldsymbol{\Sigma}},\alpha,\beta,\varphi\right) \tag{15}$$

The viscoplastic multiplier $\dot{\lambda}$ is unchanged as given by (6).

Using this non-associated flow rule and (7), the rate of equivalent viscoplastic strain of the clay matrix is given by:

$$\dot{\gamma}^{vp}=\frac{\tilde{\boldsymbol{\Sigma}}:\dfrac{\partial G}{\partial\tilde{\boldsymbol{\Sigma}}}}{\left(1-\varphi\right)\alpha c_{vp}+\left(\beta-\alpha\right)\tilde{\Sigma}_m}\dot{\lambda}$$

The evolution of porosity is determined by:

$$\dot{\varphi}=\left(1-\varphi\right)\left(\frac{\partial G}{\partial\tilde{\Sigma}_m}-3\beta\frac{\tilde{\boldsymbol{\Sigma}}:\dfrac{\partial G}{\partial\tilde{\boldsymbol{\Sigma}}}}{\left(1-\varphi\right)\alpha c_{vp}+\left(\beta-\alpha\right)\tilde{\Sigma}_m}\right)\dot{\lambda}$$

Similarly to the associated model, an asymptotic elastoplastic tangent operator is defined for the non-associated viscoplastic model (Shen and al., 2012) as follows:

$$\mathbb{L}_0=\begin{cases}\mathbb{C} & \text{if } f\left(\tilde{\boldsymbol{\Sigma}},\alpha,\varphi\right)\le 0,\\ \mathbb{C}-\dfrac{\mathbb{C}:\dfrac{\partial f}{\partial\tilde{\boldsymbol{\Sigma}}}\otimes\dfrac{\partial G}{\partial\tilde{\boldsymbol{\Sigma}}}:\mathbb{C}}{H^n} & \text{if } f\left(\tilde{\boldsymbol{\Sigma}},\alpha,\varphi\right)>0.\end{cases} \tag{16}$$

With

$$H^n = \frac{\partial f}{\partial \tilde{\boldsymbol{\Sigma}}} : \mathbb{C} : \frac{\partial G}{\partial \tilde{\boldsymbol{\Sigma}}} - \frac{\partial f}{\partial \varphi}(1-\varphi)\left[\frac{\partial G}{\partial \tilde{\Sigma}_m} - \beta \frac{\tilde{\boldsymbol{\Sigma}} : \frac{\partial G}{\partial \tilde{\boldsymbol{\Sigma}}}}{(1-\varphi)\alpha c_{vp} + (\beta-\alpha)\tilde{\Sigma}_m}\right]$$
$$- \frac{\partial f}{\partial \alpha}\frac{\partial \alpha}{\partial \gamma^{vp}} \frac{\tilde{\boldsymbol{\Sigma}} : \frac{\partial G}{\partial \tilde{\boldsymbol{\Sigma}}}}{(1-\varphi)\alpha c_{vp} + (\beta-\alpha)\tilde{\Sigma}_m}$$

Note that as a difference with the associated model, the tangent operator $\mathbb{L}_0$ given by (16) is now anisotropic in nature. Therefore, the Eshelby tensor should be evaluated by the numerical procedure mentioned in Chapter 2. Comparing the tangent operators derived respectively from the associated and non-associated flow rules, the latter is more complex to compute the Eshelby tensor due to its anisotropic tangent operator of the clay matrix.

4.2.1 Experimental validation of the non-associated micro-macro model

4.2.1.1 Uniaxial and triaxial compression tests

Following the same optimization procedure as that used for the associated model, the values of parameters of the non-associated model are determined and given in Table 2. Fig.3 shows the comparison between the numerical results and experimental data for uniaxial and triaxial compression tests performed on argillites samples with different mineralogical compositions. One can see a good agreement both for axial and volumetric strains. The transition from volumetric contractance to dilatancy following the deviatoric stress increase is correctly described. The evolution of porosity in clay matrix is given by Fig.4. As mentioned in the work by Shen and al. (2012), the variation of porosity remains quite small. However, this does not mean that the influence of porosity is negligible. Indeed, the macroscopic response of argillite is very sensitive to the initial value of porosity.

Table 2 Typical parameters of micro-macro model with non-associated flow rule

	Phase (0) Clay matrix	Phase (1) Calcite grain	Phase (2) Quartz grain
Elastic parameters	$E_0 = 5GPa$ $\nu_0 = 0.3$	$E_1 = 95GPa$ $\nu_1 = 0.27$	$E_2 = 100GPa$ $\nu_2 = 0.06$
Viscoplastic parameters	$\alpha_0^{vp} = 0.05$ $\alpha_m^{vp} = 0.88$ $b = 150$ $\beta_0^{vp} = 0.001$ $\beta_m^{vp} = 0.6$ $b^{'} = 30$ $c_{vp} = 14$ $m = 3$ $\eta = 5 \times 10^7$		
Initial porosity	$f_0 = 0.25$		

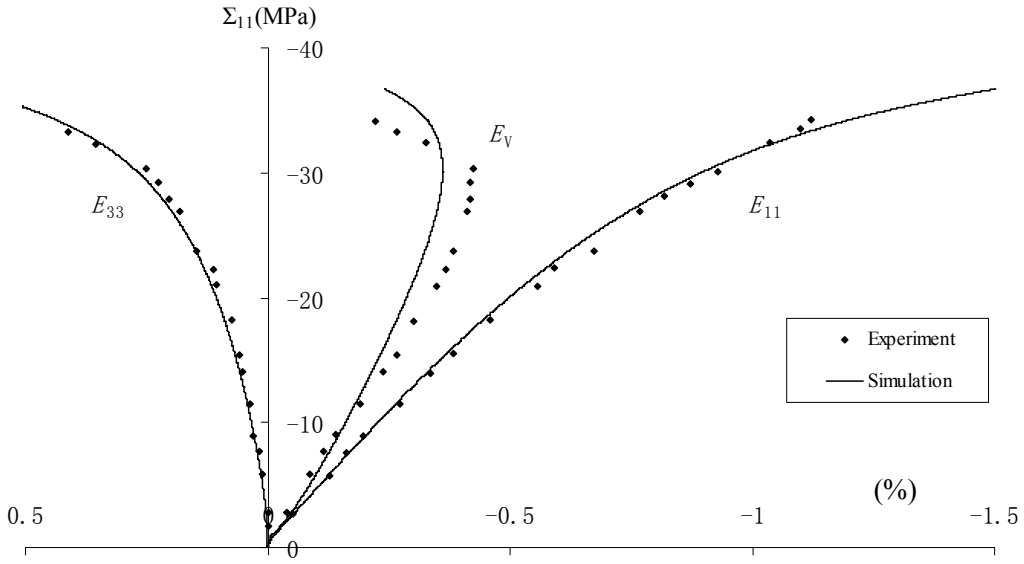

(a) Depth 466.8*m*, f_0=51%, f_1=26%, f_2=23%

Uniaxial compression test

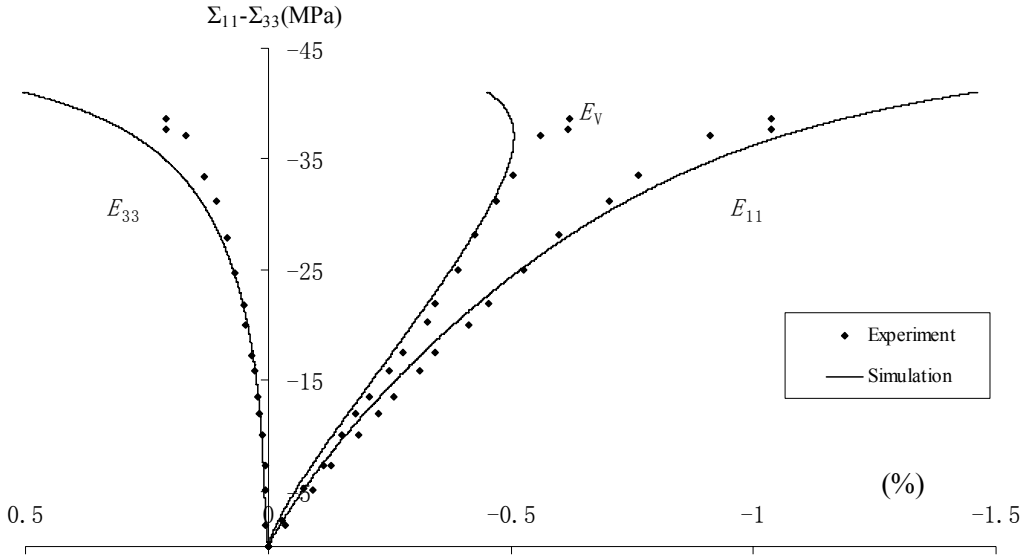

(b) Depth 451.8*m*, f_0=49%, f_1=19%, f_2=32%

Triaxial compression test, $\sigma_c = 5MPa$

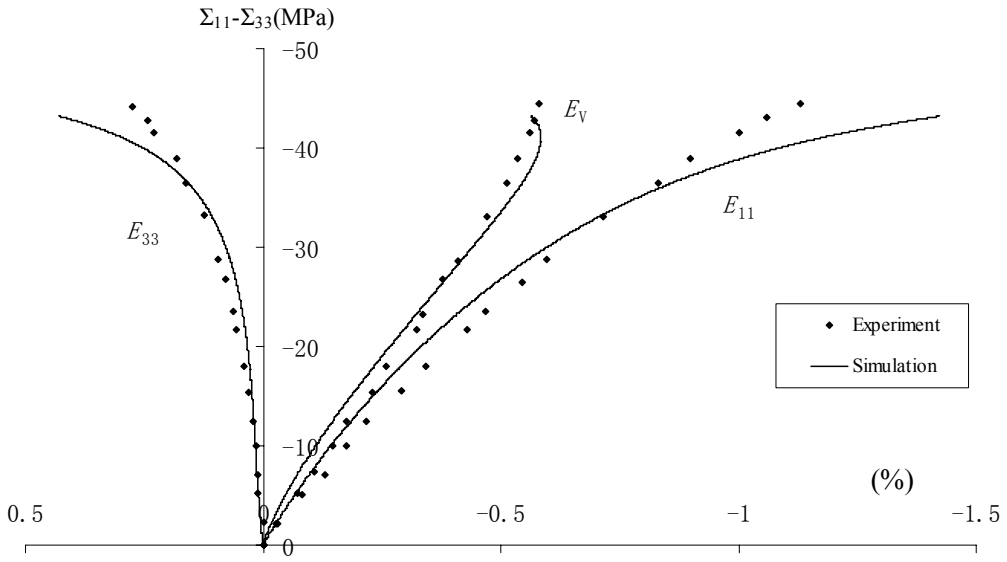

(c) Depth 451.4*m*, f_0=47%, f_1=31%, f_2=22%

Triaxial compression test, $\sigma_c = 10MPa$

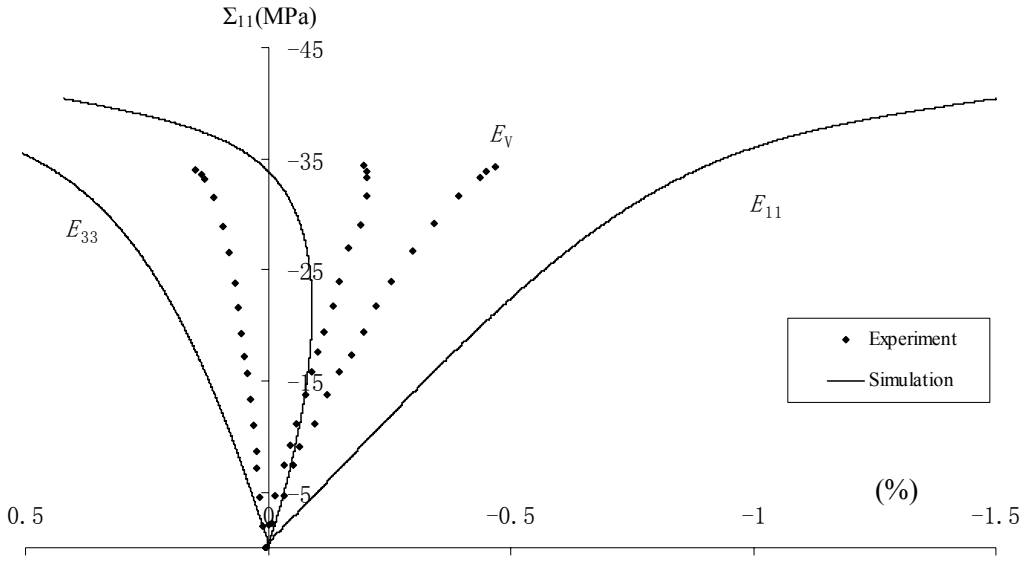

(d) Depth 468.9*m*, f_0=34%, f_1=53%, f_2=13%

Uniaxial compression test

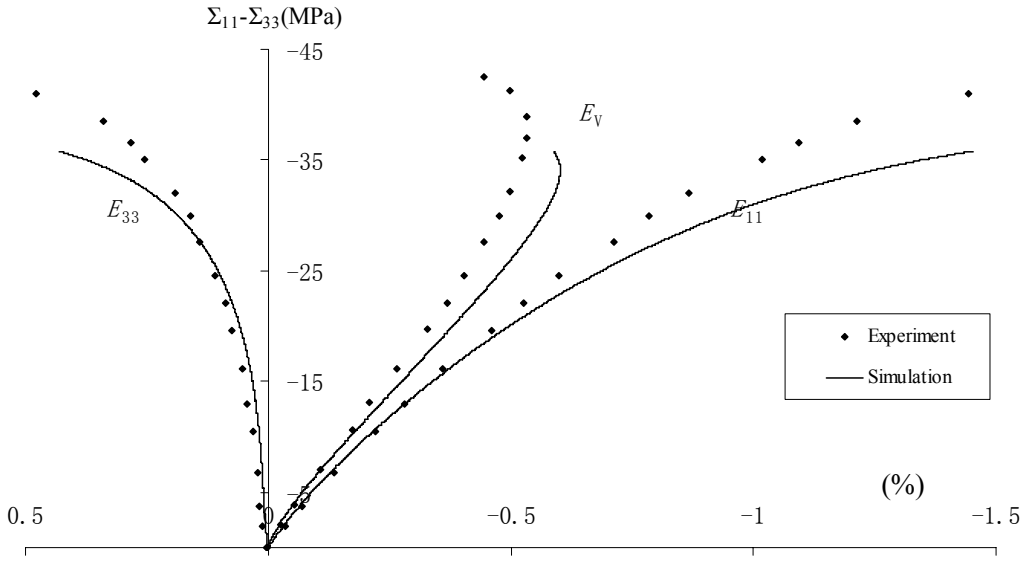

(e) Depth 482.2*m*, f_0=60%, f_1=26%, f_2=14%

Triaxial compression test, $\sigma_c = 5MPa$

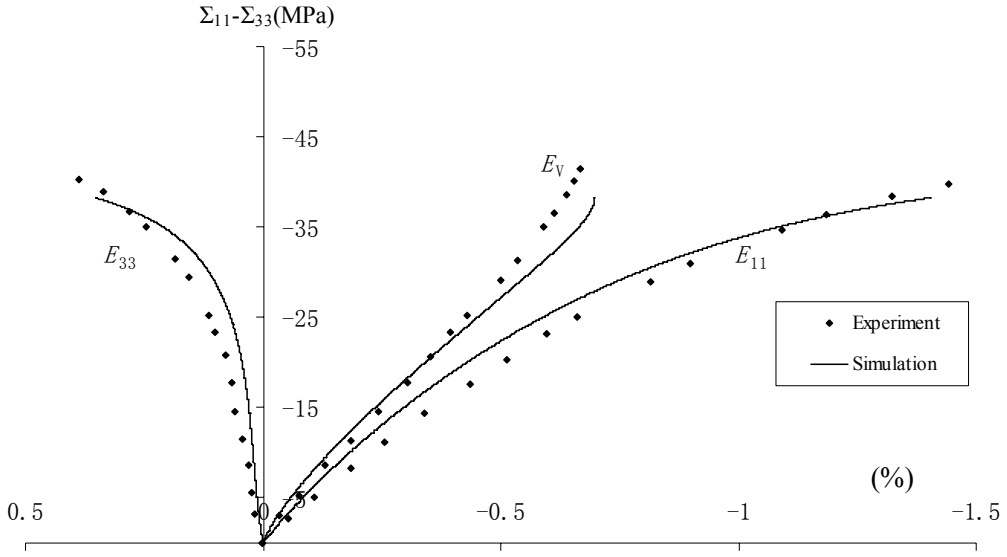

(f) Depth 482.2*m*, f_0=60%, f_1=26%, f_2=14%

Triaxial compression test, $\sigma_c = 10MPa$

Fig.3 Comparison between numerical results and laboratory tests

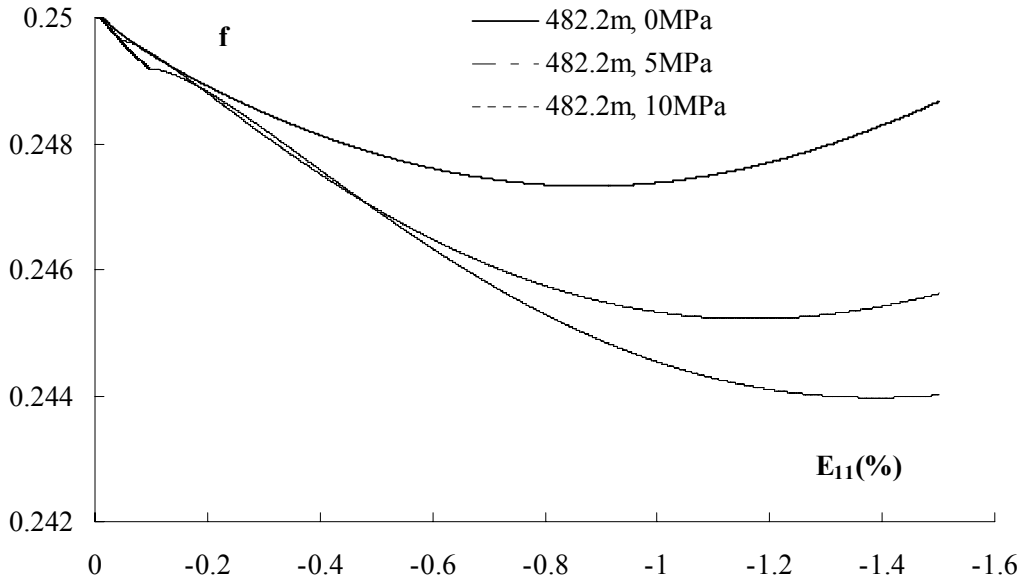

Fig.4 Evolution of porosity in clay matrix with axial strain

4.2.1.2 Uniaxial and triaxial creep tests

In this section we present modeling of time-dependent response of argillite by using the proposed micro-macro model. Again, the values of parameter related to time-dependent responses are identified from creep test by an iterative optimization

procedure and typical values are shown in Table 3. Comparisons between numerical results and experimental data are presented in Fig. 5 for various loading conditions and mineralogical compositions. One can see that there is generally a good agreement between experimental data and numerical results issued from the proposed model; this one seems to be able to correctly reproduce creep strain of argillites.

Table 3: Parameters for the creep tests with non-associated flow rule

	Phase (0) Clay matrix	Phase (1) Calcite grain	Phase (2) Quartz grain
Elastic parameters	$E_0 = 5GPa$ $\nu_0 = 0.3$	$E_1 = 95GPa$ $\nu_1 = 0.27$	$E_2 = 100GPa$ $\nu_2 = 0.06$
Viscoplastic parameters	$\alpha_0^{vp} = 0.05$ $\alpha_m^{vp} = 0.88$ $b = 150$ $\beta_0^{vp} = 0.001$ $\beta_m^{vp} = 0.6$ $b^{'} = 30$ $c_{vp} = 14$ $m = 0.3$ $\eta = 5 \times 10^8$		
Initial porosity	$f_0 = 0.25$		

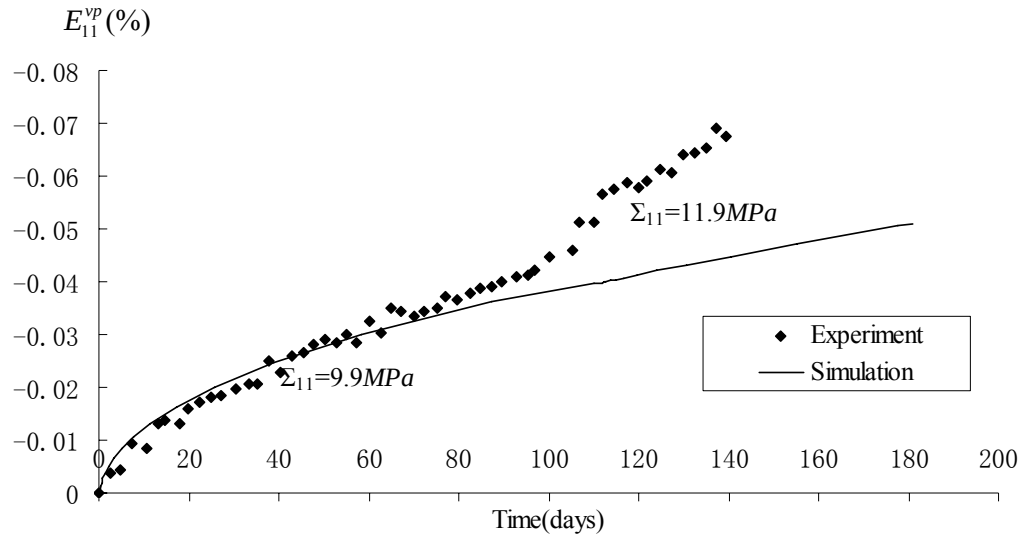

(a) Depth 434.4*m*, f_0=30.4%, f_1=36.2%, f_2=33.4% (EST 205 GII-05481-01)

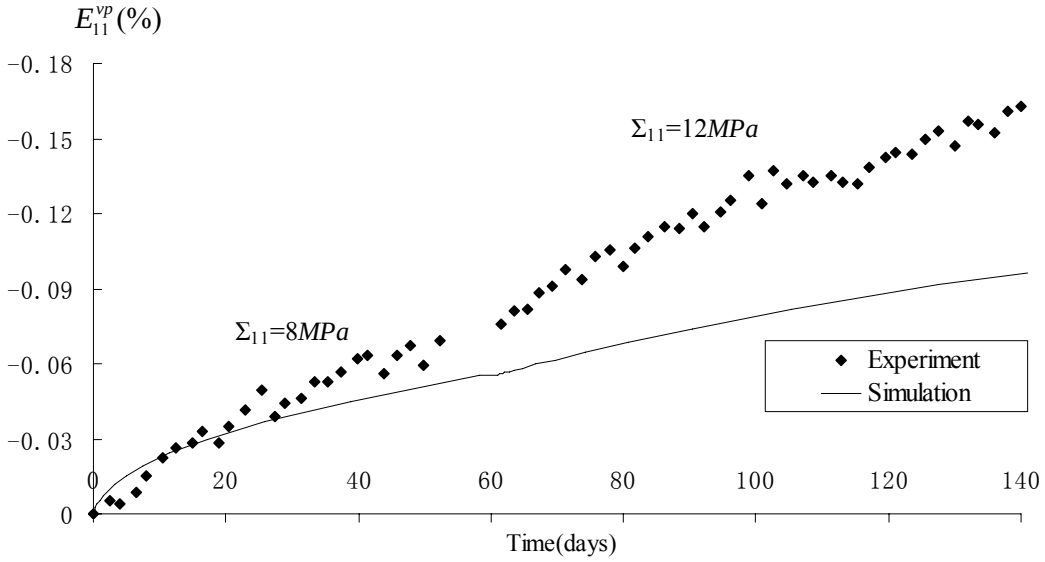

(b) Depth 484.2*m*, f_0=56.2%, f_1=20.4%, f_2=23.4% (EST 205 GIV-05671-03)

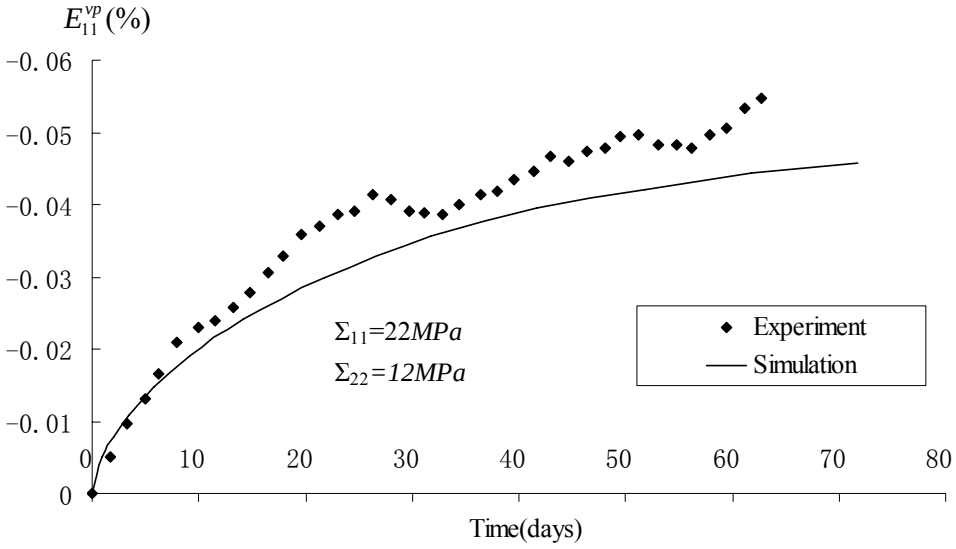

(c) Depth 492.1*m*, f_0=56.9%, f_1=21.9%, f_2=21.2% (EST 205 5698-5)

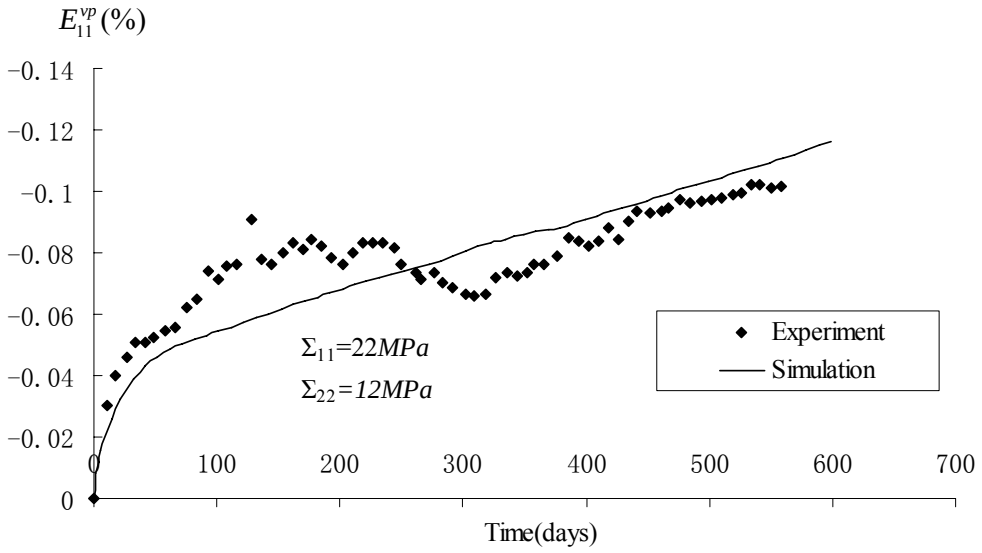

(d) Depth 497.8*m*, f_0=61%, f_1=21.6%, f_2=17.4% (EST 205 5721)

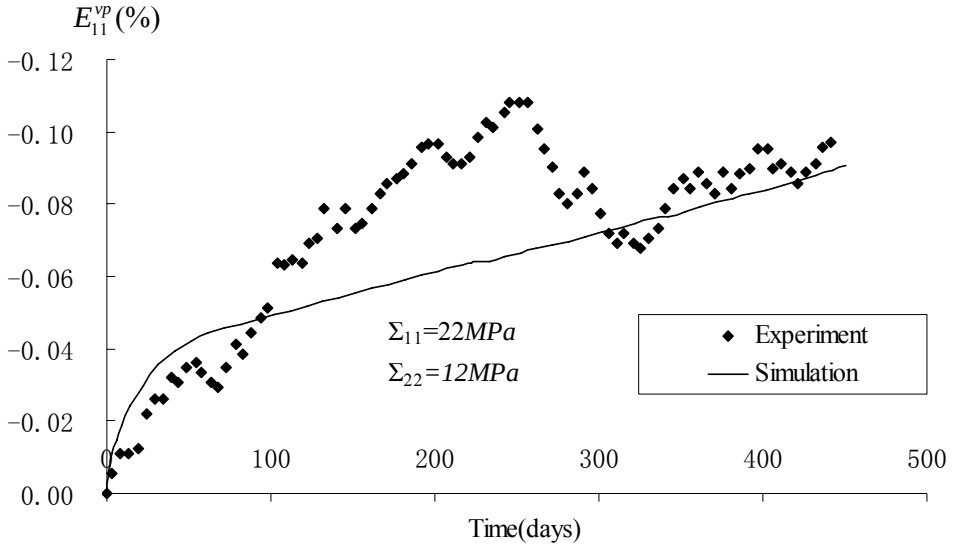

(e) Depth 491.8*m*, f_0=57%, f_1=21.7%, f_2=21.3% (EST 205 5698-5)

Fig.5 Comparison between the simulation and laboratory test

4.3 Conclusion

In this chapter, a two scale micro-macro model is proposed in the framework of nonlinear homogenization methods for the description of time-dependent behavior of a cohesive frictional geomaterial, the Callovo-Oxfordian argillite. In the context of Hill's incremental approach for viscoplastic materials, an algorithmic tangent operator is generally defined for the determination of incremental Eshelby tensor. However, such an algorithmic operator is not physically based. In this chapter, a tangent operator derived from the elastoplastic counterpart of constitutive model, seen as the asymptotic state of viscoplastic flow, is used rather than the algorithmic one. An associated viscoplastic flow rule is first considered for the clay matrix. The numerical results have shown that, though the micro-macro model correctly predicts axial strains of the argillite in uniaxial and triaxial compression tests, it fails to reproduce lateral and volumetric strains. In order to improve the quality of numerical results, a non-associated flow rule is then adopted for the clay matrix. The performance of the proposed model is verified through comparisons between numerical results and experimental data for both triaxial compression and creep tests, performed on samples with different mineralogical compositions. The comparisons show that the non-associated model is able to describe the main features of instantaneous and time-dependent mechanical behaviors of the Callovo-Oxfordian argillites.

Chapter 5
Adaptation and application of the incremental variational principles to geomaterials

Résumé du chapitre

En raison de l'hypothèse forte d'une distribution homogène du champ de déformation dans chaque phase, il ressort des travaux de [Doghri et Ouaar, 2003], [Chaboche et Kanouté, 2003] et [Abou-Chakra et al. 2007] que l'approche de Hill conduit à une réponse trop rigide du comportement. Cette observation pourrait s'expliquer par l'accumulation d'erreurs à chaque étape d'itération due à l'absence de prise en compte de l'hétérogénéité du champ de déformation locale. Pour cette raison, une nouvelle méthode basée sur les principes variationnels incrémentales [Lahellec et Suquet, 2007] en mesure d'examiner l'hétérogénéité des champs locaux est étendue à la prédiction du comportement des géomatériaux et plus particulièrement des argilites. Lors de l'utilisation d'un régime de discrétisation implicite du temps, les équations d'évolution décrivant le comportement des phases peuvent être réduites à la minimisation d'une fonction incrémentale d'énergie. Ce problème de minimisation est rigoureusement équivalent à un problème thermoélastique linéaire fonction d'un champ des déformations hétérogènes.

Par rapport à des matériaux métalliques ou composites, la pression de confinement joue un rôle important dans le comportement mécanique des géomatériaux. Par ailleurs, comme indiqué dans les chapitres précédents, la transition de contractance-dilatance de la déformation volumique est un autre aspect important à prendre en compte. Ainsi, le modèle variationnel incrémental initialement proposé par Lahellec et Suquet (2007) sera adapté aux géomatériaux afin de prendre en compte ces deux aspects. La performance du modèle proposé sera vérifiée en comparant les résultats numériques et données expérimentales.

In most micro-macro models, the COX argillite is generally considered as a two or three phase composite: the clay matrix and the mineral inclusions (calcite and quartz grains). The clay matrix is described by a viscoplastic behavior while the mineral inclusions are considered as linear elastic medium. In order to make a clearly explanation as to the physical mechanisms of creep deformation and furthermore to take into account influences of material microstructure on time-dependent behavior, various micromechanical viscoplastic models are used to describe the time-dependent behavior of composites. Based on Hill's incremental method, Abou-Chakra Guéry [Abou-Chakra Guéry et al., 2008] proposed a three phase composite model and Jiang [Jiang et al., 2009] proposed a two phase micromechanical model. Due to the assumption of homogeneous distribution of local strain field in each phase, Hill's approach generally leads to a too stiff response due to the accumulation of errors at each iteration step caused by the negligence to adequately take account of the heterogeneity of local fields. A suitable "isotropization procedure" is thus necessary to improve the performance of Hill type incremental homogenization methods. Nevertheless, such correction techniques as "isotropization procedure" don't have any physical background. For this reason, we need a "more rigorous" method which is able to consider the heterogeneity of local fields.

Lahellec and Suquet [Lahellec and Suquet 2007] proposed a new method based on incremental variational principles. Upon use of an implicit time-discretization scheme, the evolution equations describing the constitutive behavior of the phases can be reduced to the minimization of an incremental energy function. This minimization problem is rigorously equivalent to a nonlinear thermoelastic problem with a transformation strain which is a heterogeneous field. Comparisons with full-field simulation show that this model is quite satisfactory. This chapter focus on extending this model to geomaterials, more exactly, the Callovo-Oxfordian argillites, considering the specific properties of geomaterials such as compressibility- dilatancy transition and influence of confining pressure. An isotropic and kinematic hardening effect is considered as well for the more general cases.

5.1 Variational problem

5.1.1 Two thermodynamic potentials

In the framework of viscoplasticity, the composite materials are considered as a combination of the individual constituents exhibiting a dissipative behavior which can be modeled by two thermodynamic potentials, a free-energy w and a dissipation potential φ which are convex functions of the state variables and their

time-derivative (Lahellec and Suquet, 2006). The driving forces associated with the state variables are:

$$\boldsymbol{\sigma} = \frac{\partial w}{\partial \boldsymbol{\varepsilon}}\left(\boldsymbol{\varepsilon}, \boldsymbol{\varepsilon}^{vp}\right) \tag{1}$$

$$F^{vp} = -\frac{\partial w}{\partial \boldsymbol{\varepsilon}^{vp}}\left(\boldsymbol{\varepsilon}, \boldsymbol{\varepsilon}^{vp}\right) = \frac{\partial \varphi}{\partial \dot{\boldsymbol{\varepsilon}}^{vp}}\left(\dot{\boldsymbol{\varepsilon}}^{vp}\right) \tag{2}$$

Where $\boldsymbol{\varepsilon}$ is the infinitesimal strain, $\boldsymbol{\varepsilon}^{vp}$ is the viscoplastic strain.

According to the relations (1) and (2), the constitutive relations of the materials can be written as:

$$\boldsymbol{\sigma} = \frac{\partial w}{\partial \boldsymbol{\varepsilon}}\left(\boldsymbol{\varepsilon}, \boldsymbol{\varepsilon}^{vp}\right), \quad \frac{\partial w}{\partial \boldsymbol{\varepsilon}^{vp}}\left(\boldsymbol{\varepsilon}, \boldsymbol{\varepsilon}^{vp}\right) + \frac{\partial \varphi}{\partial \dot{\boldsymbol{\varepsilon}}^{vp}}\left(\dot{\boldsymbol{\varepsilon}}^{vp}\right) = 0 \tag{3}$$

Most classical nonlinear viscoelastic or elasto-viscoplastic models can be formulated in this general framework through appropriate choices of the potentials w and φ (Germain and al., 1983; Lemaitre and Chaboche, 1994).

5.1.2 Incremental variational principle

Based on the works of Mialon (1986) and Ortiz and Stainier (1999), the time derivative in (3) can be approximated by a difference quotient after use of an implicit Euler-scheme. The time interval of study [0, T] is discretized into time steps $t_0 = 0, t_1, t_2, \cdots, t_n, t_{n+1}, \cdots, t_N = T$, the time step between t_n and t_{n+1} is denoted by Δt which depends on n. The rate of plastic strain $\dot{\boldsymbol{\varepsilon}}^{vp}$ at time t_{n+1} is approximated by the finite difference $\left(\boldsymbol{\varepsilon}_{n+1}^{vp} - \boldsymbol{\varepsilon}_{n}^{vp}\right)/\Delta t$. By means of this time-discretization procedure, the system (3) is replaced by the discretized system as follow:

$$\boldsymbol{\sigma}_{n+1} = \frac{\partial w}{\partial \boldsymbol{\varepsilon}}\left(\boldsymbol{\varepsilon}_{n+1}, \boldsymbol{\varepsilon}_{n+1}^{vp}\right), \quad \frac{\partial w}{\partial \boldsymbol{\varepsilon}^{vp}}\left(\boldsymbol{\varepsilon}_{n+1}, \boldsymbol{\varepsilon}_{n+1}^{vp}\right) + \frac{\partial \varphi}{\partial \dot{\boldsymbol{\varepsilon}}^{vp}}\left(\frac{\boldsymbol{\varepsilon}_{n+1}^{vp} - \boldsymbol{\varepsilon}_{n}^{vp}}{\Delta t}\right) = 0 \tag{4}$$

At the end of n^{th} step, the fields $\boldsymbol{\sigma}_n$, $\boldsymbol{\varepsilon}_n$ and $\boldsymbol{\varepsilon}_n^{vp}$ are known, the unknowns $\boldsymbol{\sigma}_{n+1}$, $\boldsymbol{\varepsilon}_{n+1}$ and $\boldsymbol{\varepsilon}_{n+1}^{vp}$ at time t_{n+1} are solved via the discretized system (4).

The equations in (4) are the Euler-Lagrange equations for the following variational problem:

$$\underset{\boldsymbol{\varepsilon}^{vp}}{\mathrm{Inf}} < J\left(\boldsymbol{\varepsilon}, \boldsymbol{\varepsilon}^{vp}\right) > \tag{5}$$

Where the increment potential J reads as:

$$J\left(\boldsymbol{\varepsilon}, \boldsymbol{\varepsilon}^{vp}\right) = w\left(\boldsymbol{\varepsilon}, \boldsymbol{\varepsilon}^{vp}\right) + \Delta t \varphi\left(\frac{\boldsymbol{\varepsilon}^{vp} - \boldsymbol{\varepsilon}_n^{vp}}{\Delta t}\right) \tag{6}$$

5.1.3 Condensed incremental potential

The following potential is defined:

$$w_\Delta\left(\boldsymbol{\varepsilon}\right) = \underset{\boldsymbol{\varepsilon}^{vp}}{\mathrm{Inf}}\ J\left(\boldsymbol{\varepsilon}, \boldsymbol{\varepsilon}^{vp}\right) \tag{7}$$

Note that the derivative of w_Δ with respect to $\boldsymbol{\varepsilon}$ reads as:

$$\frac{\partial w_\Delta}{\partial \boldsymbol{\varepsilon}}\left(\boldsymbol{\varepsilon}\right) = \frac{\partial J}{\partial \boldsymbol{\varepsilon}}\left(\boldsymbol{\varepsilon}, \boldsymbol{\varepsilon}^{vp}\right) + \frac{\partial J}{\partial \boldsymbol{\varepsilon}^{vp}}\left(\boldsymbol{\varepsilon}, \boldsymbol{\varepsilon}^{vp}\right) : \frac{\partial \boldsymbol{\varepsilon}^{vp}}{\partial \boldsymbol{\varepsilon}} \tag{8}$$

where $\boldsymbol{\varepsilon}^{vp}$ is solved through the stationary problem in (5). For this reason, the last term in (8) vanishes by the stationarity of J with respect to $\boldsymbol{\varepsilon}^{vp}$. We can rewrite the above differential equation as:

$$\frac{\partial w_\Delta}{\partial \boldsymbol{\varepsilon}}\left(\boldsymbol{\varepsilon}\right) = \frac{\partial J}{\partial \boldsymbol{\varepsilon}}\left(\boldsymbol{\varepsilon}, \boldsymbol{\varepsilon}^{vp}\right) = \frac{\partial w}{\partial \boldsymbol{\varepsilon}}\left(\boldsymbol{\varepsilon}, \boldsymbol{\varepsilon}^{vp}\right) \tag{9}$$

Owing to the equation (9), we obtain the remarkable result which provides a relation between the stress and a single potential:

$$\boldsymbol{\sigma}_{n+1} = \frac{\partial w_\Delta}{\partial \boldsymbol{\varepsilon}}\left(\boldsymbol{\varepsilon}_{n+1}\right) \tag{10}$$

Therefore $w_\Delta\left(\boldsymbol{\varepsilon}\right)$ is called the condensed incremental potential.

5.2 Composite materials

5.2.1 Local problem

We consider that a representative volume element (*r.v.e.*) V of the composite material contains N components occupying domains $V^{(r)}$ with positional characteristic function $\chi^{(r)}\left(x\right)$ and volume fraction $c^{(r)}$. Each component has its own potentials $w^{(r)}$ and $\varphi^{(r)}$ according to equation (3). The free-energy w and the dissipation potential φ at position x in the *r.v.e.* are given by:

$$w\left(x,\boldsymbol{\varepsilon},\boldsymbol{\varepsilon}^{vp}\right)=\sum_{r=1}^{N}\chi^{(r)}(x)\,w^{(r)}\left(\boldsymbol{\varepsilon},\boldsymbol{\varepsilon}^{vp}\right),\quad \varphi\left(\boldsymbol{\varepsilon},\dot{\boldsymbol{\varepsilon}}^{vp}\right)=\sum_{r=1}^{N}\chi^{(r)}(x)\varphi^{(r)}\left(\dot{\boldsymbol{\varepsilon}}^{vp}\right) \qquad (11)$$

Note that the *r.v.e.* is submitted to a macroscopic strain $E(t)$ prescribed on its boundary ∂V, the local problem is solved as:

$$\left.\begin{aligned}
&\boldsymbol{\sigma}=\frac{\partial w}{\partial\boldsymbol{\varepsilon}}\left(\boldsymbol{\varepsilon},\boldsymbol{\varepsilon}^{vp}\right)\quad \text{for } (x,t)\in V\times[0,T]\\
&\frac{\partial w}{\partial\boldsymbol{\varepsilon}^{vp}}\left(\boldsymbol{\varepsilon},\boldsymbol{\varepsilon}^{vp}\right)+\frac{\partial\varphi}{\partial\dot{\boldsymbol{\varepsilon}}^{vp}}\left(\dot{\boldsymbol{\varepsilon}}^{vp}\right)=0\ \text{ for } (x,t)\in V\times[0,T]\\
&\mathrm{div}\boldsymbol{\sigma}=0\quad \text{for } (x,t)\in V\times[0,T]\\
&<\boldsymbol{\varepsilon}(x,t)>=\mathbf{E}(t)\ \text{ on } \partial\mathrm{V}
\end{aligned}\right\} \qquad (12)$$

All the local fields $\boldsymbol{\sigma}$, $\boldsymbol{\varepsilon}$, $\boldsymbol{\varepsilon}^{vp}$ depend on x and t, $<\bullet>$ denotes the average over V. The local boundary conditions are determined on the basis of the macroscopic strain tensor on ∂V. The macroscopic overall response of the composite along the path of strain $\mathbf{E}(t)$ is the history of average stress $\boldsymbol{\Sigma}(t)$, with $\boldsymbol{\Sigma}(t)=<\boldsymbol{\sigma}(x,t)>$.

5.2.2 Effective energy of the composite

According to the time-discretization procedure defined in section 1.2 and the equation (10), the discretized version of the local problem (12) is expressed as:

$$\left.\begin{aligned}
&\boldsymbol{\sigma}_{n+1}=\frac{\partial w_{\Delta}}{\partial\boldsymbol{\varepsilon}}\left(\boldsymbol{\varepsilon}_{n+1}\right)\quad \text{for } x\in V,\\
&\mathrm{div}\boldsymbol{\sigma}_{n+1}=0\quad \text{for } x\in V,\\
&<\boldsymbol{\varepsilon}_{n+1}>=\mathbf{E}_{n+1}\ \text{ on } \partial\mathrm{V}.
\end{aligned}\right\} \qquad (13)$$

According to (6), the incremental potential J and the condensed incremental potential $w_{\Delta}(\boldsymbol{\varepsilon})$ are given by:

$$\left.\begin{aligned}
&J\left(\boldsymbol{\varepsilon},\boldsymbol{\varepsilon}^{vp}\right)=\sum_{r=1}^{N}\left(w^{(r)}\left(\boldsymbol{\varepsilon},\boldsymbol{\varepsilon}^{vp}\right)+\Delta t\varphi\left(\frac{\boldsymbol{\varepsilon}^{vp}-\boldsymbol{\varepsilon}_{n}^{vp}(x)}{\Delta t}\right)\right)\chi^{(r)}(x),\\
&w_{\Delta}(\boldsymbol{\varepsilon},x)=\inf_{\boldsymbol{\varepsilon}^{vp}}\ J\left(\boldsymbol{\varepsilon},\boldsymbol{\varepsilon}^{vp},x\right)
\end{aligned}\right\} \qquad (14)$$

The effective energy of a composite material $\tilde{w}_{\Delta}$ is defined by:

$$\tilde{w}_{\Delta}\left(\mathbf{E}_{n+1}\right)=\inf_{<\boldsymbol{\varepsilon}>=\mathbf{E}_{n+1}}<w_{\Delta}(\boldsymbol{\varepsilon})>=\inf_{<\boldsymbol{\varepsilon}>=\mathbf{E}_{n+1}}<\inf_{\boldsymbol{\varepsilon}^{vp}}J\left(\boldsymbol{\varepsilon},\boldsymbol{\varepsilon}^{vp}\right)> \qquad (15)$$

The derivative of the effective energy $\tilde{w}_{\Delta}$ with respect to E_{n+1} reads as:

$$\frac{\partial \tilde{w}_\Delta}{\partial \mathbf{E}}\left(\mathbf{E}_{n+1}\right) = < \frac{\partial J}{\partial \boldsymbol{\varepsilon}} : \frac{\partial \boldsymbol{\varepsilon}}{\partial \mathbf{E}} > + < \frac{\partial J}{\partial \boldsymbol{\varepsilon}^{vp}} : \frac{\partial \boldsymbol{\varepsilon}^{vp}}{\partial \mathbf{E}} > \tag{16}$$

The last term in (16) vanishes by the stationarity of J with respect to $\boldsymbol{\varepsilon}^{vp}$, thanks to the relation $\boldsymbol{\sigma} = \partial J / \partial \boldsymbol{\varepsilon}$ and Hill's lemma:

$$< \boldsymbol{\sigma}_{n+1} : \frac{\partial \boldsymbol{\varepsilon}}{\partial \mathbf{E}} > = < \boldsymbol{\sigma}_{n+1} > : < \frac{\partial \boldsymbol{\varepsilon}}{\partial \mathbf{E}} > = < \boldsymbol{\sigma}_{n+1} > = \boldsymbol{\Sigma}_{n+1} \tag{17}$$

Therefore, the average stress $\boldsymbol{\Sigma}_{n+1} = < \boldsymbol{\sigma}_{n+1} >$ is deduced from the derivative of the effective energy $\tilde{w}_\Delta$ with respect to the macroscopic strain $\mathbf{E}_{n+1}$:

$$\boldsymbol{\Sigma}_{n+1} = \frac{\partial \tilde{w}_\Delta}{\partial \mathbf{E}}\left(\mathbf{E}_{n+1}\right) \tag{18}$$

Consequently, after time-discretization, the homogenization of the problem (12) is reduced to the variational problem (15). The latter problem comes to find the effective energy $\tilde{w}_\Delta$ of the composite material with one potential w_Δ.

5.2.3 Application to the Callovo-Oxfordian argillite

Experimental investigations mentioned in previous chapters show that the COX argillite exhibits a volumetric compressibility to dilatancy transition. In order to account for this specific property, as for most of geomaterials, a non-associate viscoplastic flow rule is adopted. The rate of viscoplastic mean strain $\dot{\varepsilon}_m^{vp} = \mathrm{tr}(\dot{\boldsymbol{\varepsilon}}^{vp})/3$ can be expressed as follows:

$$\dot{\varepsilon}_m^{vp} = \mathrm{tr}(\dot{\boldsymbol{\varepsilon}}^{vp})/3 = \dot{\gamma}\frac{\partial Q}{\partial \sigma_m} \tag{19}$$

The function Q is the local viscoplastic potential, σ_m is the mean stress, $\dot{\gamma}$ is the viscoplastic multiplicator. In this study, the following potential based on Drucker-Prager criterion is used (Chew and al., 2006):

$$Q = \sqrt{3J_2} + \sigma_m \tan\beta \tag{20}$$

J_2 is the second invariant of the deviatoric part of the Cauchy stress tensor $\boldsymbol{\sigma}$, β is a parameter controlling the viscoplastic dilatancy. γ^{vp} is defined as the viscoplastic hardening variable and uniform in the rth phase:

$$\dot{\gamma}^{vp} = \sqrt{\frac{2}{3}\left\langle \dot{\mathbf{e}}^{vp} : \dot{\mathbf{e}}^{vp} \right\rangle_r} = \dot{\gamma}\sqrt{\frac{2}{3}\left\langle dev\left(\frac{\partial Q}{\partial \boldsymbol{\sigma}}\right) : dev\left(\frac{\partial Q}{\partial \boldsymbol{\sigma}}\right)\right\rangle_r} = \dot{\gamma} \tag{21}$$

The tensor $\dot{\mathbf{e}}^{vp}$ denotes the deviatoric part of $\dot{\boldsymbol{\varepsilon}}^{vp}$. With (20) and (21), the mean strain evolution (19) is rewritten as:

$$\dot{\varepsilon}_m^{vp} = \dot{\gamma}^{vp} \tan\beta \tag{22}$$

Assumption 1: The mean part of viscoplastic strain tensor ε_m^{vp} at t_{n+1} is obtained by:

$$\left(\varepsilon_m^{vp}\right)_{n+1} = \left(\varepsilon_m^{vp}\right)_n + \Delta t\left(\dot{\varepsilon}_m^{vp}\right)_{n+1} = \left(\varepsilon_m^{vp}\right)_n + \Delta t\dot{\gamma}_{n+1}^{vp}\tan\beta \tag{23}$$

The mean strain $\left(\varepsilon_m^{vp}\right)_n$ is the outcome in previous step, considered as a known field. The mean part of viscoplastic strain tensor $\left(\varepsilon_m^{vp}\right)_{n+1}$ is regarded as a sole function of $\dot{\gamma}_{n+1}^{vp}$ and independent of the others variables.

The viscoplastic strain $\boldsymbol{\varepsilon}^{vp}$ at t_{n+1} can therefore be written as the sum of two parts:

$$\boldsymbol{\varepsilon}_{n+1}^{vp} = \left(\varepsilon_m^{vp}\right)_{n+1}\boldsymbol{\delta} + \mathbf{e}_{n+1}^{vp} = \left[\left(\varepsilon_m^{vp}\right)_n + \Delta t\dot{\gamma}_{n+1}^{vp}\tan\beta\right]\boldsymbol{\delta} + \mathbf{e}_{n+1}^{vp} \tag{24}$$

with $\boldsymbol{\delta}$ the second order unit tensor.

Assumption 2: The constituents of argillite are isotropic materials. Further, considering both isotropic and kinematic hardening, the free-energy of the clay matrix w^m can be written as:

$$w^m\left(\boldsymbol{\varepsilon}, \boldsymbol{\varepsilon}^{vp}, \gamma^{vp}\right) = \frac{1}{2}\left(\boldsymbol{\varepsilon} - \boldsymbol{\varepsilon}^{vp}\right) : \mathbb{L}^m : \left(\boldsymbol{\varepsilon} - \boldsymbol{\varepsilon}^{vp}\right) + w^{\gamma}\left(\gamma^{vp}\right) \tag{25}$$

The fourth-order tensor $\mathbb{L}^m$ can be characterized by two elastic moduli (a bulk modulus and a shear modulus) as $\mathbb{L}^m = 3k^m\mathbb{J} + 2\mu^m\mathbb{K}$.

The free-energy of the linear elastic inclusions w^i is defined by the same form as that for the clay matrix:

$$w^i\left(\boldsymbol{\varepsilon}\right) = \frac{1}{2}\boldsymbol{\varepsilon} : \mathbb{L}^i : \boldsymbol{\varepsilon} \quad \text{with} \quad \mathbb{L}^i = 3k^i\mathbb{J} + 2\mu^i\mathbb{K} \tag{26}$$

Thanks to the relation in the assumption 1, we replace $\boldsymbol{\varepsilon}^{vp}$ in (25) and we obtain:

$$w^m\left(\boldsymbol{\varepsilon}_{n+1},\boldsymbol{\varepsilon}^{vp}_{n+1},\gamma^{vp}\right)=\frac{1}{2}\left(\boldsymbol{\varepsilon}_{n+1}-\mathbf{e}^{vp}_{n+1}-\left[\left(\varepsilon^{vp}_m\right)_n+\Delta t\dot{\gamma}^{vp}_{n+1}\tan\beta\right]\boldsymbol{\delta}\right):$$
$$\mathbb{L}^m:\left(\boldsymbol{\varepsilon}_{n+1}-\mathbf{e}^{vp}_{n+1}-\left[\left(\varepsilon^{vp}_m\right)_n+\Delta t\dot{\gamma}^{vp}_{n+1}\tan\beta\right]\boldsymbol{\delta}\right)+w^{\gamma}\left(\gamma^{vp}_{n+1}\right) \tag{27}$$

Assumption 3: The dissipation potential φ, which is a convex function of $\dot{\boldsymbol{\varepsilon}}^{vp}$, is assumed to be a function of $\dot{\gamma}^{vp}$:

$$\varphi^{(r)}\left(\dot{\boldsymbol{\varepsilon}}^{vp}\right)=\varphi^{(r)}\left(\dot{\gamma}^{vp}\right)=\varphi^{(r)}\left(\dot{\mathbf{e}}^{vp}\right)$$

The secant viscosity η_{sct} of the rth phase is defined as:

$$\frac{\partial\varphi^{(r)}}{\partial\dot{\mathbf{e}}^{vp}}\left(\dot{\mathbf{e}}^{vp}\right)=2\eta^{(r)}_{sct}\left(\dot{\gamma}^{vp}\right)\dot{\mathbf{e}}^{vp} \tag{28}$$

Remarks:

1. With the assumptions 2 and 3, we can also obtain the driving forces associated with $\boldsymbol{\varepsilon}$ and $\mathbf{e}^{vp}$ as in section 1.1:

$$\boldsymbol{\sigma}_{n+1}=\frac{\partial w}{\partial\boldsymbol{\varepsilon}}\left(\boldsymbol{\varepsilon}_{n+1},\boldsymbol{\varepsilon}^{vp}_{n+1},\gamma^{vp}\right)=-\frac{\partial w}{\partial\mathbf{e}^{vp}}\left(\boldsymbol{\varepsilon}_{n+1},\boldsymbol{\varepsilon}^{vp}_{n+1},\gamma^{vp}\right)=\frac{\partial\varphi}{\partial\dot{\mathbf{e}}^{vp}}\left(\dot{\mathbf{e}}^{vp}_{n+1}\right),$$

   The system (4) becomes:

$$\boldsymbol{\sigma}_{n+1}=\frac{\partial w}{\partial\boldsymbol{\varepsilon}}\left(\boldsymbol{\varepsilon}_{n+1},\boldsymbol{\varepsilon}^{vp}_{n+1},\gamma^{vp}_{n+1}\right),\quad\frac{\partial w}{\partial\mathbf{e}^{vp}}\left(\boldsymbol{\varepsilon}_{n+1},\boldsymbol{\varepsilon}^{vp}_{n+1},\gamma^{vp}_{n+1}\right)+\frac{\partial\varphi}{\partial\dot{\mathbf{e}}^{vp}}\left(\dot{\mathbf{e}}^{vp}_{n+1}\right)=0 \tag{29}$$

   Similarly, the variational problem (14) and the effective energy $\tilde{w}_\Delta$ can be expressed by the stationarity of J with respect to $\mathbf{e}^{vp}$ instead of $\boldsymbol{\varepsilon}^{vp}$:

$$\left.\begin{aligned}J\left(\boldsymbol{\varepsilon},\boldsymbol{\varepsilon}^{vp}\right)&=\sum_{r=1}^{N}\left(w^{(r)}\left(\boldsymbol{\varepsilon},\boldsymbol{\varepsilon}^{vp},\gamma^{vp}\right)+\Delta t\varphi\left(\frac{\mathbf{e}^{vp}-\mathbf{e}^{vp}_n(x)}{\Delta t}\right)\right)\chi^{(r)}(x),\\ w_\Delta(\boldsymbol{\varepsilon},x)&=\inf_{\mathbf{e}^{vp}}J\left(\boldsymbol{\varepsilon},\boldsymbol{\varepsilon}^{vp},x\right)\end{aligned}\right\} \tag{30}$$

$$\tilde{w}_\Delta\left(\mathbf{E}_{n+1}\right)=\inf_{<\boldsymbol{\varepsilon}>=\mathbf{E}_{n+1}}<w_\Delta(\boldsymbol{\varepsilon})>=\inf_{<\boldsymbol{\varepsilon}>=\mathbf{E}_{n+1}}<\inf_{\mathbf{e}^{vp}}J\left(\boldsymbol{\varepsilon},\boldsymbol{\varepsilon}^{vp}\right)> \tag{31}$$

2. The viscoplastic hardening law is then specified as the following exponential form:

$$\alpha\left(\gamma^{vp}\right)=\frac{\partial w}{\partial\gamma^{vp}}\left(\boldsymbol{\varepsilon}_{n+1},\boldsymbol{\varepsilon}^{vp}_{n+1},\gamma^{vp}\right)=\frac{\partial w^{\gamma}}{\partial\gamma^{vp}}\left(\gamma^{vp}\right)=\alpha_m\left(1-e^{-b\gamma^{vp}}\right) \tag{32}$$

where α_m is the ultimate value of hardening function and b is a parameter controlling viscoplastic hardening rate.

3. According to the assumption 3, consider the power-law potential in the form:

$$\varphi^{(r)}\left(\dot{\mathbf{e}}^{vp}\right) = R^{(r)}\dot{\gamma}^{vp} + \frac{\sigma_0^{(r)}\dot{\varepsilon}_0}{(m+1)}\left(\frac{\dot{\gamma}^{vp}}{\dot{\varepsilon}_0}\right)^{m+1} \tag{33}$$

The constitutive relation corresponding to the free-energy (w) and dissipation potential (φ) defined respectively by (27) and (33) reads:

$$\dot{\boldsymbol{\varepsilon}} = M^{(r)} : \dot{\boldsymbol{\sigma}} + \frac{3}{2}\dot{\varepsilon}_0\left(\frac{\left(\sigma_{eq} - R^{(r)}\right)^+}{\sigma_0^{(r)}}\right)^{1/m}\left(\frac{\mathbf{S}}{\sigma_{eq}} + \dot{\gamma}^{vp}\boldsymbol{\delta}\tan\beta\right) \tag{34}$$

where $M^{(r)}$ is the elastic compliance tensor; $\mathbf{S}$ and σ_{eq} are the deviatoric part of stress tensor and the von-Mises equivalent stress, respectively; $R^{(r)}$ is the plastic threshold. Considering the viscoplastic hardening law (32) and the influence of confining pressure, the threshold is defined as $R^{(r)} = \alpha_m\left(e^{-b\gamma^{vp}} - 1\right)p$, with p the mean stress.

5.3 Estimation of the effective energy by a variational process

In term of the concluding paragraph in section 2.2, we will determine the effective energy $\tilde{w}_\Delta$ by means of a method inspired of the variational procedure of Ponte Castañeda (1992).

5.3.1 Variational procedure

Considering that the original potential J is difficult to homogenize, we introduce a reference energy J_0 which is chosen to be piecewise uniform,

$$J_0\left(x, \boldsymbol{\varepsilon}, \mathbf{e}^{vp}\right) = \sum_{r=1}^{N} J_0\left(\boldsymbol{\varepsilon}, \mathbf{e}^{vp}\right)\chi^{(r)}(x) \tag{35}$$

where

$$J_0^{(r)}\left(\boldsymbol{\varepsilon}, \mathbf{e}^{vp}\right) = w^{(r)}\left(\boldsymbol{\varepsilon}, \boldsymbol{\varepsilon}^{vp}, \gamma^{vp}\right) + \frac{\eta_0^{(r)}}{\Delta t}\left(\mathbf{e}^{vp} - \mathbf{e}_0^{(r)}\right) : \left(\mathbf{e}^{vp} - \mathbf{e}_0^{(r)}\right) \tag{36}$$

In this expression, $\eta_0^{(r)}$ and $\mathbf{e}_0^{(r)}$ are uniform in the r^{th} phase and will be chosen

specifically in the next section. Let ΔJ be the difference between J and J_0:

$$\begin{aligned}\Delta J\left(\mathbf{e}^{vp}\right) &= J_0\left(x,\boldsymbol{\varepsilon},\mathbf{e}^{vp}\right)\\ &= \sum_{r=1}^{N}\left[\Delta t\varphi^{(r)}\left(\frac{\mathbf{e}^{vp}-\mathbf{e}_n^{vp}(x)}{\Delta t}\right)-\frac{\eta_0^{(r)}}{\Delta t}\left(\mathbf{e}^{vp}-\mathbf{e}_0^{(r)}\right):\left(\mathbf{e}^{vp}-\mathbf{e}_0^{(r)}\right)\right]\chi^{(r)}(x)\end{aligned} \tag{37}$$

After that, (31) can be rewritten as:

$$\begin{aligned}\tilde{w}_\Delta\left(\mathbf{E}_{n+1}\right) &= \inf_{<\boldsymbol{\varepsilon}>=\mathbf{E}_{n+1}} <w_\Delta(\boldsymbol{\varepsilon})> = \inf_{<\boldsymbol{\varepsilon}>=\mathbf{E}_{n+1}} \inf_{\mathbf{e}^{vp}} <J_0\left(\boldsymbol{\varepsilon},\mathbf{e}^{vp}\right)+\Delta J\left(\mathbf{e}^{vp}\right)>\\ &\le \inf_{<\boldsymbol{\varepsilon}>=\mathbf{E}_{n+1}}\left[\inf_{\mathbf{e}^{vp}} <J_0\left(\boldsymbol{\varepsilon},\mathbf{e}^{vp}\right)> + <\sup_{\mathbf{e}^{vp}}\ \Delta J\left(\mathbf{e}^{vp}\right)>\right]\end{aligned} \tag{38}$$

The supremum of ΔJ over $\mathbf{e}^{vp}$ in the last expression provides a rigorous upper bound for $\tilde{w}_\Delta$. Ponte Castañeda and Willis (1999) and Ponte Castañeda (2002) have observed, in a different but similar context, that a sharper estimate for $\tilde{w}_\Delta$ could be obtained by only requiring the stationarity (rather than supremum) of ΔJ with respect to $\mathbf{e}^{vp}$ in (38):

$$\tilde{w}_\Delta\left(\mathbf{E}_{n+1}\right) \approx \inf_{<\boldsymbol{\varepsilon}>=\mathbf{E}_{n+1}}\left[\inf_{\mathbf{e}^{vp}} <J_0\left(\boldsymbol{\varepsilon},\mathbf{e}^{vp}\right)> + <\operatorname{Stat}_{\mathbf{e}^{vp}}\ \Delta J\left(\mathbf{e}^{vp}\right)>\right] \tag{39}$$

It is clear that the expression (39) has no upper bound character and is only an estimate (hopefully accurate) of $\tilde{w}_\Delta$.

5.3.2 Linear viscoplastic constituents

First, we deal with the stationarity condition $\operatorname{Stat}_{\mathbf{e}^{vp}}\ \Delta J\left(\mathbf{e}^{vp}\right)$, which becomes:

$$\operatorname{Stat}_{\mathbf{e}^{vp}}\sum_{r=1}^{N}\left[\frac{\eta_{sct}^{(r)}}{\Delta t}\left(\mathbf{e}^{vp}-\mathbf{e}_n^{vp}\right):\left(\mathbf{e}^{vp}-\mathbf{e}_n^{vp}\right)-\frac{\eta_0^{(r)}}{\Delta t}\left(\mathbf{e}^{vp}-\mathbf{e}_0^{(r)}\right):\left(\mathbf{e}^{vp}-\mathbf{e}_0^{(r)}\right)\right]\chi^{(r)}(x) \tag{40}$$

The solution $\mathbf{e}^{vp}$ of the above stationarity problem satisfies the following condition in the r^{th} phase:

$$\frac{\eta_{sct}^{(r)}}{\Delta t}\left(\mathbf{e}^{vp}-\mathbf{e}_n^{vp}\right)=\frac{\eta_0^{(r)}}{\Delta t}\left(\mathbf{e}^{vp}-\mathbf{e}_0^{(r)}\right) \tag{41}$$

and therefore can be expressed as follows:

$$\mathbf{e}^{vp}(x)=\frac{\mathbf{e}_n^{vp}(x)-\theta^{(r)}\mathbf{e}_0^{(r)}}{1-\theta^{(r)}} \qquad \text{with} \quad \theta=\eta_0^{(r)}/\eta_{sct}^{(r)} \tag{42}$$

Thanks to this relation, the last term in (39) can be rewritten and the estimate for $\tilde{w}_\Delta$ becomes:

$$\begin{aligned}\tilde{w}_\Delta(\mathbf{E}_{n+1}) \approx & \inf_{<\boldsymbol{\varepsilon}>=\mathbf{E}_{n+1}}\left[\inf_{\mathbf{e}^{vp}} < J_0\left(\varepsilon,\mathbf{e}^{vp}\right)>\right] \\ & +\sum_{r=1}^{N} c^{(r)}\left\langle \frac{\eta_{sct}^{(r)}\theta^{(r)}}{\Delta t\left(\theta^{(r)}-1\right)}\left(\mathbf{e}_n^{vp}-\mathbf{e}_0^{(r)}\right):\left(\mathbf{e}_n^{vp}-\mathbf{e}_0^{(r)}\right)\right\rangle_r\end{aligned} \tag{43}$$

where $\theta^{(r)}$ and $\mathbf{e}_0^{(r)}$ remain to be determined.

Therefore the estimate (43) can be optimized with respect to $\theta^{(r)}$ and $\mathbf{e}_0^{(r)}$. The stationarity of the right-hand side of (43) with respect to $\theta^{(r)}$ reads:

$$\frac{\partial}{\partial\theta^{(r)}}\left\langle J_0{}^{(r)}\left(\boldsymbol{\varepsilon},\mathbf{e}^{vp}\right)+\frac{\eta_{sct}^{(r)}\theta^{(r)}}{\Delta t\left(\theta^{(r)}-1\right)}\left(\mathbf{e}_n^{vp}-\mathbf{e}_0^{(r)}\right):\left(\mathbf{e}_n^{vp}-\mathbf{e}_0^{(r)}\right)\right\rangle_r=0$$

$$\Rightarrow \theta^{(r)}=1\pm\sqrt{\frac{\left\langle\left(\mathbf{e}_n^{vp}-\mathbf{e}_0^{(r)}\right):\left(\mathbf{e}_n^{vp}-\mathbf{e}_0^{(r)}\right)\right\rangle_r}{\left\langle\left(\mathbf{e}^{vp}-\mathbf{e}_0^{(r)}\right):\left(\mathbf{e}^{vp}-\mathbf{e}_0^{(r)}\right)\right\rangle_r}} \tag{44}$$

The two roots (defined with – and +, respectively) have been tested separately and compared with exact results (FEM) (Lahellec and Suquet, 2006). It is shown that the root defined with – is more applicable and thus will be adopted in the subsequent discussion.

Similarly, the stationarity condition with respect to $\mathbf{e}_0^{(r)}$ is given by:

$$\frac{\partial}{\partial\mathbf{e}_n^{(r)}}\left\langle J_0{}^{(r)}\left(\boldsymbol{\varepsilon},\mathbf{e}^{vp}\right)+\frac{\eta_{sct}^{(r)}\theta^{(r)}}{\Delta t\left(\theta^{(r)}-1\right)}\left(\mathbf{e}_n^{vp}-\mathbf{e}_0^{(r)}\right):\left(\mathbf{e}_n^{vp}-\mathbf{e}_0^{(r)}\right)\right\rangle_r=0$$

$$\Rightarrow \mathbf{e}_0^{(r)}=\frac{\left\langle\mathbf{e}_n^{vp}\right\rangle_r+\left(\theta^{(r)}-1\right)\left\langle\mathbf{e}^{vp}\right\rangle_r}{\theta^{(r)}} \tag{45}$$

Through the infimum problem in (43), the traceless field $\mathbf{e}^{vp}$ can be given by:

$$\mathbf{e}^{vp}\left(x\right)=\left(\frac{2\eta_{sct}^{(r)}\theta^{(r)}}{\Delta t}\mathbb{K}+\mathbb{L}^{(r)}\right)^{-1}:\left[\mathbb{K}:\mathbb{L}^{(r)}:\boldsymbol{\varepsilon}\left(x\right)+\frac{2\eta_{sct}^{(r)}\theta^{(r)}}{\Delta t}\mathbf{e}_0^{(r)}\right] \tag{46}$$

where $\mathbb{K}$ is the isotropic fourth-order tensor associated with the deviatoric projection and $\boldsymbol{\varepsilon}\left(x\right)$ is the strain field solution of the infimum problem of the effective energy among all admissible strain fields compatible with an average strain $\mathbf{E}$.

The reference energy J_0 can be minimized as soon as the above variables ($\mathbf{e}^{vp}\left(x\right),\theta^{(r)}$ and $\mathbf{e}_0^{(r)}$) are determined. Substituting (46) into the expression of J_0 leads to:

$$\underset{\mathbf{e}^{vp}}{\mathrm{Inf}}\ J_0^{(r)}\left(\boldsymbol{\varepsilon},\mathbf{e}^{vp}\right)=\frac{1}{2}\boldsymbol{\varepsilon}:\mathbb{L}_{eff}^{(r)}:\boldsymbol{\varepsilon}+\boldsymbol{\rho}_{eff}^{(r)}:\boldsymbol{\varepsilon}+\beta_{eff}^{(r)} \tag{47}$$

The tensors $\mathbb{L}_{eff}^{(r)}$, $\boldsymbol{\rho}_{eff}^{(r)}$ and $\beta_{eff}^{(r)}$ are piecewise uniform in the *r*th phase, and defined by (see detailed process in Appendix A):

$$\left.\begin{aligned}
&\mathbb{L}_{eff}^{(r)}=\mathbb{L}^{(r)}-\mathbb{L}^{(r)}:\mathbb{K}:\left(\frac{2\eta_{sct}^{(r)}\theta^{(r)}}{\Delta t}\mathbb{K}+\mathbb{L}^{(r)}\right)^{-1}:\mathbb{K}:\mathbb{L},\\
&\boldsymbol{\rho}_{eff}^{(r)}=-\mathbb{L}^{(r)}:\left(\frac{2\eta_{sct}^{(r)}\theta^{(r)}}{\Delta t}\mathbb{K}+\mathbb{L}^{(r)}\right)^{-1}\frac{2\eta_{sct}^{(r)}\theta^{(r)}}{\Delta t}\mathbf{e}_0^{(r)}-\mathbb{L}^{(r)}:\left(\boldsymbol{\varepsilon}_m^{vp}\right)_{n+1},\\
&\beta_{eff}^{(r)}=\frac{2\eta_{sct}^{(r)}\theta^{(r)}}{\Delta t}\mathbf{e}_0^{(r)}:\left(\frac{2\eta_{sct}^{(r)}\theta^{(r)}}{\Delta t}\mathbb{K}+\mathbb{L}^{(r)}\right)^{-1}:\mathbb{L}^{(r)}:\mathbf{e}_0^{(r)}-\mathbf{e}_{n+1}^{vp}:\mathbb{L}^{(r)}:\left(\boldsymbol{\varepsilon}_m^{vp}\right)_{n+1}\\
&\qquad+\frac{1}{2}\left(\boldsymbol{\varepsilon}_m^{vp}\right)_{n+1}:\mathbb{L}^{(r)}:\left(\boldsymbol{\varepsilon}_m^{vp}\right)_{n+1}.
\end{aligned}\right\} \tag{48}$$

Just as (7), a reference condensed incremental potential is defined by:

$$w_0^{(r)}\left(\boldsymbol{\varepsilon}\right)=\underset{\mathbf{e}^{vp}}{\mathrm{Inf}}\ J_0^{(r)}\left(\boldsymbol{\varepsilon},\mathbf{e}^{vp}\right) \tag{49}$$

which is the free-energy of a linear thermoelastic phase. Then the estimate of $\tilde{w}_\Delta$ is given by:

$$\tilde{w}_\Delta\left(\mathbf{E}\right)=\tilde{w}_0\left(\mathbf{E}\right)+\sum_{r=1}^{N}c^{(r)}\left\langle\frac{\eta_{sct}^{(r)}\theta^{(r)}}{\Delta t\left(\theta^{(r)}-1\right)}\left(\mathbf{e}_n^{vp}-\mathbf{e}_0^{(r)}\right):\left(\mathbf{e}_n^{vp}-\mathbf{e}_0^{(r)}\right)\right\rangle_r \tag{50}$$

with $\tilde{w}_0(\mathbf{E}) = \inf_{\langle\boldsymbol{\varepsilon}\rangle=\mathbf{E}} \sum_{r=1}^{N} c^{(r)} \left\langle w_0^{(r)}(\boldsymbol{\varepsilon}) \right\rangle_r$.

The homogenized response of the composite at time t_{n+1}, as predicted by the present model, reads:

$$\boldsymbol{\Sigma}_{n+1} = \frac{\partial \tilde{w}_\Delta}{\partial \mathbf{E}}(\mathbf{E}_{n+1}) = \frac{\partial \tilde{w}_0}{\partial \mathbf{E}}(\mathbf{E}_{n+1}) \tag{51}$$

The relation (51) implies that the macroscopic stress in the composite at time t_{n+1} coincides with the average stress in the linear thermoelastic composite defined by (Lahellec and Suquet, 2007):

$$\boldsymbol{\Sigma}_{n+1} = \langle \boldsymbol{\sigma}_{n+1} \rangle = \sum_{r=1}^{N} c^{(r)} \left[\mathbb{L}_{eff}^{(r)} : \langle \boldsymbol{\varepsilon} \rangle_r + \boldsymbol{\rho}_{eff}^{(r)} \right] \tag{52}$$

with $\boldsymbol{\varepsilon}$ and $\boldsymbol{\sigma}$ the local strain and stress fields, respectively. Therefore the actual strain and stress fields are approximated by the same fields in the linear thermoelastic composite. Note that the last term of (47) is not really needed because its derivative with respect to $\boldsymbol{\varepsilon}$ is zero.

5.4 Preparation for application

5.4.1 Expression of secant viscosity η_{sct}

According to (28) and (33), the secant viscosity η_{sct} of the rth phase will be derived by the derivative of the dissipation potential φ with respect to $\dot{\mathbf{e}}^{vp}$:

$$\begin{aligned}
\frac{\partial \varphi^{(r)}}{\partial \dot{\mathbf{e}}^{vp}}\left(\dot{\mathbf{e}}^{vp}\right) &= \frac{\partial}{\partial \dot{\mathbf{e}}^{vp}}\left[R^{(r)}\dot{\gamma}^{vp} + \frac{\sigma_0^{(r)}\dot{\varepsilon}_0}{(m+1)}\left(\frac{\dot{\gamma}^{vp}}{\dot{\varepsilon}_0}\right)^{m+1}\right] = R^{(r)}\frac{\partial \dot{\gamma}^{vp}}{\partial \dot{\mathbf{e}}^{vp}} + \sigma_0^{(r)}\left(\frac{\dot{\gamma}^{vp}}{\dot{\varepsilon}_0}\right)^{m}\frac{\partial \dot{\gamma}^{vp}}{\partial \dot{\mathbf{e}}^{vp}} \\
&= \frac{2}{3}\left[\frac{R^{(r)}}{\dot{\gamma}^{vp}} + \frac{\sigma_0}{\dot{\varepsilon}_0}\left(\frac{\dot{\gamma}^{vp}}{\dot{\varepsilon}_0}\right)^{m-1}\right]\dot{\mathbf{e}}^{vp} \\
&= \frac{2}{3}\left[\frac{R^{(r)}}{\sqrt{\frac{2}{3}\left\langle \dot{\mathbf{e}}^{vp} : \dot{\mathbf{e}}^{vp} \right\rangle_r}} + \frac{\sigma_0}{\dot{\varepsilon}_0}\left(\frac{\sqrt{\frac{2}{3}\left\langle \dot{\mathbf{e}}^{vp} : \dot{\mathbf{e}}^{vp} \right\rangle_r}}{\dot{\varepsilon}_0}\right)^{m-1}\right]\dot{\mathbf{e}}^{vp}
\end{aligned}$$

$$\Rightarrow \eta_{sct}^{(r)} = \frac{1}{3}\left[\frac{R^{(r)}}{\sqrt{\frac{2}{3}\left\langle \dot{\mathbf{e}}^{vp} : \dot{\mathbf{e}}^{vp} \right\rangle_r}} + \frac{\sigma_0}{\dot{\varepsilon}_0}\left(\frac{\sqrt{\frac{2}{3}\left\langle \dot{\mathbf{e}}^{vp} : \dot{\mathbf{e}}^{vp} \right\rangle_r}}{\dot{\varepsilon}_0}\right)^{m-1}\right] \tag{53}$$

The first- and second-order moments of $\dot{\mathbf{e}}^{vp}$ remain to be determined and read:

$$\left\langle \dot{\mathbf{e}}^{vp} \right\rangle_r = \frac{1}{\Delta t}\left[\left\langle \mathbf{e}^{vp} \right\rangle_r - \left\langle \mathbf{e}_n^{vp} \right\rangle_r\right] \tag{54}$$

$$\left\langle \dot{\mathbf{e}}^{vp} : \dot{\mathbf{e}}^{vp} \right\rangle_r = \frac{1}{(\Delta t)^2}\left[\left\langle \left(\mathbf{e}^{vp} - \mathbf{e}_n^{vp}\right) : \left(\mathbf{e}^{vp} - \mathbf{e}_n^{vp}\right) \right\rangle_r\right] \tag{55}$$

5.4.2 Determination of the first- and second-order moments of $\dot{\mathbf{e}}^{vp}$

Following the expression (36), the first-order moment $\left\langle \dot{\mathbf{e}}^{vp} \right\rangle_r$ can be expressed as:

$$\begin{aligned}\left\langle \dot{\mathbf{e}}^{vp} \right\rangle_r &= \frac{1}{\Delta t}\left[\left\langle \mathbf{e}^{vp} \right\rangle_r - \left\langle \mathbf{e}_n^{vp} \right\rangle_r\right] \\ &= \frac{1}{\Delta t}\left[\left\langle \left(\frac{2\eta_{sct}^{(r)}\theta^{(r)}}{\Delta t}\mathbb{K} + \mathbb{L}^{(r)}\right)^{-1} : \left[\mathbb{K} : \mathbb{L}^{(r)} : \boldsymbol{\varepsilon}(x) + \frac{2\eta_{sct}^{(r)}\theta^{(r)}}{\Delta t}\mathbf{e}_0^{(r)}\right]\right\rangle_r - \left\langle \mathbf{e}_n^{vp} \right\rangle_r\right]\end{aligned} \tag{56}$$

We recall that $\eta_{sct}^{(r)}$, $\theta^{(r)}$ and $\mathbf{e}_0^{(r)}$ are uniform in the rth phase, we obtain:

$$\begin{aligned}\left\langle \mathbf{e}^{vp} \right\rangle_r &= \left\langle \left(\frac{2\eta_{sct}^{(r)}\theta^{(r)}}{\Delta t}\mathbb{K} + \mathbb{L}^{(r)}\right)^{-1} : \left[\mathbb{K} : \mathbb{L}^{(r)} : \boldsymbol{\varepsilon}(x) + \frac{2\eta_{sct}^{(r)}\theta^{(r)}}{\Delta t}\mathbf{e}_0^{(r)}\right]\right\rangle_r \\ &= \left(\frac{2\eta_{sct}^{(r)}\theta^{(r)}}{\Delta t}\mathbb{K} + \mathbb{L}^{(r)}\right)^{-1} : \left[\mathbb{K} : \mathbb{L}^{(r)} : \left\langle \boldsymbol{\varepsilon}(x) \right\rangle_r + \frac{2\eta_{sct}^{(r)}\theta^{(r)}}{\Delta t}\mathbf{e}_0^{(r)}\right]\end{aligned} \tag{57}$$

Similarly,

$$
\begin{aligned}
&\left\langle \mathbf{e}^{vp} : \mathbf{e}^{vp} \right\rangle_r \\
&= \left\langle \left[\left(\frac{2\eta_{sct}^{(r)}\theta^{(r)}}{\Delta t}\mathbb{K} + \mathbb{L}^{(r)} \right)^{-1} : \mathbb{L}^{(r)} : \mathbb{K} : \boldsymbol{\varepsilon} \right] : \left[\left(\frac{2\eta_{sct}^{(r)}\theta^{(r)}}{\Delta t}\mathbb{K} + \mathbb{L}^{(r)} \right)^{-1} : \mathbb{L}^{(r)} : \mathbb{K} : \boldsymbol{\varepsilon} \right] \right\rangle_r \\
&\quad + \frac{4\eta_{sct}^{(r)}\theta^{(r)}}{\Delta t} \left[\left(\frac{2\eta_{sct}^{(r)}\theta^{(r)}}{\Delta t}\mathbb{K} + \mathbb{L}^{(r)} \right)^{-1} : \mathbb{K} : \mathbb{L}^{(r)} : \left\langle \boldsymbol{\varepsilon} \right\rangle_r \right] : \left[\left(\frac{2\eta_{sct}^{(r)}\theta^{(r)}}{\Delta t}\mathbb{K} + \mathbb{L}^{(r)} \right)^{-1} : \mathbf{e}_0^{(r)} \right] \\
&\quad + \left(\frac{2\eta_{sct}^{(r)}\theta^{(r)}}{\Delta t} \right)^2 \left[\left(\frac{2\eta_{sct}^{(r)}\theta^{(r)}}{\Delta t}\mathbb{K} + \mathbb{L}^{(r)} \right)^{-1} : \mathbf{e}_0^{(r)} \right] : \left[\left(\frac{2\eta_{sct}^{(r)}\theta^{(r)}}{\Delta t}\mathbb{K} + \mathbb{L}^{(r)} \right)^{-1} : \mathbf{e}_0^{(r)} \right]
\end{aligned}
\tag{58}
$$

The first term of the right hand side is given by (see the relation (A.2) in Appendix (A)):

$$
\begin{aligned}
&\left\langle \left[\left(\frac{2\eta_{sct}^{(r)}\theta^{(r)}}{\Delta t}\mathbb{K} + \mathbb{L}^{(r)} \right)^{-1} : \mathbb{L}^{(r)} : \mathbb{K} : \boldsymbol{\varepsilon} \right] : \left[\left(\frac{2\eta_{sct}^{(r)}\theta^{(r)}}{\Delta t}\mathbb{K} + \mathbb{L}^{(r)} \right)^{-1} : \mathbb{L}^{(r)} : \mathbb{K} : \boldsymbol{\varepsilon} \right] \right\rangle_r \\
&= \left\langle \left[\left(\frac{1}{3k^{(r)}}\mathbb{J} + \frac{1}{\dfrac{2\eta^{(r)}\theta^{(r)}}{\Delta t} + 2\mu^{(r)}}\mathbb{K} \right) : \left(3k^{(r)}\mathbb{J} + 2\mu^{(r)}\mathbb{K} \right) : \mathbb{K} : \boldsymbol{\varepsilon} \right] \right. \\
&\quad \left. : \left[\left(\frac{1}{3k^{(r)}}\mathbb{J} + \frac{1}{\dfrac{2\eta^{(r)}\theta^{(r)}}{\Delta t} + 2\mu^{(r)}}\mathbb{K} \right) : \left(3k^{(r)}\mathbb{J} + 2\mu^{(r)}\mathbb{K} \right) : \mathbb{K} : \boldsymbol{\varepsilon} \right] \right\rangle_r \\
&= \left(\frac{\mu^{(r)}}{\dfrac{\eta^{(r)}\theta^{(r)}}{\Delta t} + \mu^{(r)}} \right)^2 \mathbb{K} :: \left\langle \boldsymbol{\varepsilon} \otimes \boldsymbol{\varepsilon} \right\rangle_r
\end{aligned}
\tag{59}
$$

The second-order moments of $\dot{\mathbf{e}}^{vp}$ given by (55) is expanded as:

$$
\left\langle \dot{\mathbf{e}}^{vp} : \dot{\mathbf{e}}^{vp} \right\rangle_r = \frac{1}{(\Delta t)^2} \left(\left\langle \mathbf{e}^{vp} : \mathbf{e}^{vp} \right\rangle_r - 2 \left\langle \mathbf{e}^{vp} : \mathbf{e}_n^{vp} \right\rangle_r + \left\langle \mathbf{e}_n^{vp} : \mathbf{e}_n^{vp} \right\rangle_r \right) \tag{60}
$$

However, the expression (60) cannot be evaluated duo to the inaccessibility of the term $\left\langle \mathbf{e}^{vp} : \mathbf{e}_n^{vp} \right\rangle_r$. Thanks to the stationarity of ΔJ over $\mathbf{e}^{vp}$, the $\mathbf{e}^{vp}$ in (55) will be replaced by the right hand side of (42). Thus, the relation (55) can be reset as:

$$\left\langle \dot{\mathbf{e}}^{vp} : \dot{\mathbf{e}}^{vp} \right\rangle_r = \left[\frac{\theta^{(r)}}{\Delta t\left(1-\theta^{(r)}\right)} \right]^2 \left[\left\langle \left(\mathbf{e}_n^{vp} - \mathbf{e}_0^{(r)} \right) : \left(\mathbf{e}_n^{vp} - \mathbf{e}_0^{(r)} \right) \right\rangle_r \right]$$
$$= \left[\frac{\theta^{(r)}}{\Delta t\left(1-\theta^{(r)}\right)} \right]^2 \left[\left\langle \mathbf{e}_n^{vp} : \mathbf{e}_n^{vp} \right\rangle_r - 2\left\langle \mathbf{e}_n^{vp} \right\rangle_r : \mathbf{e}_0^{(r)} + \mathbf{e}_0^{(r)} : \mathbf{e}_0^{(r)} \right] \tag{61}$$

Note that the quantities $\left\langle \mathbf{e}_n^{vp} : \mathbf{e}_n^{vp} \right\rangle_r$ are known from the previous step by relation (58). Through the expressions (57) and (61), the first and second-order moments of $\dot{\mathbf{e}}^{vp}$ can be obtained while the first- and second-order moments of $\boldsymbol{\varepsilon}$ (defined by $\left\langle \boldsymbol{\varepsilon} \right\rangle_r$ and $\left\langle \boldsymbol{\varepsilon} \otimes \boldsymbol{\varepsilon} \right\rangle_r$, respectively) are unknown.

5.4.3 Determination of the first- and second-order moments of $\boldsymbol{\varepsilon}$

The first moments of the strain field $\boldsymbol{\varepsilon}$ in each phase of a linear thermoelastic composite can be expressed as (Willis, 1981)

$$\left\langle \boldsymbol{\varepsilon} \right\rangle_r = \mathbb{A}^{(r)} : \mathbf{E} + \mathbf{a}^{(r)} \tag{61}$$

$\mathbb{A}^{(r)}$, $\mathbf{a}^{(r)}$ are the classical localization tensor determined according to the homogenization scheme used in the thermoelastic composite. Both tensors depend on the effective elastic moduli of the phases and on the microstructure of the composite. Explicit expressions corresponding to specific microstructures can be found in the literature. These tensors can also be evaluated numerically.

The second moment of the strain field in (59) is obtained by the derivation of the effective energy of the composite with respect to the effective elastic moduli $\mathbb{L}_{eff}^{(r)}$ of the individual phases (Ponte Castañeda and Suquet, 1998; Buryachenko, 2001; Ponte Castañeda, 2002):

$$\left\langle \boldsymbol{\varepsilon} \otimes \boldsymbol{\varepsilon} \right\rangle_r = \frac{2}{c^{(r)}} \frac{\partial \tilde{w}_0}{\partial \mathbb{L}_{eff}^{(r)}} \tag{62}$$

where $\mathbb{L}_{eff}^{(r)}$ is obtained by (48) and can be expressed by two effective moduli as $\mathbb{L}_{eff}^{(r)} = 3k_{eff}^{(r)}\mathbb{J} + 2\mu_{eff}^{(r)}\mathbb{K} = 3k^{(r)}\mathbb{J} + 2\mu_{eff}^{(r)}\mathbb{K}$. The partial derivative in (62) can be solved by several approaches such as the analytical derivation (Bobeth and Diener, 1987; Kreher, 1990), approximate evaluation by finite differences (Bilger and al., 2002) or

an efficient semi-analytical procedure (Renald Brenner, Olivier Castelnau and Lori Badea, 2004). Nevertheless, the above mentioned methods are quite complex to perform. Actually, for evaluating the expression (59), we need the projection of the second moment over $\mathbb{K}$ rather than the second moment itself. This projection can be given by derivation of the effective energy with respect to $\mu_{eff}^{(r)}$:

$$\mathbb{K} :: \left\langle \boldsymbol{\varepsilon} \otimes \boldsymbol{\varepsilon} \right\rangle_r = \frac{1}{c^{(r)}} \frac{\partial \tilde{w}_0}{\partial \mu_{eff}^{(r)}} = \frac{1}{c_0} \left(\frac{1}{2} \mathbf{E}_{n+1} : \frac{\partial \tilde{\mathbb{L}}}{\partial \mu_{eff}^{(0)}} : \mathbf{E}_{n+1} + \frac{\partial \tilde{\boldsymbol{\rho}}}{\partial \mu_{eff}^{(0)}} : \mathbf{E}_{n+1} + \frac{\partial \tilde{f}}{\partial \mu_{eff}^{(0)}} \right) \quad (63)$$

We note that $\mu_{eff}^{(r)}$ is a scalar variable. Thus the partial derivative (63) can be easily solved when the detailed expressions for the effective energy $\tilde{w}_0(\mathbf{E})$ are given (see Appendix B).

5.5 Numerical implementation

5.5.1 Computational procedure

The numerical integration scheme for determining the macroscopic response ($\boldsymbol{\Sigma}_{n+1}$) of the composite will be given in this subsection. To facilitate further numerical applications, this integration is realized directly at each Gauss point in the framework of finite elements method through the standard code (Abaqus).

The composite is submitted at t_{n+1} to an uniform macroscopic strain $\mathbf{E}_{n+1} = \mathbf{E}_n + \Delta\mathbf{E}$ with the given strain increment $\Delta\mathbf{E}$.

The computational procedure can be summarized as follows:

1. At time t_n, the first moment $\left\langle \mathbf{e}^{vp} \right\rangle_r$ and the second moment $\left\langle \mathbf{e}^{vp} : \mathbf{e}^{vp} \right\rangle_r$ are known for each individual phase r;
2. Given a macroscopic strain increment: $\Delta\mathbf{E}$ and $\mathbf{E}_{n+1} = \mathbf{E}_n + \Delta\mathbf{E}$;
3. Trial elastic prediction: $\boldsymbol{\sigma}_{n+1}^{(r)} = \mathbb{L}^{(r)} : \left(\boldsymbol{\varepsilon}_{n+1}^{(r)} - \left\langle \mathbf{e}_n^{vp} \right\rangle_r - \left(\boldsymbol{\varepsilon}_m^{vp} \right)_n \right)$;
4. Check of $\left(\sigma_{eq} - R^{(r)} \right)^+$;
5. If $\left(\sigma_{eq} - R^{(r)} \right)$ is positive, then go to (6); Else, evaluate the macroscopic stress through the classical elastic homogenization method;
6. Initialize $\left(\eta_{sct}^{(r)} \right)_i$ and $\left(\theta^{(r)} \right)_i$;

7. Solving of the nonlinear equation (45) for $\left(\mathbf{e}_0^{(r)}\right)_i$;

8. Once $\left(\eta_{sct}^{(r)}\right)_i$, $\left(\theta^{(r)}\right)_i$ and $\left(\mathbf{e}_0^{(r)}\right)_i$ are given, the linear thermoelastic composite is known from (48). Then through the expressions (61) and (63), the first and second moments of the strain in the thermoelastic composite are evaluated;

9. Calculate the first moment $\left(\left\langle \mathbf{e}^{vp} \right\rangle_r\right)_{i+1}$ and the second moment $\left(\left\langle \mathbf{e}^{vp} : \mathbf{e}^{vp} \right\rangle_r\right)_{i+1}$ by means of relations (57) and (58) from the first and second moments of the strain $\boldsymbol{\varepsilon}$ obtained at the step 8;

10. With the results at the step 9, the secant viscosity $\left(\eta_{sct}^{(r)}\right)_{i+1}$ is known from (53) and the scaling factor $\left(\theta^{(r)}\right)_{i+1}$ is known from (44);

11. Calculate the residues $R_1 = \left(\eta_{sct}^{(r)}\right)_{i+1} - \left(\eta_{sct}^{(r)}\right)_i$ and $R_2 = \left(\theta^{(r)}\right)_{i+1} - \left(\theta^{(r)}\right)_i$

if $|R_1| < tolerance$ and $|R_2| < tolerance$, go to the next step; Else, $i = i+1$ and return to the step 8;

12. After the convergence is reached, the macroscopic stress at t_{n+1} can be obtained as the stress in the thermoelastic composite by taking the average of the microscopic stress field:

$$\boldsymbol{\Sigma}_{n+1} = \left\langle \boldsymbol{\sigma}_{n+1} \right\rangle = \sum_{r=1}^{N} c^{(r)} \left[\mathbb{L}_{eff}^{(r)} : \left\langle \boldsymbol{\varepsilon} \right\rangle_r + \boldsymbol{\rho}_{eff}^{(r)} \right]$$

5.5.2 Comparison with a reference solution given by finite element method (FEM)

For a first evaluation of the variational approach, we present in this section some comparisons of its predictions with a reference solution obtained by direct finite element simulations. For obvious reasons of relevance of the comparison, the parameters used in this variational approach and finite element calculations are chosen as the same.

The FEM solution is obtained by considering a unit cell. As shown in the Figure 1, the matrix is composed of hexagonal prisms and each prism is reinforced by a spherical inclusion at its center. This 3-dimensional unit cell is approximated by a cylindrical cell which can be solved in the axisymmetric condition (Fig 1. (a)).

The boundary conditions in the plane $r \sim z$ are:

- $\mathbf{U}_3(r,0)=0,\ \ 0<r<R$,
- $\mathbf{U}_3(r,L)=\vec{U}_3,\ \ 0<r<R$,
- $\mathbf{U}_1(0,z)=0,\ \ 0<z<L$,
- $\mathbf{U}_1(R,z)=\vec{U}_1,\ \ 0<z<L$.

The displacement $\vec{\mathbf{U}}_3$ is prescribed gradually over time ($10^{-2}/s$) to reach the required deformation at the end of the simulation. The unit cell (Fig 1. (b)), used in the simulation, has 15% of reinforcements and 963 CAX8R (8-node biquadratic axisymmetric quadrilateral, reduced integration) elements and contains 3002 nodes.

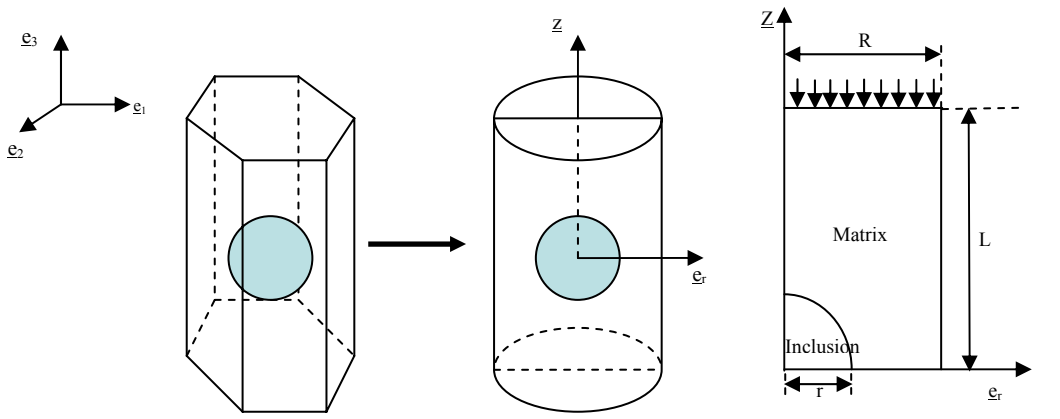

(a) (b)

Fig 1. (a) 3 dimensional unit cell approximated by cylindrical one, (b) 2D axisymmetric unit cell used in the simulation

The inclusion is a linearly elastic material, whereas the matrix is a viscoplastic material with a power-law dissipative potential under the form (33). The behaviors of the matrix and inclusion are described by the following parameters respectively:

Matrix: $E=3000\text{MPa}$, $v=0.2$, $\sigma_0=14\text{MPa}$, $\dot{\varepsilon}_0=0.0028$, $m=0.8$, $\beta=1.06$, $b=3000$;

Inclusion: $E=100000\text{MPa}$, $v=0.2$.

In Figure 2, we present comparisons between the results obtained respectively by the incremental variationnel method and FEM solution for a uniaxial compression test. There is globally an agreement between the two results. However, some scatters are observed for higher values of axial strain.

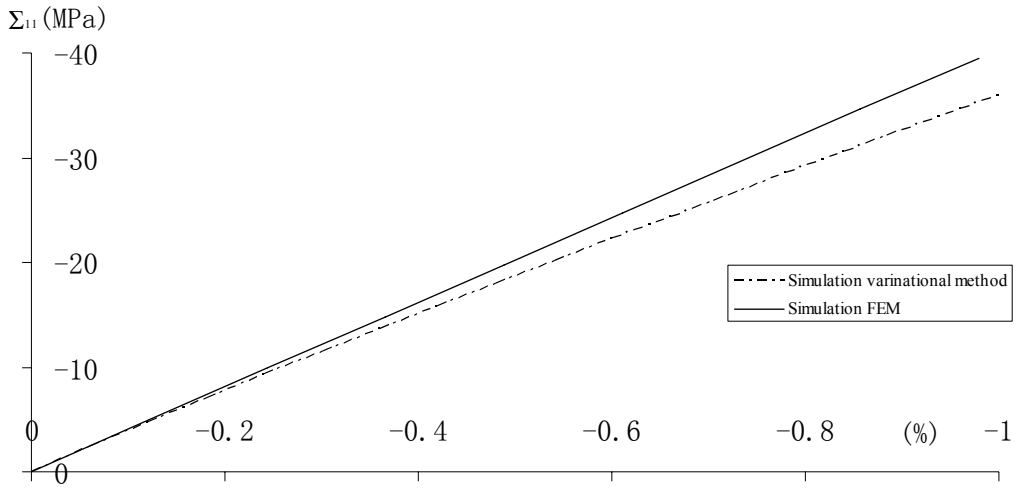

Fig 2: Uniaxial compression test - comparison between the variational method and reference solution obtained by FEM

5.6 Numerical simulation of laboratory tests for COX argillite

Instantaneous behavior

In this part, the proposed variationnel model is used for the simulation of uniaxial and triaxial compression tests on COX argillites with different mineral composition The identification of parameters for the local plastic and elastic properties has been performed always using an iterative optimization procedure by numerical fitting from uniaxial compression test performed on a specific specimen (EST 104 02262-1). The obtained values issued from this procedure are as follows:

Matrix: $E = 3000\text{MPa}$, $v = 0.2$, $\sigma_0 = 14\text{MPa}$, $\dot{\varepsilon}_0 = 0.02$, $m = 0.8$, $\beta = 1.06$, $b = 3000$;

Inclusions (average value of calcite and quartz): $E = 100000\text{MPa}$, $v = 0.2$.

Representative numerical results are presented in Fig. 3. We can see that the numerical results are generally in good agreement with experimental data. The proposed model seems to correctly reproduce the main features of the Callovo-Oxfordian argillite behavior such as the volumetric dilatancy and confining pressure sensitivity. At the same time, the hardening behavior and impact of mineral compositions are also well predicted.

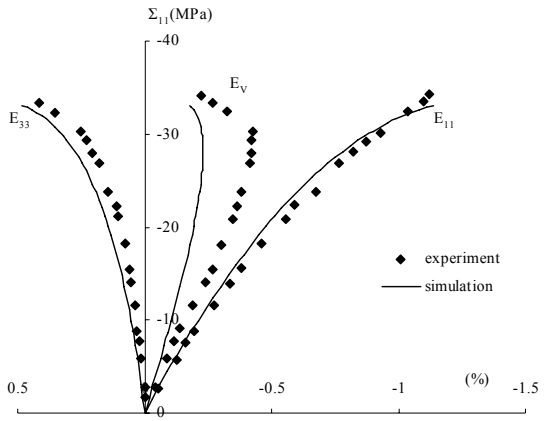

(a) Depth 466.8m, $f_m = 51\%$, $f_i = 49\%$. Uniaxial compression (EST 104 02262-12)

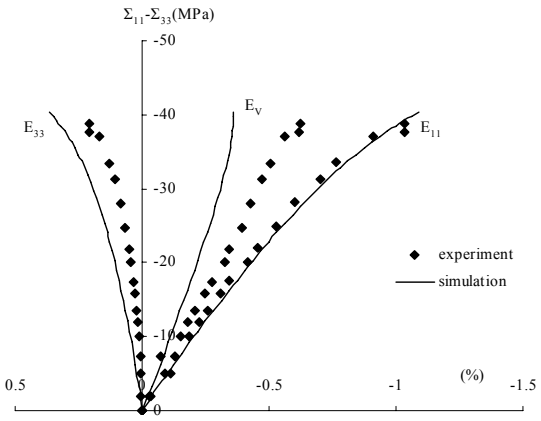

(b) Depth 451.5m, $f_m = 49\%$, $f_i = 51\%$. Triaxial compression, $\sigma_c = 5MPa$, (EST 104 02172-32)

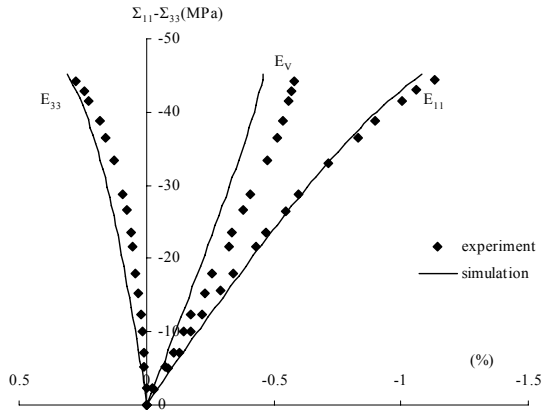

(c) Depth 451.4m, $f_m = 47\%$, $f_i = 53\%$. Triaxial compression, $\sigma_c = 10MPa$ (EST 104 02172-22)

Fig 3: Comparison between experimental data and simulation

Creep behavior

For the simulation of time-dependent responses, we have used the following values of parameters:

Matrix: $E = 3000\text{MPa}$, $v = 0.2$, $\sigma_0 = 14\text{MPa}$, $\dot{\varepsilon}_0 = 0.01$, $m = 0.06$, $\beta = 1.06$, $b = 3000$;

Inclusions: $E = 100000\text{MPa}$, $v = 0.2$.

In Fig. 4, we present the evolutions of axial strain during three triaxial creep tests with different stress levels for three argillite samples with different mineral compositions. One can see that the numerical results are in good agreement with experimental data. The proposed model is able to correctly capture time-dependent behaviors of the Callovo-Oxfordian argillite due to the viscoplasticity of the clay matrix. The influences of mineral compositions are also well reproduced.

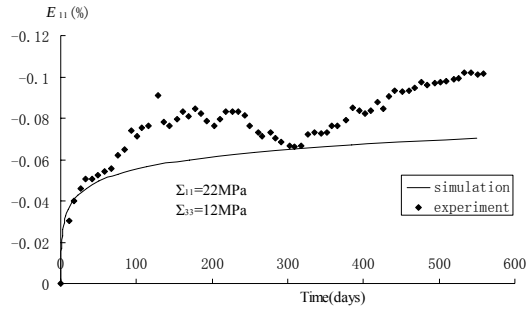

(a) Depth 497.8m, $f_m = 61\%$, $f_i = 39\%$

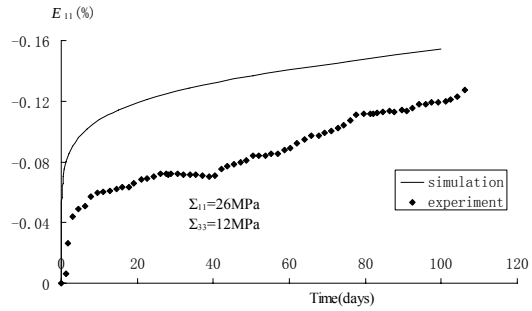

(b) Depth 491.8m, $f_m = 57\%$, $f_i = 43\%$

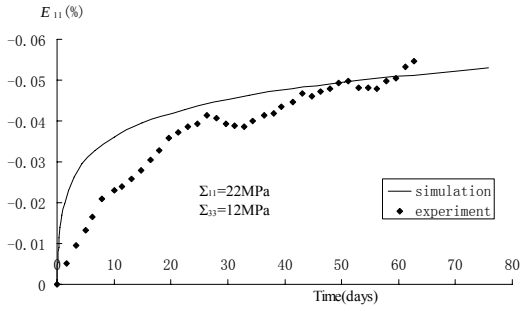

(c) Depth 492.1m, $f_m = 56.9\%$, $f_i = 43.1\%$.

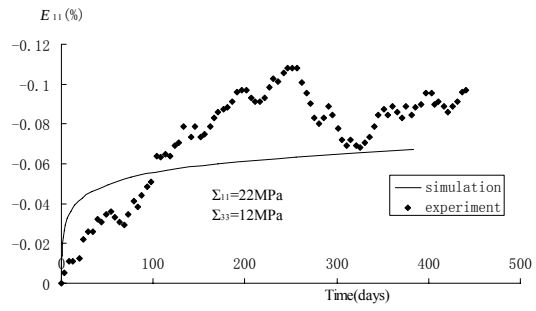

(d) Depth 491.8m, $f_m = 57\%$, $f_i = 43\%$.

Fig 4: Comparison between numerical results and experimental data in creep tests

5.7 Conclusion

The objective of this chapter is to propose a micromechanical model taking into account the heterogeneity of local stain fields inside constituents of the Callovo-Oxfordian argillite. The proposed model is based on the incremental variational principles. The validity of this model is verified by comparisons with finite element computation on a unit cell. The experimental validation is also performed through the comparison with experimental data on uniaxial and triaxial compression tests performed on samples with different mineralogical compositions. It is shown that the model is able to describe the main features of the argillite mechanical behaviors. In the last part of present chapter, the numerical results are compared with experimental data in creep tests under different stress levels. The proposed model correctly reproduces the effects of stress level and mineral compositions.

Appendix A: The effective tensors for the viscoplastic constituents

As a matter of convenience, in this section, the superscript (r) of the variables is omitted and η_{sct} is denoted by η. The expression (36) is expanded as:

$$\begin{aligned} J_0\left(\boldsymbol{\varepsilon}_{n+1}, \mathbf{e}^{vp}_{n+1}\right) = \frac{1}{2}\left(\boldsymbol{\varepsilon}_{n+1} - \mathbf{e}^{vp}_{n+1} - \left(\boldsymbol{\varepsilon}^{vp}_{m}\right)_{n+1}\right) :: \mathbb{L} : \left(\boldsymbol{\varepsilon}_{n+1} - \mathbf{e}^{vp}_{n+1} - \left(\boldsymbol{\varepsilon}^{vp}_{m}\right)_{n+1}\right) \\ + w^{\gamma}\left(\gamma^{vp}_{n+1}\right) + \frac{\eta\theta}{\Delta t}\mathbf{e}^{vp}_{n+1} : \mathbf{e}^{vp}_{n+1} - \frac{2\eta\theta}{\Delta t}\mathbf{e}^{vp}_{n+1} : \mathbf{e}_0 + \frac{\eta\theta}{\Delta t}\mathbf{e}_0 : \mathbf{e}_0 \end{aligned} \tag{A.1}$$

where the first term of the right hand side reads as:

$$\begin{aligned} &\left(\boldsymbol{\varepsilon}_{n+1} - \mathbf{e}^{vp}_{n+1} - \left(\boldsymbol{\varepsilon}^{vp}_{m}\right)_{n+1}\right) :: \mathbb{L} : \left(\boldsymbol{\varepsilon}_{n+1} - \mathbf{e}^{vp}_{n+1} - \left(\boldsymbol{\varepsilon}^{vp}_{m}\right)_{n+1}\right) = \\ &\qquad \boldsymbol{\varepsilon}_{n+1} :: \mathbb{L} : \boldsymbol{\varepsilon}_{n+1} + \mathbf{e}^{vp}_{n+1} :: \mathbb{L} : \mathbf{e}^{vp}_{n+1} + \left(\boldsymbol{\varepsilon}^{vp}_{m}\right)_{n+1} :: \mathbb{L} : \left(\boldsymbol{\varepsilon}^{vp}_{m}\right)_{n+1} \\ &\qquad - 2\boldsymbol{\varepsilon}_{n+1} :: \mathbb{L} : \mathbf{e}^{vp}_{n+1} - 2\mathbf{e}^{vp}_{n+1} :: \mathbb{L} : \left(\boldsymbol{\varepsilon}^{vp}_{m}\right)_{n+1} - 2\boldsymbol{\varepsilon}_{n+1} :: \mathbb{L} : \left(\boldsymbol{\varepsilon}^{vp}_{m}\right)_{n+1} \end{aligned} \tag{A.2}$$

Substituting (46) into (A.1) obtains the follow expressions:

i) the 2nd term in (A.2):

$$\begin{aligned} \mathbf{e}^{vp}_{n+1} :: \mathbb{L} : \mathbf{e}^{vp}_{n+1} = \boldsymbol{\varepsilon}_{n+1} : \mathbb{L} : \mathbb{K} : \left(\frac{2\eta\theta}{\Delta t}K + \mathbb{L}\right)^{-1} : \mathbb{L} : \left(\frac{2\eta\theta}{\Delta t}\mathbb{K} + \mathbb{L}\right)^{-1} : \mathbb{K} : \mathbb{L} : \boldsymbol{\varepsilon}_{n+1} \\ + 2\boldsymbol{\varepsilon}_{n+1} : \mathbb{L} : \mathbb{K} : \left(\frac{2\eta\theta}{\Delta t}\mathbb{K} + L\right)^{-1} : \mathbb{L} : \left(\frac{2\eta\theta}{\Delta t}\mathbb{K} + \mathbb{L}\right)^{-1} : \frac{2\eta\theta}{\Delta t}\mathbf{e}_0 , \\ + \left(\frac{2\eta\theta}{\Delta t}\right)^2 \mathbf{e}_0 : \left(\frac{2\eta\theta}{\Delta t}\mathbb{K} + \mathbb{L}\right)^{-1} : \mathbb{L} : \left(\frac{2\eta\theta}{\Delta t}\mathbb{K} + \mathbb{L}\right)^{-1} : \mathbf{e}_0 \end{aligned}$$

ii) the 4th term in (A.2):

$$\boldsymbol{\varepsilon}_{n+1} : \mathbb{L} : \mathbf{e}_{n+1}^{vp} = \boldsymbol{\varepsilon}_{n+1} : \mathbb{L} : \mathbb{K} : \left(\frac{2\eta\theta}{\Delta t}\mathbb{K} + \mathbb{L} \right)^{-1} : \mathbb{K} : \mathbb{L} : \boldsymbol{\varepsilon}_{n+1} + \frac{2\eta\theta}{\Delta t}\boldsymbol{\varepsilon}_{n+1} : \mathbb{L} : \left(\frac{2\eta\theta}{\Delta t}\mathbb{K} + \mathbb{L} \right)^{-1} : \mathbf{e}_0$$

iii) the 3rd term in (A.1):

$$\begin{aligned} \mathbf{e}_{n+1}^{vp} : \mathbf{e}_{n+1}^{vp} = {} & \boldsymbol{\varepsilon}_{n+1} : \mathbb{L} : \mathbb{K} : \left(\frac{2\eta\theta}{\Delta t}\mathbb{K} + \mathbb{L} \right)^{-1} : \left(\frac{2\eta\theta}{\Delta t}\mathbb{K} + \mathbb{L} \right)^{-1} : \mathbb{K} : \mathbb{L} : \boldsymbol{\varepsilon}_{n+1} \\ & + 2\boldsymbol{\varepsilon}_{n+1} : \mathbb{K} : \left(\frac{2\eta\theta}{\Delta t}\mathbb{K} + \mathbb{L} \right)^{-1} : \left(\frac{2\eta\theta}{\Delta t}\mathbb{K} + \mathbb{L} \right)^{-1} : \frac{2\eta\theta}{\Delta t}\mathbf{e}_0 , \\ & + \left(\frac{2\eta\theta}{\Delta t} \right)^2 \mathbf{e}_0 : \left(\frac{2\eta\theta}{\Delta t}\mathbb{K} + \mathbb{L} \right)^{-1} : \left(\frac{2\eta\theta}{\Delta t}\mathbb{K} + \mathbb{L} \right)^{-1} : \mathbf{e}_0 \end{aligned}$$

iiii) the 4th term in (A.1):

$$\mathbf{e}_{n+1}^{vp} : \mathbf{e}_0 = \boldsymbol{\varepsilon}_{n+1} : \mathbb{L} : \mathbb{K} : \left(\frac{2\eta\theta}{\Delta t}\mathbb{K} + \mathbb{L} \right)^{-1} : \mathbf{e}_0 + \frac{2\eta\theta}{\Delta t}\mathbf{e}_0 : \left(\frac{2\eta\theta}{\Delta t}\mathbb{K} + \mathbb{L} \right)^{-1} : \mathbf{e}_0 .$$

Re-arranging these expressions in terms of ε_{n+1} and remarking that,

$$\left(\frac{2\eta\theta}{\Delta t}\mathbb{K} + \mathbb{L} \right)^{-1} = \left(\frac{2\eta\theta}{\Delta t}\mathbb{K} + 3k\mathbb{J} + 2\mu\mathbb{K} \right)^{-1} = \frac{1}{3k} J + \frac{1}{\frac{2\eta\theta}{\Delta t} + 2\mu}\mathbb{K} \qquad \text{(A.3)}$$

We obtain:

$$\begin{aligned} \boldsymbol{\varepsilon}_{n+1} : \Bigg[& \frac{2\eta\theta}{\Delta t}\mathbb{L} : \mathbb{K} : \left(\frac{2\eta\theta}{\Delta t}\mathbb{K} + \mathbb{L} \right)^{-1} : \mathbb{L} : \left(\frac{2\eta\theta}{\Delta t}\mathbb{K} + \mathbb{L} \right)^{-1} : \mathbf{e}_0 \\ & + \frac{2\eta\theta}{\Delta t}\mathbb{K} : \left(\frac{2\eta\theta}{\Delta t}\mathbb{K} + \mathbb{L} \right)^{-1} : \left(\frac{2\eta\theta}{\Delta t}\mathbb{K} + \mathbb{L} \right)^{-1} : \frac{2\eta\theta}{\Delta t}\mathbf{e}_0 - \frac{2\eta\theta}{\Delta t}\mathbb{L} : \mathbb{K} : \left(\frac{2\eta\theta}{\Delta t}\mathbb{K} + \mathbb{L} \right)^{-1} : \mathbf{e}_0 \Bigg] = 0 \end{aligned} \qquad \text{(A.4)}$$

$$\boldsymbol{\varepsilon}_{n+1} : \left[\frac{1}{2}\mathbb{L} : \mathbb{K} : \left(\frac{2\eta\theta}{\Delta t}\mathbb{K} + \mathbb{L} \right)^{-1} : \mathbb{L} : \left(\frac{2\eta\theta}{\Delta t}\mathbb{K} + \mathbb{L} \right)^{-1} : \mathbb{K} : \mathbb{L} - \mathbb{L} : \mathbb{K} : \left(\frac{2\eta\theta}{\Delta t}K + \mathbb{L} \right)^{-1} : \mathbb{K} : \mathbb{L} \right.$$
$$\left. + \frac{\eta\theta}{\Delta t}\mathbb{L} : \mathbb{K} : \left(\frac{2\eta\theta}{\Delta t}\mathbb{K} + \mathbb{L} \right)^{-1} : \left(\frac{2\eta\theta}{\Delta t}\mathbb{K} + \mathbb{L} \right)^{-1} : \mathbb{K} : \mathbb{L} \right] : \boldsymbol{\varepsilon}_{n+1}$$
$$= \boldsymbol{\varepsilon}_{n+1} : \left[-\frac{1}{2}\mathbb{L} : \mathbb{K} : \left(\frac{2\eta\theta}{\Delta t}K + \mathbb{L} \right)^{-1} : \mathbb{K} : \mathbb{L} \right] : \boldsymbol{\varepsilon}_{n+1} \tag{A.5}$$

As the result of the expression (A.4) and (A.5), the tensors $\mathbb{L}_{eff}^{(r)}$, $\boldsymbol{\rho}_{eff}^{(r)}$ and $\beta_{eff}^{(r)}$ will be obtained.

Appendix B: Effective energy for N-phase and two-phase composites

Consider an N-phase thermoelastic composite whose phase r is characterized by the sole energy:

$$w^{(r)}(\boldsymbol{\varepsilon}) = \frac{1}{2}\boldsymbol{\varepsilon} : \mathbb{L}_{eff}^{(r)} : \boldsymbol{\varepsilon} + \boldsymbol{\rho}_{eff}^{(r)} : \boldsymbol{\varepsilon} + \beta_{eff}^{(r)}$$

Its effective energy is defined by (Willis, 1981):

$$\tilde{w}(\mathbf{E}) = \frac{1}{2}\mathbf{E} : \tilde{\mathbb{L}}_{eff} : \mathbf{E} + \tilde{\boldsymbol{\rho}}_{eff} : \mathbf{E} + \tilde{\beta}_{eff} \tag{B.1}$$

where

$$\tilde{\mathbb{L}}_{eff} = \left\langle \mathbb{L}_{eff} \right\rangle + \sum_{r=1}^{N-1} c^{(r)} \left(\mathbb{L}_{eff}^{(r)} - \mathbb{L}_{eff}^{(N)} \right) : \left(\mathbb{A}^{(r)} - \mathbb{I} \right), \tag{B.2}$$

$$\tilde{\boldsymbol{\rho}}_{eff} = \left\langle \boldsymbol{\rho}_{eff} \right\rangle + \sum_{r=1}^{N-1} c^{(r)} \left(\mathbb{A}^{(r)} - \mathbb{I} \right)^{T} : \left(\boldsymbol{\rho}_{eff}^{(r)} - \boldsymbol{\rho}_{eff}^{(N)} \right), \tag{B.3}$$

$$\tilde{\beta}_{eff} = -\frac{1}{2}\left(\left\langle \beta_{eff} \right\rangle + \sum_{r=1}^{N-1} c^{(r)} \left(\boldsymbol{\rho}_{eff}^{(r)} - \boldsymbol{\rho}_{eff}^{(N)} \right) : \mathbf{a}^{(r)} \right). \tag{B.4}$$

These expressions simplify further for two-phase composites (N=2). According to Levin's (1967) remarkable relations, the localization operators can be explicitly expressed in terms of the effective stiffness $\tilde{\mathbb{L}}_{eff}$ (given by the homogenization scheme used) of the composite:

$$\mathbb{A}^{(1)} = \mathbb{I} + \frac{1}{c^{(1)}}\left(\mathbb{L}_{eff}^{(1)} - \mathbb{L}_{eff}^{(2)} \right)^{-T} : \left(\tilde{\mathbb{L}}_{eff} - \left\langle \mathbb{L}_{eff} \right\rangle \right)^{T} \tag{B.5}$$

$$\mathbf{a}^{(1)} = -\frac{1}{c^{(1)}}\left(\mathbb{L}_{eff}^{(1)} - \mathbb{L}_{eff}^{(2)}\right)^{-1} : \left(\tilde{\mathbb{L}}_{eff} - \left\langle \mathbb{L}_{eff} \right\rangle\right) : \left(\mathbb{L}_{eff}^{(1)} - \mathbb{L}_{eff}^{(2)}\right)^{-1} : \left(\boldsymbol{\rho}_{eff}^{(1)} - \boldsymbol{\rho}_{eff}^{(2)}\right) \quad \text{(B.6)}$$

Substituting (B.5) and (B.6) into (B.3) and (B.4) obtains the follow expressions:

$$\tilde{\boldsymbol{\rho}}_{eff} = \left\langle \boldsymbol{\rho}_{eff} \right\rangle + \left(\tilde{\mathbb{L}}_{eff} - \left\langle \mathbb{L}_{eff} \right\rangle\right) : \left(\mathbb{L}_{eff}^{(1)} - \mathbb{L}_{eff}^{(2)}\right)^{-1} : \left(\boldsymbol{\rho}_{eff}^{(1)} - \boldsymbol{\rho}_{eff}^{(2)}\right) \quad \text{(B.7)}$$

$$\begin{aligned} \tilde{\beta}_{eff} = -\frac{1}{2}\Big(&\left\langle \beta_{eff} \right\rangle \\ &-\left(\boldsymbol{\rho}_{eff}^{(1)} - \boldsymbol{\rho}_{eff}^{(2)}\right) : \left(\mathbb{L}_{eff}^{(1)} - \mathbb{L}_{eff}^{(2)}\right)^{-1} : \left(\tilde{\mathbb{L}}_{eff} - \left\langle \mathbb{L}_{eff} \right\rangle\right) : \left(\mathbb{L}_{eff}^{(1)} - \mathbb{L}_{eff}^{(2)}\right)^{-1} : \left(\boldsymbol{\rho}_{eff}^{(1)} - \boldsymbol{\rho}_{eff}^{(2)}\right)\Big) \end{aligned} \quad \text{(B.8)}$$

Conclusion générale et perspectives

Ce travail de thèse a consisté à étudier essentiellement le comportement mécanique différé des argilites du Callovo-Oxfordien par le moyen de modélisations multi-échelles. Nous avons considéré deux mécanismes différents de déformation différée: la déformation viscoplastique de la matrice argileuse et la propagation subcritique de microfissures. Nous avons proposé trois modèles micromécaniques, différents mais complémentaires, pour décrire ces deux mécanismes. Une première phase de validation a été effectuée pour chacun de ces modèles par rapport à des données expérimentales.

Afin de justifier le choix des approches multi-échelles adoptées, nous avons tout d'abord présenté, au premier chapitre, une analyse bibliographique succincte sur la microstructure et les compositions minéralogiques des argilites du Callovo-Oxfordien. Ces roches argileuses sont des matériaux hétérogènes constitués principalement de grains de quartz, de calcite et de minéraux argileux. La microstructure de ces roches est très complexe et nécessite une description multi-échelle. Cependant, à la première approximation et en vue des modélisations mécaniques, deux échelles paraissent être essentielles. A une échelle mésoscopique, ces argilites peuvent être approchées par une microstructure de type matrice/inclusion: les minéraux argileux constituent une matrice dans laquelle sont noyées des inclusions minérales de calcite et de quartz. A une échelle plus petite, soit microscopique, il est nécessaire de considérer la matrice argileuse comme un milieu poreux. Celui-ci est composé des particules d'argile constituant la phase solide et des pores inter-particules. Ces derniers représentent par ailleurs la majorité de la porosité connectée des argilites du COX. Il est donc essentiellement de prendre en compte les effets de la porosité de la matrice argileuse sur le comportement mécanique des argilites.

En ce qui concerne le comportement mécanique des phases. Il existe une forte contrasse entre les trois phases. Pour les gammes de sollicitations envisagées dans le contexte du stockage, les comportements des grains de calcite et de quartz peuvent être raisonnablement décrits par un modèle élastique linéaire. En revanche, le comportement mécanique de la matrice argileuse est clairement inélastique et susceptible à des déformations plastiques instantanée et différée et à l'endommagement par microfissuration. Par ailleurs, la matrice argileuse présente également une anisotropie structurale liée à une distribution orientée des particules d'argile. Enfin, les interfaces entre les inclusions minérales et la matrice argileuse

peuvent également jouer un rôle important dans le comportement mécanique et hydromécanique des argilites, notamment en ce qui concerne le mécanisme d'endommagement.

En se basant sur cette analyse de la microstructure et des mécanismes de déformations, nous avons présenté dans le chapitre 2 quelques outils de base de la micromécanique des milieux à microstructure aléatoire. Différents schémas d'estimation des propriétés élastiques (dilue, Mori-Tanaka, auto-cohérente) ainsi que des bornes de base (Voigt et Reuss, Hashin-Shtrikman) ont été rappelés. En ce qui concerne le comportement effectif non-linéaire, quelques approches ont également été résumées. Par rapport à la morphologie de matrice-inclusion des argilites, nous avons en particulier présenté l'approche incrémentale de Hill.

A partir du chapitre 3, nous avons proposé trois modèles micro-macro différents mais complémentaires pour décrire le comportement différé des argilites para rapport aux deux mécanismes principaux visés. Dans le chapitre 3, nous avons proposé un premier modèle micro-macro en considérant que la propagation subcritique de microfissures dans la matrice argileuse comme le seul mécanisme des déformations différées du matériau. La matrice argileuse a été alors modélisée par un modèle d'endommagement dépendant du temps. Ce modèle peut être utilisé pour décrire le comportement mécanique des argilites à moyen terme quand la déformation plastique peut être négligée, par exemple dans la zone proche des parois d'excavation.

Dans les chapitres 4 et 5, nous avons proposé deux modèles différents mais avec un point commun : la déformation viscoplastique de la matrice argileuse étant considérée comme le principal mécanisme du comportement différé des argilites. La différence entre les deux modèles réside dans la prise en compte des champs locaux à l'échelle mésoscopique. Au chapitre 4, nous avons proposé une modification de l'approche incrémentale de Hill pour le comportement différé des argilites. La matrice argileuse est décrite par une loi viscoplastique en tenant en compte des effets de la porosité inter-particulaire. Des lois d'écoulement associée et non-associée ont été envisagées et comparées. Par rapport aux travaux antérieurs, nous avons proposé d'utiliser un opérateur tangent élastoplastique asymptotique pour la détermination du tenseur incrémental d'Eshelby. Il a été clairement démontré que le modèle proposé décrit correctement les principaux aspects du comportement mécanique des argilites avec une loi d'écoulement non-associée. Cependant, ce type d'approche est basé sur l'hypothèse forte d'une distribution homogène des champs locaux qui sont

généralement fortement hétérogènes.

Par conséquent, dans le chapitre 5, nous avons proposé une adaptation de l'approche variationnelle incrémentale initialement proposée par Lahellec et Suquet pour des matériaux composites à la modélisation des argilites. Cette approche permet justement la prise en compte de l'hétérogénéité des champs locaux dans l'estimation des comportements non-linéaires des composites. L'adaptation a consisté à prendre en compte les spécificités du comportement mécanique des argilites comme la sensibilité à la pression de confinement et la transition contractance-dilatance volumique. La première phase de validation expérimentale a montré une réelle capacité de cette approche pour la modélisation des géomatériaux.

Les travaux en perspectives sont nombreux et peuvent concerner notamment les aspects suivants:

- Sur le plan de la modélisation, il s'avère nécessaire d'étendre les travaux effectués à la prise en compte d'autres phénomènes importants des argilites comme l'anisotropie structurale de la matrice argileuse et les effets d'interfaces entre inclusions et la matrice ;
- Il est aussi important de réaliser l'extension des modèles aux couplages thermo-hydromécaniques et chimiques, qui peuvent jouer un rôle crucial pour la sureté du stockage des déchets radioactifs ;
- Sur le plan expérimental, il convient de réaliser des essais en laboratoire à différentes échelles permettant d'identifier les mécanismes physiques supposés responsables de la déformation différée des roches argileuses. A titre d'exemple, il est nécessaire d'établir les liens physiques entre la vitesse de propagation subcritique de microfissures et l'endommagement différé du modèle proposé. Le modèle actuel ne permet pas de décrire directement la relation entre la condition de propagation locale et la vitesse de propagation de microfissure expérimentalement mesurée à l'échelle macroscopique.
- Il faut également compléter la phase de validation des différents modèles proposés par rapport à d'autres données expérimentales, notamment celles issues des expérimentations in situ dans le laboratoire souterrain de l'ANDRA.
- Enfin, il convient de tester les aptitudes des modèles à prédire les réponses des structures dans les conditions de sollicitations proches du contexte du stockage souterrain des déchets radioactifs.

Reference

Abou-Chakra Guéry, A., Cormery, F., Su, K., Shao, J.F., Kondo, D. A micromechanical model for the elasto-viscoplastic and damage behavior of a cohesive geomaterial. Physics and Chemistry of the Earth 33 (2008) S416–S421. 2008

Abou-Chakra Guery A, Cormery F, Shao JF, Kondo D. A micromechanical model of elastoplastic and damage behavior of a cohesive geomaterial. Int J Solids Struct; 45:1406–29. 2008

Abou-Chakra Guery A, Cormery F, Shao JF, Kondo D. A multiscale modeling of damage and time-dependent behavior of cohesive rocks. Int. J. for numerical and analytical methods in Geomechanics; 33:567-589 2009

Anderson OL, Grew PC. Stress corrosion theory of crack propagation with application to geophysics. Rev. Geophys. Space Phys.; 15:77-104. 1977

Andra. Référentiel du site Meuse-Haute Marne. Scientific Report (in French), 2005

Atkinson BK. Fracture toughness of Tennessee sandstone and Carrara marble using the double torsion testing method. Int. J. Rock Mech Min Sci Geomech Abstr; 16:46-53. 1979

Atkinson BK. Subcritical crack propagation in rocks: theory, experimental results and applications. J. Struct. Geol.; 4:41–56. 1982

Atkinson BK. Subcritical crack growth in geological materials. J. Geophys. Res; 89:4077-4114. . 1984

Bilger, N., Auslender, F., Bornert, M. & Masson, R. New bounds and estimates for porous media with rigid perfectly plastic matrix. C. R. Mecanique 330, 127 – 132. 2002

Bobeth, M. & Diener, G.. Static and thermoelastic field fluctuations in multiphase composites. J. Mech. Phys. Solids 35, 137 – 149. 1987

Bornert M, Vales F, Gharbi H, Nguyen Minh D. Multiscale full-field strain measurements for micromechanical investigations of the hydromechanical behaviour of clayey rocks. Strain; 46:33–46. 2010

Budiansky, B., O'Connell, RJ. Elastic moduli of a cracked solid, International Journal of Solids and Structures 12, 81-97; 1976

Buryachenko, V. Multiparticle effective field and related methods in micromechanics of composite materials. Appl. Mech. Rev. 54, 1 – 47. 2001

Chaboche, J.L, Continuous damage mechanics – A tool to describe phenomena before crack initiation, Nuclear Engineering and Design 64, 233-247. 1981

Chaboche, J., Kruch, S., Maire, J., Pottier, T. Towards a micromechanics based inelastic and damage modeling of composites. Int. J. Plasticity 17, 411 – 439.

2001.

Chaboche, J.L., Kanouté, P. Sur les approximations « isotrope » et « anisotrope » de l'opérateur tangent pour les méthodes tangentes incrémentale et affine. C.R. Mecanique, 331(12):857-864. 2003

Chan, K. S., Bodner, S. R., Fossum, A. F. and Munson D. E. A Damage Mechanics Treatment of Creep Failure in Rock Salt, International Journal of Damage Mechanics 6(2), 121-152. 1997

Chau, K. T. and Wong R.H. C. Effective Moduli of Microcracked Rocks: Theories and Experiments, International Journal of Damage Mechanics 6(3), 258-277. 1997

Chen L., Duveau G. and Shao J.F. Modelling of plastic deformation and damage in cement-based material subjected to desiccation, International journal for numerical and analytical methods in Geomechanics 35, 1877-1898. 2011

Chew HB, Guo TF, Cheng L. Effects of pressure-sensitivity and plastic dilatancy on void growth and interaction. Int J Solids Struct 43. 2006

Chiarelli AS, Shao JF, Hoteit N. Modeling of elastoplastic damage behaviour of a claystone. Int. J. Plasticity;19:23–45. 2003

Ciccotti M, Gonzato G, Mulargia F. The double torsion loading configuration for fracture propagation: an improved methodology for the load-relaxation at constant displacement, International Journal of Rock Mechanics & Mining Sciences; 37:1103-1113; 2000

Ciccotti M, Negri N, Gonzato G, Mulargia F. Practical application of an improved methodology for the double torsion load relaxation method, International Journal of Rock Mechanics & Mining Sciences; 38:569–576. 2001

Comi, C., Perego, U. Anisotropic Damage Model for Concrete Affected by Alkali-Aggregate Reaction, International Journal of Damage Mechanics 20, 598-617. 2011

Drucker, D.-C., Prager, W., Soil mechanics and plastic analysis or limit design. Quartely of appl. Math. 10, 157-175. 1952

Doghri, I., Ouaar, A. homogenization of two-phase elastoplastic composite materials and structures: Study of tangent operators, cyclic plasticity and numerical algorithms. Int. J. Solids Struct., 40(7):1681-1712. 2003

Eshelby, J. The determination of the elastic field of an ellipsoidal inclusion and related problems, Proc. R. Soc. London A. 241, 375–396. 1957

Gurson, A., Continuum theory of ductile rupture by void nucleation and growth: part1-yield criteria and flow rules for porous ductile media. J Engrg. Mater. Technol. 99, 2-15. 1977

Halm, D., Dragon, A. A model of anisotropic damage by mesocrack growth: unilateral

effect. Int. J. Damage Mech. 5, 384-402. 1996

Hashin, Z. and Shtrikman, S., On some variational principlrd in anisotropic and nonhomogeneous elasticity. Journal of Mechanics and Physics of Solids, 10, pp. 335-342. 1962

Hayakawa, K. and Murakami, S. Thermodynamical modeling of elastic-plastic damage and experimental validation of damage potential, Int. J. Damage Mech. 6, 333-363. 1997

Henry JP, Paquet J, Tancrez JP. Experimental study of crack propagation in calcite rocks. Int. J. Rock Mech Min Sci Geomech Abstr; 14:85-91. 1977

Hill, R., Continuum micro-mechanics of elastoplastic polycrystals. J.Mech.Phys.Solids 13, 89-101. 1965a.

Hill, R., A self-consistent mechanics of composite materials. J.Mech.Phys.Solids 13, 213-222. 1965b.

Ju, J.W. On energy based coupled elastoplastic damage theories: constitutive modeling and computational aspects, Int. J. Solids Structures 25(7), 803-833. 1989

Ju JW, Yuan KY, Kuo AW. Novel strain energy based coupled elastoplastic damage and healing models for geomaterials – Part I: formulations, Int. J. of damage Mechanics 21, 525- 549. 2012

Kreher, W. Residual stresses and stored elastic energy of composites and polycrystals. J. Mech. Phys. Solids 38, 115 – 128. 1990

Lahellec, N., Suquet, P. Effective behavior of linear viscoelastic composites: a time-integration approach. Int. J. Solids Struct. 44, 507 – 529. 2006.

Lahellec, N., Suquet P. On the effective behaviour of nonlinear inelastic composites: I. Incremental variational principles. J. Mech. Phys. Solids 55 1960 P1932–1963. 2007

Lebon P., Mouroux B. Knowledge of the three French underground laboratory sites, Engineering Geology 52, 251-256. 1999

Lemaitre, J. How to use damage mechanics, Nuclear Engineering and Design 80, 233-245. 1985

Lemaitre, J., Chaboche, J. Mechanics of Solid Materials. Cambridge University Press, Cambridge. 1994.

Levin, V. Thermal expansion coefficients of heterogeneous materials. Mekh. Tverd. Tela 2, 83 – 94. 1967.

Maghous, S., Dormieux, L., Barthèlèmy, J. Micromechanical approach to the strength properties of frictional geomaterials. European Journal of Mechanics A/Solid 28, 179-188. 2009.

Marigo, J.J. Modeling of brittle and fatigue damage for elastic material by growth of microvoids, Engineering Fracture Mechanics 21, 861-874. 1985

Mazars, J. A description of micro-and macroscale damage of concrete structures, Engineering Fracture Mechanics 25, 729-737. 1986

Mialon, P. Eléments d'analyse et de résolution numérique des relations de l'élasto-plasticité. EDF Bull. Dir. Etud. Rech. Série C. Math., Inf., No. 3, 57 – 89. 1986.

Mori, T., Tanaka, K., Average stress in a matrix and average elastic energy of materials with misfitting inclusions. Acta Metall.Mater 42(7), 597-629. 1973

Nara Y., K. Kaneko. Study of subcritical crack growth in Andesite using the Double Torsion test. International Journal of Rock Mechanics & Mining Sciences; 42:521-530. 2005

Nara Y, Kaneko K, Sub-critical crack growth in anisotropic rock, International Journal of Rock Mechanics & Mining Sciences; 43: 437–453. 2006

Nemat-Nasser, S. and Hori, M. Micromechanics: overall properties of heterogeneous materials, North-Holland, Amsterdam, The Netherlands. 1999

Ortiz, M., Stainier, L. The variational formulation of viscoplastic constitutive updates. Comput. Methods Appl. Mech. Eng. 171, 419 – 444. 1999.

Pietruszczak S, Lydzba D, Shao JF. Description of creep in frictional materials in terms of microstructure evolution, Journal of Engineering Mechanics ASCE;130:681-690. 2004

Pijaudier-Cabot, G,. and Bazant, Z. P. Nonlocal Damage Theory. Journal of Engineering Mechanics ASCE 113(10), 1512-1533. 1987

Pletka BJ, Fuller Jr ER, Koepke BG. An evaluation of double torsion testing-experimental. ASTM STP; 678:19–37. 1979

Ponte Castañeda, P. New variational principles in plasticity and their application to composite materials. J. Mech. Phys. Solids 40, 1757 – 1788. 1992.

Ponte-Castaneda, P., Willis, J.-R. The effect of spatial distribution of effective behavior of composite materials and cracked media. Journal of the Mechanics and Physics of Solids 43, 1919-1951. 1995

Ponte Castañeda, P., Suquet, P. Nonlinear composites. Adv. Appl. Mech. 34, 171 – 302. 1998.

Ponte Castañeda, P., Willis, J.R. Variational second-order estimates for nonlinear composites. Proc. R. Soc. London A 455, 1799 – 1811. 1999.

Ponte Castañeda, P. Second-order homogenization estimates for nonlinear composites incorporating field fluctuations. I—Theory. J. Mech. Phys. Solids 50, 737 – 757. 2002.

Renald Brenner, Olivier Castelnau and Lori Badea. Mechanical field fluctuations in polycrystals estimated by homogenization techniques. Proc. R. Soc. Lond. A 2004 460, P3589-3612. 2004

Reuss, A. Calculation of the flow limits of mixed crystals on the basis of the plasticity of monocrystals. Z. Angew. Math. Mech, 9:49-58. 1929

Robinet JC. Mineralogie, porosite et diffusion des solutes dans l'argilite du callovo-oxfordien de bure (meuse/haute-marne, France) de l'échelle centimétrique à micrométrique. Doctoral thesis, University of Poitiers, France. 2008

Sammartino, G. Construction d'un modèle conceptuel d'organisation de la porosité et de la minéralogie des argilites du site de bure. Rapport final. Rapport ANDRA DRP0ERM01—018/A. 2001

Shao JF, Zhu QZ, Su K. Description of creep in rock materials in terms of material degradation, Computer and Geotechnics; 30:549-555. 2003

Shen, W.Q., Shao. J.F., Kondo. D., Gatmiri. B. Mesomechanical model for clayey rocks with plastic compressive porous matrix. Accepted by International Journal of Plasticity, 2012

Valès, F. Rapport d'étude: Géo-micromecanique. Études expérimentales de l'approche géo-micromecanique des argilites du site meuse/haute marne. Partie 1-b. Analyses microstructurales. Rapport ANDRA BRP0LMS2001-02/A. 2001

Voigt, W. Uber die beziehung zwischen den beiden elasticitat constantan isotroper korper. Ann. Phys. (Leipzig), 38:573-587. 1889

Voyiadjis G.Z., Taqieddin Z.N. and Kattan P.I. Theoretical Formulation of a Coupled Elastic—Plastic Anisotropic Damage Model for Concrete using the Strain Energy Equivalence Concept, International Journal of Damage Mechanics 18, 603-638. 2008

Waza T, Kurita K, Mizutani H. The effect of water on the subcritical crack growth in silicate rocks. Tectonophys; 67: 25-34. 1980

Willis, J. R. Variational and related methods for the overall properties of composites. Adv. Appl. Mech. 21, 2 – 78. 1981

Yang DS, Billiotte J, Su K. Characterization of the hydromechanical behavior of argillaceous rocks with effective gas permeability under deviatoric stress. Engineering Geology; 114:116-122. 2010

Yang DS, Bornert M, Chanchole S, Gharbi H, Valli P, Gatmiri B. Dependence of elastic properties of argillaceous rocks on moisture content investigated with optical full-field strain measurement techniques, International Journal of Rock Mechanics Mining Sciences; 53:45–55. 2012

Zhang C, Rothfuchs T. Experimental study of the hydro-mechanical behaviour of the

Callovo-Oxfordian argillite. Appl. Clay Sci.; 26:325–336. 2004

Zhou H, Jia Y, Shao JF. A unified elastic - plastic and viscoplastic damage model for quasi brittle rocks. International journal of rock mechanics and mining sciences; 45: 1237-1251. 2008

Zhu, QZ., Kondo, D., Shao, JF. Micromechanical analysis of coupling between anisotropic damage and friction in quasi brittle materials: role of the homogenization scheme. International Journal of Solids and Structures 45, 1385-1405. 2008